UNIVERSITY OF CALIFORNIA,
IRVINE

Multi-wavelength Photo-Magnetic Imaging: a novel high-resolution diffuse optical imaging modality

DISSERTATION

submitted in partial satisfaction of the requirements
for the degree of

DOCTOR OF PHILOSOPHY

in Physics

by

Maha Algarawi

Dissertation Committee:
Associate Professor Gultekin Gulsen, Chair
Professor Min-Ying (Lydia) Su
Professor Thorsten Ritz

2022

TABLE OF CONTENTS

LIST OF FIGURES

LIST OF TABLES

ACKNOWLEDGEMENTS

First and foremost, I would like to express my sincere gratitude to my advisor Professor Gultekin Gulsen. Over the years I have spent working at the Center for Functional Onco-Imaging (CFOI), he has been an astonishing mentor who has provided guidance and encouragement throughout my Ph.D. Without his guidance and persistent help, this dissertation would not have been possible. I appreciate all the time he spent helping, teaching, and training me in the lab.

I also would like to thank Dr. Farouk Nouizi for his insightful comments and encouragement. I am grateful to his enormous contribution towards this work and all his help. I would like to thank him for helping me in programming, reviewing my papers, and for always finding time for our discussions.

Additionally, I would like to thank my committee members, Professor Lydia Su and Professor Thorsten Ritz for serving as committee members and for their time and expertise to improve my work.

I would also like to thank the amazing people that I met at (CFOI) for their invaluable support and willingness to share their expertise, especially: Dr. Hakan Erkol, Dr. Alex Luk, Dr. Tiffany Kwong, Dr. Yang Zhang and Lena Qin.

I acknowledge the generous financial support I have received from my country (Saudi Arabia) through the Saudi Arabian Cultural Mission in United States (SACM). I also would like to thank the department of Physics at Imam Mohammad ibn Saud University for the opportunity to pursue my degree at the University of California, Irvine.

Special thanks to my parents, Dr. Mohamed Algarawi and Fawzyah Algarawi, for their unconditional love, motivation and unlimited support. A big thanks to my husband Mohaned, for being supportive, encouraging and patient with me during my most difficult times. Lastly, I would like to thank my brother, my sisters and all who have helped me to make my educational journey successful.

VITA

Maha Algarawi

EDUCATION

2008 B.S. in Physics, King Saud University, Riyadh, Saudi Arabia

2013 M.S. in Physics, King Saud University, Riyadh, Saudi Arabia

2022 Ph.D. in Physics, University of California, Irvine

PUBLICATIONS

Algarawi, M., Erkol, H., Luk, A., Ha, S., Burcin Unlu, M., Gulsen, G., & Nouizi, F. (2020). Multi-Wavelength Photo-Magnetic Imaging System for Photothermal Therapy Guidance. *Lasers in Surgery and Medicine.*

Algarawi, M., Erkol, H., Luk, A., Ha, S., Ünlü, M. B., Gulsen, G., & Nouizi, F. (2020). Resolving tissue chromophore concentration at MRI resolution using multi-wavelength photo-magnetic imaging. *Biomedical Optics Express*, *11*(8), 4244-4254.

Erkol, H., Yelken, S. Z., **Algarawi, M.,** Gulsen, G., & Nouizi, F. (2020). Validation of a comprehensive analytical model for photothermal therapy planning in a layered medium with gold nanoparticles. *International Journal of Heat and Mass Transfer*, *163*, 120438.

Nouizi, F., **Algarawi, M**., Erkol, H., Luk, A., & Gulsen, G. (2021). Multiwavelength photo-magnetic imaging algorithm improved for direct chromophore concentration recovery using spectral constraints. Applied Optics, 60(35), 10855-10861.

CONFERENCE PROCEEDINGS

Erkol, H., Nouizi, F., Luk, A., Mehrabi, M., **Algarawi, M**., Unlu, M. B., & Gulsen, G. (2018, April). A comprehensive analytical based computational approach for laser induced heat in a heterogeneous turbid medium. In *Microscopy Histopathology and Analytics* (pp. JTh3A-16). Optical Society of America.

Nouizi, F., Erkol, H., Luk, A., **Algarawi, M**., Mehrabi, M., & Gulsen, G. (2018, April). Multi-wavelengths Photo Magnetic Imaging. In *Optical Tomography and Spectroscopy* (pp. JW3A-45). Optical Society of America.

Algarawi, M., Nouizi, F., Luk, A., Mehrabi, M., Erkol, H., Ünlü, M. B., ... & Ha, S. (2019, February). High-resolution chromophore concentration recovery using multi-wavelength photo-magnetic imaging. In *Multimodal Biomedical Imaging XIV* (Vol. 10871, p. 108710F). International Society for Optics and Photonics.

Mehrabi, M., Nouizi, F., **Algarawi, M.**, Kwong, T. C., Erkol, H., Sampathkumaran, U., & Gulsen, G. (2019, March). CCD-based temperature modulated fluorescence tomography. In *Optical Tomography and Spectroscopy of Tissue XIII* (Vol. 10874, p. 108740Y). International Society for Optics and Photonics.

Algarawi, M., Luk, A., Erkol, H., Almudhry, M., Unlu, B. M., Gulsen, G., & Nouizi, F. (2020, April). Reconstruction chromophore concentration directly by Photo-Magnetic Imaging: simulation study. In *Clinical and Translational Biophotonics* (pp. JTu3A-15). Optical Society of America.

Algarawi, M., Nouizi, F., Luk, A., Erkol, H., Almudhry, M., Unlu, B. M., ... & Gulsen, G. (2020, April). Experimental validation of a multiple wavelength Photo-Magnetic Imaging system. In *Optical Tomography and Spectroscopy* (pp. STh3D-3). Optical Society of America.

Algarawi, M., Erkol, H., Gulsen, G., & Nouizi, F. (2022) Imaging gold-nanoparticle distribution with photo-magnetic Imaging. In *SPIE BiOS*. International Society for Optics and Photonics. (submitted)

Nouizi, F., **Algarawi, M**., Erkol, H., Luk, A, & Gulsen, G. (2022) Photo-magnetic imaging: a new functional imaging modality for more accurate photothermal therapy planning. In *Photodynamic Therapy III*. International Society for Optics and Photonics. (submitted)

ABSTRACT OF THE DISSERTATION

Multi-wavelength Photo-Magnetic Imaging: a novel high-resolution diffuse optical imaging modality

by

Maha Algarawi

Doctor of Philosophy in Physics

University of California, Irvine, 2022

Associate Professor Gultekin Gulsen, Chair

The functional state of biological tissue alters the optical properties of its constituents; therefore, studying the distribution of tissue chromophores is beneficial as it provides a contrast between abnormalities and normal surrounding tissue. Diffuse optical tomography (DOT) is one of the optical imaging modalities that is used noninvasively to quantify tissue chromophore concentrations such as water, lipid, oxy- and deoxy- hemoglobin by employing near infrared (NIR) light at multiple optical wavelengths. It has been demonstrated that these optical measurements have the ability to differentiate between diseased and normal tissues. Although DOT can obtain valuable information, its spatial resolution is very poor resulting in very low quantitative accuracy.

Extensive efforts have been made to enhance the performance of DOT. Its combination with anatomical imaging modalities has been widely demonstrated to improve its spatial resolution through the use of structural information. Yet, this approach is limited to a few cases due to technical challenges required for such incorporation. Furthermore, the optical and anatomic imaging systems in those multi-modalities are working independently from each other. To overcome these limitations, our lab introduced a new technology termed, “multi-wavelength

Photo-Magnetic Imaging (PMI)" in the recent years. PMI is a hybrid modality that synergistically utilizes NIR light and Magnetic Resonance Imaging (MRI). Unlike DOT where measurements are acquired only at the boundary, PMI utilizes MRI to noninvasively acquire the laser-induced temperature measurements internally. Utilizing multiple wavelengths PMI, endogenous and exogenous chromophore concentrations are recovered. In contrast to other conventional multi-modality approaches, optical and MR modalities work together in harmony by interacting with each other in PMI. However, PMI developmental efforts have been limited to a basic single-wavelength prototype system up to now.

This thesis presents the development of the novel multi-wavelength PMI system including the instrumentation and its associated control software. This system can noninvasively elevate the internal temperature of biological tissue by a few degrees utilizing five wavelengths ranging between 760 nm and 980 nm, where the laser-induced temperature is internally measured using MRI. Two image reconstruction approaches are developed and implemented to recover the chromophore concentrations from PMI multi-wavelength temperature measurements. The feasibility of the multi-wavelength PMI technique for providing chromophore concentrations with high spatial resolution and high quantitative accuracy is validated using simulation studies and experimentally demonstrated on homogenous and heterogeneous phantoms, using several newly introduced PMI reconstruction methods.

Chapter 1: Introduction

1.1 Introduction

The field of medical imaging has undergone major advancements to provide fundamental information about variety of diseases. The process of medical imaging is based on the interaction of different types of energy with tissue to extract structural or functional information. This information can aid in detection and diagnosis of different diseases including cancer, as well as treatment planning and therapy monitoring. Different medical imaging techniques have been developed throughout the years such as magnetic resonance imaging (MRI), X-ray computed tomography (CT), ultrasound imaging (US) and nuclear imaging techniques, such as positron emission tomography (PET) and single photon emission computed tomography (SPECT). Beside those conventional imaging techniques, optical imaging, which has rapidly developed over the past two decades, has also demonstrated promise for detection, diagnosis and monitoring therapeutic response of cancer and other diseases.

Optical imaging is a medical imaging technique that provides valuable functional information. It is safe since it utilizes nonionizing radiation. Light in near infrared window (NIR), between 600 and 1000 nm, is beneficial to be used in optical imaging due to its ability to penetrate deep in biological tissue since such medium exhibits a relatively low optical attenuation within this spectral range [1, 2]. Therefore, NIR has been widely used in optical imaging to retrieve optical properties of biological tissue.

1.2 Diffuse optical tomography (DOT)

DOT is one of the optical imaging modalities that provides functional information about the physiology of thick biological tissue. DOT is based on illuminating the tissue with NIR light

on the surface from multiple points while transmitted and reflected light is measured from multiple detection points. When light propagates in biological tissue, it interacts mainly by scattering and absorption, which results in light intensity attenuation. The attenuated light is then noninvasively collected at the tissue boundary by photodetectors arranged at multiple positions to obtain tomographic images of the imaged medium [3, 4]. Light sources and detectors are either placed on the same side as in reflectance mode, or on opposite sides of the tissue in transmission mode [5]. Based on the measured attenuated light, the optical properties of the medium they propagated through can be recovered using a sophisticated image reconstruction algorithm where the photon propagation is iteratively modelled by diffusion equation and matched to the actual measured data to recover the unknown optical properties [6, 7].

DOT is used to recover tissue optical properties which then can be used to obtain the concentration of tissue chromophores such as oxy-hemoglobin, deoxy-hemoglobin, lipid and water [8, 9]. Recovering tissue chromophore concentration is important to provide functional information such as total hemoglobin concentration and oxygen saturation. In addition to these valuable functional parameters, DOT can be applied frequently as it utilizes nonionizing radiation. Due to these features, DOT has become an important low-cost clinical research tool in several areas especially for breast cancer detection and characterization [10, 11]. The concentration of total hemoglobin and the saturation of oxygen obtained via DOT can give insight on the angiogenesis and hypermetabolism state of the tumor which correlates with its malignancy [12, 13]. It has been demonstrated that malignant tumors have higher total hemoglobin concentration and lower oxygen saturation compared to the normal tissue [14, 15]. Also, by employing broader wavelength range, higher water concentration and lower lipid concentration have been observed in malignant tumors compared to normal tissue [16, 17]. DOT has also been used for other

applications such as functional brain imaging [3, 18], joint disease imaging such as rheumatoid arthritis [19, 20], and cancer therapy monitoring [21, 22].

Although DOT has shown high sensitivity in quantifying blood volume and oxygenation saturation level in biological tissue, its translation to the clinical arena is still hampered due to some serious limitations. The most significant limitation of DOT originates from the highly scattering nature of the biological tissue. Since photons experiencing multiple scattering events in their paths before they are measured at the boundary, the DOT inverse problem is highly ill-posed and under-determined [23]. Consequently, the resolution of the DOT is limited to approximately 1–5 mm depending on the tissue thickness/depth as well as the type and configuration of the measurements [24, 25]. The limited resolution of DOT causes significant effect on the quantitative accuracy of the obtained functional information. That leads to inaccuracy in the diagnosis of the disease and treatment regimen followed by clinicians. Therefore, increasing the resolution and accuracy of the DOT is crucial for its clinical translation.

Extensive efforts have been made to improve the performance of DOT. For example, incorporating DOT with high-resolution anatomical imaging modality such as MRI [26, 27], X-ray [28, 29], and ultrasound [10, 30] has significantly improved the quality of DOT reconstructed images. In this approach, DOT image reconstruction algorithm would use the structural information provided by the anatomical imaging modality as *a priori* information. In fact, this approach not only successfully enhances the image spatial resolution but also improves the quantitative accuracy of the functional information [31-34]. However, this method does not overcome the ill-posedness of the inverse problem as the optical measurements are still acquired at the boundary of the object. Furthermore, this approach fails to recover the heterogeneity of the tumor, and this is mostly noticed on large tumors where a necrotic region is developed [26, 34].

Consequently, there is a necessity for a true multi-modality where both imaging modalities perform simultaneously to provide precise and reliable information regardless of the heterogeneity of the medium.

1.3 Photoacoustic Tomography (PAT)

An example of a true multi-modality is the photoacoustic tomography (PAT) which combines the high ultrasonic resolution and the high contrast of the optical imaging. PAT utilizes pulsed laser to illuminate the biological tissue where the absorbed energy is converted into heat. This induced-temperature variation in biological tissue causes a thermoelastic expansion of tissue, resulting in the generation of ultrasound waves. The resulted ultrasound waves are detected with transducers which then can be processed to form image of the optical absorption distribution [35, 36]. Compared with the purely optical tomography DOT, PAT can penetrate the biological tissue deeper due to the weak scattering of the sound waves compared to the light scattering in this medium. Owing to such feature, PAT has been used in different medical applications including but not limited to breast cancer detection and diagnosis [37, 38], joint inflammations early detection and characterization [39], and neurofunctional activities evaluation [40, 41].

Although PAT is capable to provide functional information with spatial resolution of ultrasound, it still faces some challenges. As the conventional ultrasound, there is a trade-off between the image resolution and the probing depth. For instance, when imaging deep objects, the resolution is reduced and the number of photons penetrating the medium is also reduced due to the absorption by shallower objects [42]. The imaging depth can be sacrificed to improve the resolution up to the micron-scale, as in photoacoustic microscopy [43]. Another factor is the effect of the of acoustic impedance mismatch between different tissue types which results to a strong signal reflection. There are also some limitations arising from transducer configurations. For

example, transducers arranged in one line would limit the imaging view; consequently, the recovered image would be inaccurate [44]. While arranging transducers on a ring-shape might enhance the imaging view, but it would utilize large number of transducers, which as result will increase the system complexity and cost [45, 46]. On the other hand, systems consisting of limited number of transducers require rotation around the object which is time consuming and inconvenient for patients [47].

1.4 Photo-magnetic imaging (PMI)

Previously, our lab invented Photo-Magnetic Imaging (PMI) to overcome the previous limitations. PMI is a true multi-modality imaging technique that combines diffuse optics with MRI in a novel way. It utilizes laser sources in NIR range to illuminate the tissue. Then, the induced temperature distribution is measured internally using Magnetic Resonance Thermometry (MRT). Thus, PMI does not utilize the high-resolution MRI system to provide structural *a priori* information as in the conventional multi-modality approaches, but to measure the 3-D internal laser-induced temperature distribution. The measured temperature increase is proportional to the tissue absorption coefficient as well as the amount of the absorbed light. Consequently, the measured temperature maps can be used to recover the optical absorption maps using a dedicated PMI image reconstruction algorithm. During the PMI image reconstruction process, the absorption map at a given wavelength is recovered by iteratively minimizing the difference between the measured and simulated temperature maps, which are generated by solving the combined diffusion and Pennes' bioheat thermal equations. Unlike the stand-alone DOT where only the superficial measurements are acquired, PMI utilizes MRT which facilitates the internal temperature measurements making its inverse problem well-posed. Therefore, PMI provides absorption maps with high-resolution and quantitative accuracy. The superior performance of the single-wavelength

PMI technique on recovering high-resolution absorption maps has been demonstrated with various simulation and experimental studies [48-57]. Although single-wavelength PMI can provide absorption maps with high-resolution and quantitative accuracy, one laser wavelength is not sufficient to provide comprehensive functional information important for characterization and diagnosis.

1.5 Multi-wavelength PMI

The excellent performance of the single-wavelength PMI has motivated to upgrade the technique to multiple wavelengths in order to obtain functional information with high-resolution and quantitative accuracy. Therefore, in this thesis, we upgrade the single-wavelength PMI to a full multi-wavelength version: “Multi-wavelength Photo-Magnetic Imaging”. This novel multi-wavelength PMI technique utilizes five laser wavelengths in the NIR range, ranging between 760 nm and 980 nm. These specific wavelengths were chosen carefully to allow the recovery of tissue endogenous chromophores such as oxy- and deoxy- hemoglobin, water and lipid contents as well as distribution of exogenous contrast agents. Each of these chromophores has a distinct absorption spectrum. Therefore, at a specific wavelength, tissue optical absorption is defined as the total absorption resulted by the contribution of absorption of each chromophore at this particular wavelength. By utilizing single wavelength, the total absorption would be recovered. However, the concentration of each individual chromophore is particularly important to provide functional information such as total hemoglobin concentration and oxygen saturation. To estimate such an important information, measurements at multiple wavelengths should be acquired in order to provide the concentration of each individual chromophores.

1.6 Innovations and contributions

A number of innovations and contributions have been achieved during this work:

1- The main innovation in this work is the development of the multi-modality technique: multi-wavelength PMI. This technique combines the high-resolution of MRI with the sensitivity of DOT to provide high-resolution and high quantitative accuracy chromophore concentrations maps.

2- The first-of-its-kind multi-wavelength PMI system has been developed during this work. This system is considered as a low-cost add on to any MRI system to perform preclinical and clinical studies. Multi-wavelength PMI system was built with five wavelengths ranging between 760 nm and 980 nm to slightly increase the internal temperature of the medium, which is monitored and measured using MRI.

3- A user-friendly control panel created using LabVIEW software was also developed to communicate with the hardware of the multi-wavelength PMI system through National instruments data acquisition devices.

4- Two multi-wavelength PMI image reconstruction approaches were developed to recover the chromophore concentrations from PMI multi-wavelength temperature measurements. Both methods, PMI conventional and direct methods, were validated on different simulation and experimental studies.

Chapter 2: Principle and method of PMI

This chapter describes the interaction of light and biological tissue, PMI image reconstruction algorithm, and PMI methodology on recovering the high-resolution chromophore concentration maps.

2.1 Light interactions with biological tissue

Interaction of photons with biological tissue has to be well understood in order to accurately model light propagation and consequently recover the tissue optical properties from the acquired measurements. The mechanism of light and tissue interactions is described by different optical properties such as: absorption, scattering, and index of refraction.

2.1.1 Absorption

As light is propagating through tissue, some photons will be absorbed by the medium. This causes a reduction in the amount of the transmitted light compared to the incident one and causes temperature elevation due to the conversion of the absorbed photons energy into heat. The relationship between the intensity of light and the absorption of a medium can be described by Beer-Lambert law [58]:

$$I = I_0 e^{-\mu_a x} \tag{1}$$

This expression states that the intensity of an incident light I_0 is exponentially attenuated when traveling through a medium having an absorption coefficient μ_a and a thickness x. This expression is valid only when the light travels in a purely absorbing medium. Figure 1 shows an illustration of the light intensity attenuation due to the absorption of the medium as described by the Beer-Lambert law.

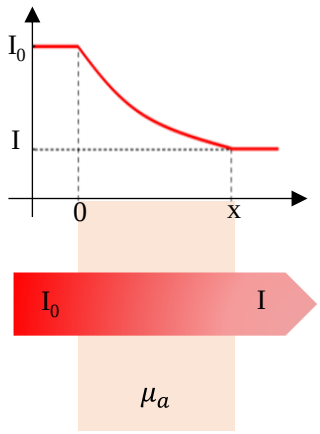

Figure 1: Attenuation of light intensity when traveling through an absorbing medium based on Beer-Lambert law.

The absorption coefficient μ_a $[\mathrm{mm}^{-1}]$, is defined as the probability of a photon to be absorbed per unit length when traveling through a medium. The reciprocal of the absorption coefficient is defined as the absorption mean free path, that represents the distance that a photon can travel before being absorbed. A photon can be absorbed only if its energy is exactly equal to the energy difference between two energy levels in a molecule of the illuminated medium. As the molecule absorbs only specific amounts of energy, only specific wavelengths will be absorbed making the absorption strongly wavelength-dependent. In general, the absorption coefficient of a medium at wavelength λ is described as the sum of the absorption of its constituents [59]:

$$\mu_{a_{tot}}(\lambda) = \sum_{i=1}^{P} \mu_{a_i}(\lambda) \tag{2}$$

where $\mu_{a_{tot}}$ is the total absorption coefficient, μ_{a_i} is the absorption coefficient of chromophore i. and P is the number of the chromophores in the medium.

2.1.2 Scattering

Another factor describing light-tissue interactions, is photons scattering. A scattering event causes deviation in the propagation direction of photons. Specifically, scattering occurs when

photons encounter particles that have index of refraction different from the surrounding medium. The scattering coefficient of a medium μ_s $[\mathrm{mm}^{-1}]$, is defined as the probability of a photon to be scattered in a medium per unit length. The scattering mean free path, which represents the reciprocal of scattering coefficient, is defined as the spatial interval between two consecutive scattering events.

Biological tissue is considered as anisotropic medium, where most of light photons travel in the forward direction. The angle between the incident and the scattered direction is known as the scattering angle. The anisotropy factor, g, is defined as the average of the cosine of the scattering angles of all photons. This factor determines the preferred direction of the scattering in a medium. If the anisotropy factor g is near unity, then light scattering is mostly forward. The anisotropy factor is found to be between 0.8 and 0.99 for biological tissue [60]. Therefore, scattering within biological tissue cannot be characterized by the scattering coefficient only, but requires the consideration of the anisotropy factor. As a result, the scattering is described using the reduced scattering coefficient which is related to both factors as follow [61]:

$$\mu_s'(\lambda) = \mu_s(1 - g) \tag{3}$$

where μ_s' $[\mathrm{mm}^{-1}]$ is the reduced scattering coefficient which represents the probability of equivalent isotropic photon scattering by a medium per unit length.

The scattering in biological tissue depends on the light wavelength and the properties of tissue particles. Scattering can be classified into two main categories based on the medium particles size: Rayleigh and Mie scattering [9]. Scattering by particles much smaller than the wavelength of light is referred to as Rayleigh scattering. In contrast, Mie scattering refers to scattering by particles comparable to or larger than the wavelength of light. The spectrum of the reduced scattering

coefficient in tissue can be calculated using the following empirical approximation to Mie scattering theory [62]:

$$\mu_s'(\lambda) = A\lambda^{-b} \tag{4}$$

where A is the scattering amplitude and b is the scattering power. These parameters depend on the structure of the tissue in terms of the scatterers size and density.

2.1.3 Index of refraction

The index of refraction of a medium describes the effect on the speed of the incident light. When the light passes across the boundary separating two media with different index of refraction, the speed of light is changing causing its direction to change, as show in Figure 2.

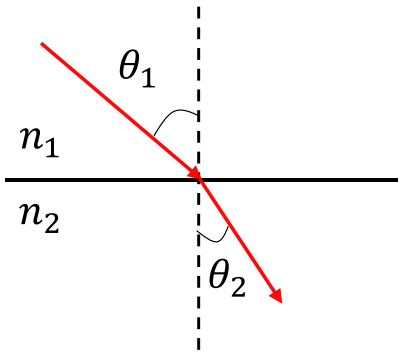

Figure 2: illustration of Snell's law shows the refraction between two media with different index of refraction.

The relationship between the angles of incidence and refraction is described by Snell's law:

$$n_1 sin\theta_1 = n_2 sin\theta_2 \tag{5}$$

where θ_1 and θ_2 are the angles of incident and refracted light. n is the index of refraction which is defined as the ratio of the speed of light in vacuum, c_0, to the speed of light in a particular medium, c, as given by:

$$n = \frac{c_0}{c} \tag{6}$$

2.2 Endogenous chromophores

Endogenous chromophores refer to molecules naturally present in the biologic tissue that absorb light at a specific wavelength. The main endogenous chromophores that absorb NIR light are hemoglobin, water and lipid. Hemoglobin is present either in its oxygen-saturated form, oxy-hemoglobin (HbO_2), or in the oxygen-unloaded form, deoxy-hemoglobin (Hb). The hemoglobin oxygenation level results in a difference between the optical absorption spectra of these two hemoglobin forms. Each of the endogenous chromophores has a unique absorption spectrum as shown in Figure 3.

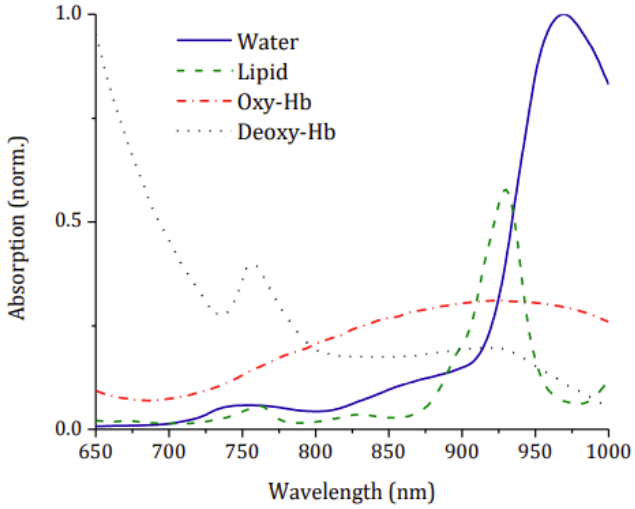

Figure 3: The optical absorption coefficient spectrum as a function of wavelength of the four main tissue chromophores [63].

One of the main advantages of optical imaging is the ability to utilize these endogenous chromophores as biomarkers since the change in their optical properties often indicates tissue abnormality. Hence, endogenous chromophores frequently used to identify physiological problems and monitor the effects of therapy. For deeper light penetration, most of the optical

imaging techniques utilize NIR light since the absorption coefficients of these chromophores are low compared to their values at the visible and the second NIR windows.

2.2.1 Chromophore concentration

The total absorption coefficient of a certain medium is the sum of contributions from all its absorbing chromophores, as stated in equation (2). The absorption of each chromophore at a given wavelength is expressed by the modified Beer-Lambert law [64]:

$$\mu_a(\lambda) = ln10.\varepsilon(\lambda).C \tag{7}$$

where ε is the wavelength dependent extinction coefficient that gives the absorption μ_a at a specific concentration C. Using this equation, the concentration is resolved by recovering the absorption coefficient at specific wavelength and using the known extinction coefficient at that same wavelength. For example, oxy- and deoxy-hemoglobin share the same absorption coefficient at the hemoglobin isosbestic point at 806 nm [9]. Therefore, acquiring measurement using single wavelength at the isosbestic point allows to directly measure the changes in the total hemoglobin concentration that can probe tumor angiogenesis [65]. On the other hand, acquiring measurements at multiple wavelengths allows differentiation between HbO_2 and Hb by recovering their absolute concentration using the recovered absorption at each wavelength in equation (2) and (7) with the known extinction coefficient [66-68]. Consequently, not only the total hemoglobin concentration $[THb]$ can be recovered, but also the hemoglobin oxygen saturation stO_2:

$$[THb] = [Hb] + [HbO_2],$$
$$stO_2 = \frac{[HbO_2]}{[THb]} \times 100\% \tag{8}$$

By applying longer wavelengths, water and lipid can be also resolved and used to provide additional information. The concentration of each tissue endogenous chromophore can be

compared individually, or a combined tissue optical index (TOI) can be calculated to evaluate therapeutic monitoring [69, 70]:

$$TOI = \frac{[Hb]}{[lipid]} \times [water] \tag{9}$$

2.3 PMI image reconstruction algorithm

In PMI, a continuous wave (CW) NIR laser source is used to illuminate the medium under investigation and elevate its temperature. The laser-induced temperature, which is directly related to the local optical absorption and photon density, is measured using MRT. During PMI image reconstruction, the measured temperature is compared to simulated temperature maps generated from the PMI forward problem by assuming a specific optical absorption distribution within the medium. The difference between the measured and simulated temperature maps is minimized iteratively by updating the assumed optical absorption. Consequently, the absorption map is recovered once the difference between the measurement and simulation maps is minimized. PMI image reconstruction algorithm is described in the diagram shown in Figure 4.

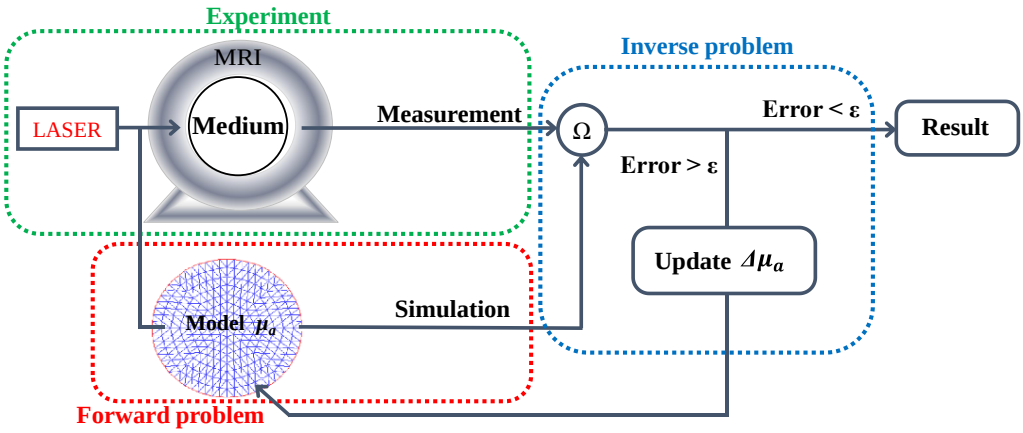

Figure 4: Diagram of the PMI image reconstruction algorithm.

2.3.1 PMI forward problem

The first step during the modeling of the internal laser-induced temperature, is the modeling of the propagation of light in the medium. The following section describes the approach and mathematical models used for light propagation modeling in PMI.

2.3.1.1 Modelling light propagation in biological tissue

2.3.1.1.1 Radiative transfer equation

The propagation of light in tissue is widely described using the Boltzmann transport equation or the radiative transfer equation (RTE) [71-73]:

$$\frac{1}{c}\frac{\partial L(\vec{r},t,\hat{s})}{\partial t} + \hat{s}.\nabla L(\vec{r},t,\hat{s}) + [\mu_a + \mu_s]L(\vec{r},t,\hat{s}) = \mu_s \iint_{4\pi} f(\hat{s},\hat{s}')L(\vec{r},t,\hat{s}')d\hat{s}' + q(\vec{r},t,\hat{s}) \quad (10)$$

RTE describes the change of the radiance $L(\vec{r},t,\hat{s})$ [$\mathrm{W.m^{-2}.sr^{-1}}$] at time t at position $\vec{r}$ towards direction $\hat{s}$. Where, $q(\vec{r},t,\hat{s})$ [$\mathrm{W.m^{-3}.sr^{-1}}$] is the emitted energy per unit of volume per unit of time along the direction $\hat{s}$. The parameters μ_a, μ_s are the absorption and scattering coefficients, respectively. c is the speed of light in the medium, and $f(\hat{s},\hat{s}')$ is the scattering phase function that represents the probability of light scattering from a given direction $\hat{s}$ to direction $\hat{s}'$. Solving the RTE is computationally heavy as it depends on different independent variables (space, angle, and time). Simplifying the RTE by making a series of assumptions, leads to a simpler approximation as the number of the independent variables is reduced. Often, RTE is approximated to its most used form, which is known as the diffusion equation (DE). The DE has been widely accepted to model light propagation in biological tissue [23, 74].

2.3.1.1.2 Diffusion equation (DE)

The use of the diffusion equation is usually preferred to the RTE in order to overcome the heavy computational burden. The DE approximation is generally accepted in a medium where scattering is largely dominant, and assuming that light scattering is isotropic, which requires that the source detector distance is larger than the scattering mean free path. In this approach, the RTE integrodifferential equation is simplified by a first order approximation of the spherical harmonics expansion. Furthermore, the temporal variation in the flux vector is assumed to be negligible, and the light source is isotropic. This approximation allows the conversion of the anisotropic light radiance $L(\vec{r}, t, \hat{s})$ to isotropic photon density $\Phi(\vec{r}, t)$ in the case where the scattering of the medium dominates over the absorption [75, 76]. Photon density is related to the light radiance by the following integral:

$$\Phi(\vec{r}, t) = \int_{4\pi} L(\vec{r}, t, \hat{s})\, d\hat{s} \tag{11}$$

Therefore, the propagation of NIR photons in biological tissue, where ($\mu_s' >> \mu_a$), is considered isotropic and modeled using the angle-independent diffusion equation:

$$-\nabla.[D(\vec{r})\nabla\Phi(\vec{r}, t)] + \mu_a(\vec{r})\Phi(\vec{r}, t) + \frac{1}{c}\frac{\partial\Phi(\vec{r}, t)}{\partial t} = S(\vec{r}, t) \tag{12}$$

where $\Phi(\vec{r}, t)$ [W. mm^{-2}] is the direction-independent photon density, $S(\vec{r}, t)$ [W. mm^{-3}] is the isotropic light source, $\mu_a(\vec{r})$ [mm^{-1}] is the absorption coefficient, and $D(\vec{r})$ [mm] is the diffusion coefficient defined as:

$$D(\vec{r}) = \frac{1}{3\left(\mu_a(\vec{r}) + \mu_s'(\vec{r})\right)} \tag{13}$$

where $\mu_s'(\vec{r})$ [mm^{-1}] is the reduced scattering coefficient.

Multi-wavelength PMI system utilizes CW laser diodes; hence, the diffusion equation is further simplified to a time-independent diffusion equation that is expressed as:

$$-\nabla.[D(\vec{r})\nabla\Phi(\vec{r})] + \mu_a(\vec{r})\Phi(\vec{r}) = S(\vec{r}) \quad (14)$$

This diffusion equation form is used to express the photon density $\Phi(\vec{r})$ at any position $\vec{r}$ after illuminating the medium by a CW light source.

2.3.1.1.3 Boundary conditions

The solution of the diffusion equation requires applying the appropriate boundary condition to model the behavior of photons on the surface of the biological tissue. Therefore, the Robin boundary condition that relates the photon density to photon flux at the boundary is used [77, 78]:

$$\Phi(\vec{r}) + 2AD(\vec{r})\nabla\Phi(\vec{r}).\vec{n} = 0 \quad (15)$$

where $\vec{n}$ is the normal vector perpendicular to the surface of the medium, $\vec{r}$ is a point on the external boundary, and A is the index mismatch parameter that is related to the internal reflection caused by the mismatch in the refractive index on the tissue surface, and defined as:

$$A = \frac{1+R}{1-R} \quad (16)$$

The internal reflection coefficient R is approximated by [79]:

$$R = -1.4399n^{-2} + 0.7099n^{-1} + 0.6681 + 0.0636n \quad (17)$$

where n is the refractive index of the medium.

Consequently, the photon flux is represented as the photon density measured at the boundary weighted by the parameter $2A$:

$$J(\vec{r}) = -D(\vec{r})\,\nabla\Phi(\vec{r}).\vec{n} = \frac{\Phi(\vec{r})}{2A} \quad (18)$$

2.3.1.2 Modelling heat propagation in tissue

After obtaining the photon density in the medium using the diffusion equation, the induced spatial and temporal temperature distribution and variation is modeled as described below.

2.3.1.2.1 Pennes bioheat equation

The second order partial differential equation that was developed by Harry H. Pennes in 1948, is used to model the heat transfer in biological tissue [80, 81]:

$$\rho c \frac{\partial T(\vec{r},t)}{\partial t} - \nabla.[k\nabla T(\vec{r},t)] = Q_m + Q_s + \rho_b w_b c_b[T_a - T(\vec{r},t)] \quad (19)$$

where T is tissue temperature [°C] at position $\vec{r}$ [mm] at time t [sec], ρ is the density [kg. m^{-3}], c is the specific heat [J. (kg. °C)$^{-1}$], and k is the thermal conductivity [W. (mm. °C)$^{-1}$] of the tissue. T_a [°C] is the temperature of arterial blood, w_b [kg. sec^{-1}. mm^{-3}] is the blood perfusion rate, c_b is the blood specific heat, and ρ_b is the density of the blood. Q_m [W. mm^{-3}] is the metabolic heat generation. And Q_s [W. mm^{-3}] is the heating source, which is induced by the NIR laser and is defined as follow:

$$Q_s(\vec{r}) = \Phi(\vec{r})\mu_a(\vec{r}) \quad (20)$$

where $\Phi(\vec{r})$ is the photon density resulted from the diffusion equation (5), and $\mu_a(\vec{r})$ is the local optical absorption [55, 67].

For PMI studies that were conducted on phantoms, the heat transfer was modeled by modifying the Pennes bioheat equation to the heat conduction equation [48, 66]:

$$\rho c \frac{\partial T(\vec{r},t)}{\partial t} - \nabla.[k\nabla T(\vec{r},t)] = Q_s \quad (21)$$

This equation shows that at any position r in the medium and at time t, the rate of heat energy flow due to the conduction in a unit volume together with the rate of heat energy generated by the

external laser source should be equal the rate of heat energy accumulated within a volume in the medium. The blood perfusion term as well as the heat generation by metabolism term are neglected.

2.3.1.2.2 Boundary conditions

The heat transfer in a medium can be studied accurately once the boundary condition is applied. In this this thesis, the boundary at the medium surface is modeled using the heat convection boundary condition [49, 81]:

$$-k.(\nabla T(\vec{r}).\vec{n}) = h[T_{ext} - T(\vec{r})] \quad (22)$$

where T_{ext} [°C] is the external environment temperature, and h is the heat transfer coefficient $[\mathrm{W}.(\mathrm{mm}^2.℃)^{-1}]$. This condition states that the convective heat transfer between two media is described by their temperature difference and the heat transfer coefficient.

2.3.1.3 Solution of PMI forward problem

The solution of the combined diffusion and heat equations system can be obtained using either analytical or numerical approaches or a combination of both [82-84]. The analytical method, which is usually based on obtaining the Greens function for a specific boundary condition, can provide considerably accurate results compared to numerical methods and in a short computational time [85]. However, this method is limited to simplistic geometries such as spherical or cylindrical as well as infinite or semi-infinite slabs [86-88].

On the other hand, the numerical techniques can provide a better solution for realistic situations with irregular and complex geometries. Monte Carlo is considered as the gold standard for modelling the photon propagation in biological tissues by employing a probability distribution model [89]. However, such a statistical method requires a large number of samples to achieve

accurate results which makes it very slow and computationally heavy [90]. Alternatively, Finite Element Method (FEM) is the most used technique to provide a relatively fast and accurate numerical solution to the combined diffusion and heat equation system.

Both analytical and numerical methods have been implemented to provide a solution to the PMI forward problem. Based on PMI previous studies, the results generated using the analytical approach were in a very good agreement with the results obtained using FEM as well as the experimental data [54, 57, 85, 91]. The numerical solution of the PMI forward problem is presented in detail in the following section.

For the numerical solutions, FEM is used to solve both the diffusion and the heat equations. In this approach, a mesh is generated over a domain having the same dimension as the real object. The domain is divided into nonoverlapping small elements, generally triangles and tetrahedrals for 2-D and 3-D cases, respectively. These elements are connected by vertices known as mesh nodes [92]. The diffusion and heat equations are then solved at each node in the mesh. Figure 5 shows an example of a circular 2-D mesh with triangular elements.

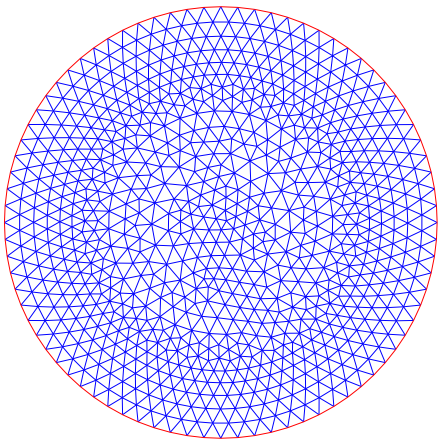

Figure 5: Example of a 2-D FEM mesh with 852 nodes and 1622 triangular elements.

To apply the FEM to the diffusion and heat equations, equation (14) and (21), they must be first converted to their weak form. The weak formulation is obtained by multiplying each term in these equations by a test function v and integrate over a domain Ω. After integrating by parts, the weak forms of the diffusion and heat equations are expressed as in equation (23) and (24), respectively [78, 92, 93]:

$$\int_{\Omega} D\ \nabla\Phi\nabla v d\Omega + \int_{\Omega} \mu_a\, \Phi\ v d\Omega = \int_{\Omega} Sv\mathrm{d}\Omega \tag{23}$$

$$\int_{\Omega} \rho c \frac{\partial T}{\partial t} v\, d\Omega + \int_{\Omega} k\ \nabla T\nabla v d\Omega = \int_{\Omega} Q_s v\mathrm{d}\Omega \tag{24}$$

The FEM solutions of the photon density $\Phi(\vec{r})$ and temperature $T(\vec{r},t)$ are approximated by polynomial functions as stated in equation (25) and (26), respectively:

$$\Phi(\vec{r}) = \sum_{j=1}^{N} \phi_j \varphi_j(\vec{r}) \tag{25}$$

$$\mathrm{T}(\vec{r},t) = \sum_{j=1}^{N} T_j(t)\varphi_j(\vec{r}) \tag{26}$$

where ϕ_j and $T_j(t)$ are the value of the photon density $\Phi(\vec{r})$ and the temperature $T(\vec{r},t)$ at the j-th node, respectively. $\varphi_j(\vec{r})$ is the nodal FEM basis function. Substituting each approximate solution with the test function $v = \varphi_i(\vec{r})$ into the weak form equation (23) and (24), respectively, gives:

$$\sum_{j=1}^{N} \phi_j \int_{\Omega} D\ (\nabla\varphi_j(\vec{r}).\nabla\varphi_i(\vec{r}))d\Omega + \sum_{j=1}^{N} \phi_j \int_{\Omega} \mu_a\ (\varphi_j(\vec{r}).\varphi_i(\vec{r}))\, d\Omega = \int_{\Omega} S\varphi_i(\vec{r})\mathrm{d}\Omega \tag{27}$$

$$\sum_{j=1}^{N} \frac{\partial T_j(t)}{\partial t} \int_{\Omega} \rho c(\varphi_j(\vec{r}).\varphi_i(\vec{r}))\, d\Omega + \sum_{j=1}^{N} T_j(t) \int_{\Omega} k\, (\nabla\varphi_j(\vec{r}).\nabla\varphi_i(\vec{r}))d\Omega = \int_{\Omega} Q_s\varphi_i(\vec{r})\mathrm{d}\Omega \tag{28}$$

Consequently, the diffusion and heat equations in the FEM framework can be written in a matrix notation as:

$$[A+B]\phi = S$$
$$\left[M\frac{\partial}{\partial t} + K\right]T = \mathrm{Q}_s \tag{29}$$

The term on the left-hand side of equation (29), A, B, M, and K are matrices of size $[N \times N]$. The elements of these matrices are given by:

$$\begin{aligned} A_{ij} &= \int_{\Omega} D.\nabla\varphi_j(\vec{r}).\nabla\varphi_i(\vec{r})d\Omega, \\ B_{ij} &= \int_{\Omega} \mu_{a}.\varphi_j(\vec{r}).\varphi_i(\vec{r})\, d\Omega, \\ M_{ij} &= \int_{\Omega} \rho c.\varphi_j(\vec{r}).\varphi_i(\vec{r})d\Omega, \\ K_{ij} &= \int_{\Omega} k\,.\nabla\varphi_j(\vec{r}).\nabla\varphi_i(\vec{r})d\Omega. \end{aligned} \tag{30}$$

The source terms on the right-hand side of equation (29), S and Q_s are vectors of length N. The elements of these vectors are given by:

$$\begin{aligned} S_i &= \int_{\Omega} S\varphi_i(\vec{r})\mathrm{d}\Omega, \\ Q_{s_i} &= \int_{\Omega} Q_s\varphi_i(\vec{r})\mathrm{d}\Omega. \end{aligned} \tag{31}$$

Therefore, the numerical solution of the PMI forward problem is obtained as follow:

$$[A+B]^{-1}S = \phi,$$
$$\left[M\frac{\partial}{\partial t} + K\right]^{-1} B\phi = T, \tag{32}$$

$$\phi = \begin{bmatrix} \phi_1 \\ \phi_2 \\ \vdots \\ \phi_N \end{bmatrix}, \qquad T = \begin{bmatrix} T_1 \\ T_2 \\ \vdots \\ T_N \end{bmatrix}.$$

where ϕ and T are the nodal solution vectors, from which the photon density is calculated first, and then plugged in the second equation to obtain the temperature change in the whole medium.

2.3.2 PMI inverse problem

PMI inverse problem is solved to recover the optical absorption distribution at each node in the FEM mesh using PMI internal temperature measurements. As a multi-wavelength modality, the optical absorption reconstruction algorithm, which is based on solving the PMI inverse problem, is used for each wavelength individually [67]. During the resolution of the PMI inverse problem, the optical absorption maps are obtained by iteratively minimizing the quadratic error between the experimental temperature map and the simulated obtained using the optical absorption μ_a [94]:

$$\Omega(\mu_a) = \underset{\mu_a}{arg\min} \sum_{n=1}^{N} (\mathcal{T}_n - T_n(\mu_a))^2 \tag{33}$$

where Ω is the objective function to be minimized, $\mathcal{T}$ is the temperature map acquired experimentally, and T is the simulated temperature map calculated by the PMI forward problem using the optical absorption μ_a. N is the number of the FEM mesh nodes.

Solving the PMI inverse problem requires the construction of a matrix relating variations in the absorption coefficient at any point within the medium to their induced variations in the temperature measurements. This matrix is called the sensitivity matrix or the Jacobian matrix. One approach to obtain the Jacobian matrix is the perturbation theory based on calculating the induced

change in the temperature T at all the FEM nodes due to a small perturbation of the absorption μ_a at one of the nodes. This theory can be expressed by a Taylor series as follow [23, 95]:

$$T_{ij}(\mu_{a1}) = T_{ij}(\mu_{a0}) + \frac{\partial T(\mu_{a0})}{\partial \mu_a}(\mu_{a1} - \mu_{a0}) + \frac{1}{2!}\frac{\partial^2 T(\mu_{a0})}{\partial {\mu_a}^2}(\mu_{a1} - \mu_{a0})^2 + \cdots \tag{34}$$

where μ_{a0} and μ_{a1} are the initial and the perturbed optical absorption, respectively.

The elements of the Jacobian matrix can be obtained by considering only the first order term in equation (34):

$$J_{ij} = \frac{\partial T(\mu_{a0})}{\partial \mu_a} = \frac{T_{ij}(\mu_{a1}) - T_{ij}(\mu_{a0})}{\mu_{a1} - \mu_{a0}} \tag{35}$$

where J_{ij} is the element in the i^{th} row and j^{th} column of the Jacobian matrix that represents the change in temperature at node i caused by a variation in the absorption at node j. Since PMI utilizes MTR to acquire measurements from the whole volume of the medium, temperature measurements will be available at all the nodes of the FEM mesh. Therefore, the size of the Jacobian matrix in PMI case is $[N \times N]$ which can be constructed as follow:

$$J = \begin{bmatrix} \frac{\partial T_1}{\partial \mu_{a1}} & \cdots & \frac{\partial T_1}{\partial \mu_{aN}} \\ \vdots & \ddots & \vdots \\ \frac{\partial T_N}{\partial \mu_{a1}} & \cdots & \frac{\partial T_N}{\partial \mu_{aN}} \end{bmatrix} \tag{36}$$

Equation (35) can be written as follow:

$$\Delta\mu_a = J^{-1}\Delta T \tag{37}$$

This equation shows that the update on the absorption $\Delta\mu_a$ can be obtained by inversion the Jacobian square matrix. $\Delta\mu_a$ and ΔT are vectors of the size $[N \times 1]$, and J^{-1} is a square matrix of size $[N \times N]$. In certain cases, some measurements would be discarded from the measurement vector ΔT reducing its size to $[M \times 1]$. The removed measurements usually correspond to the MRT

measurements that are prone to error such as the measurement below the MRT noise level, or the ones performed at fatty tissue [96]. Consequently, the Jacobian matrix becomes of size $[M \times N]$, which requires utilization of dedicated non-square matrix inversion methods. In this thesis, the PMI inverse problem is solved using the algorithm of Levenberg–Marquardt where the unknown $\Delta\mu_a$ is updated iteratively by [97, 98]:

$$\Delta\mu_a = (J^T J + \gamma I)^{-1} J^T (\mathcal{T} - T(\mu_a)) \tag{38}$$

where J^T is the transpose of the Jacobian matrix J, γ is the regularization parameter which is required to stabilize the matrix inversion process. $\mathcal{T}$ is the MRT temperature measurements vector, and T is the vector containing the simulated temperature values calculated by the PMI forward problem using the initial optical absorption μ_a, and I is the identity matrix of the same size as $(J^T J)$. Using this method, the calculated $\Delta\mu_a$ is used to update the estimation of the absorption coefficient μ_a in each iteration that will be later used to solve the PMI forward problem to compare the simulated map with the experimental one. The iterative process continues until the difference between the measured and simulated temperature maps, also known as reconstruction error, is minimized. The absorption distribution μ_a corresponding to the smallest reconstruction error will be accepted as a solution to the inverse problem as described in Figure 4. This recovered absorption represents the total absorption of the medium, as expressed in equation (2). To differentiate between the contribution of each individual chromophore within the medium, their concentrations are recovered using multi-wavelength approaches as described below.

2.3.3 Reconstruction of chromophore concentration

Two approaches can be used to resolve the chromophore concentrations from PMI temperature measurements acquired at multiple wavelengths. The first approach is based on

recovering the optical absorption distribution at each wavelength individually, and then use these recovered absorption maps to calculate the chromophore concentrations through a separate minimization process. This method will be referred to as the PMI conventional method in the rest of the thesis. On the other hand, the concentration can be reconstructed directly from the PMI temperature measurements by incorporating spectral *a priori* constraints. This method is called PMI direct method for concentration recovery.

2.3.3.1 PMI conventional method

Once the tissue optical absorption map is obtained at each wavelength using the PMI inverse problem, chromophore concentrations are then recovered using the modified Beer-Lambert Law equation (7), which states that the recovered absorption at each node in the FEM mesh is a linear combination of the product of the extinction coefficient of each chromophore and its concentration [99-102], this can be expressed in a matrix notation as:

$$\begin{bmatrix} \mu_{a_{tot}}(\lambda_1) \\ \vdots \\ \mu_{a_{tot}}(\lambda_\Lambda) \end{bmatrix} = ln10 \begin{bmatrix} \varepsilon_1(\lambda_1) & \cdots & \varepsilon_P(\lambda_1) \\ \vdots & \ddots & \vdots \\ \varepsilon_1(\lambda_\Lambda) & \cdots & \varepsilon_P(\lambda_\Lambda) \end{bmatrix} \begin{bmatrix} C_1 \\ \vdots \\ C_P \end{bmatrix} \tag{39}$$

where $\mu_{a_{tot}}(\lambda)$ is the total recovered absorptions at wavelength λ. The size of the total absorption vector is $[\Lambda \times 1]$, with Λ being the number of applied wavelengths. $\varepsilon_P(\lambda)$ is the extinction coefficient of a specific chromophore at wavelength λ. The size of the wavelength-dependent extinction coefficient matrix is $[\Lambda \times P]$, where P is the number of considered chromophores in the object. C is the unknown chromophore concentration assembled in a vector with size $[P \times 1]$. This system of linear equations is solved by a nonnegative linear least square minimization to recover the concentration of all individual chromophores in the medium at each node of the FEM mesh [67].

2.3.3.2 PMI Direct method

The spectrally-constrained chromophore concentration reconstruction algorithm was first introduced by Corlu *et al*. to recover chromophore concentrations from continuous wave DOT measurements [103]. When tested on DOT, this method showed high performance on improving the accuracy of the recovered chromophore concentrations, suppressing artifacts, and reducing the cross talk between different chromophore concentration maps [100, 104, 105]. By applying this method to PMI, the MRT temperature maps acquired experimentally at each wavelength are used in the PMI new algorithm to directly recover the chromophore concentration maps. Figure 6 shows the diagram of PMI direct algorithm.

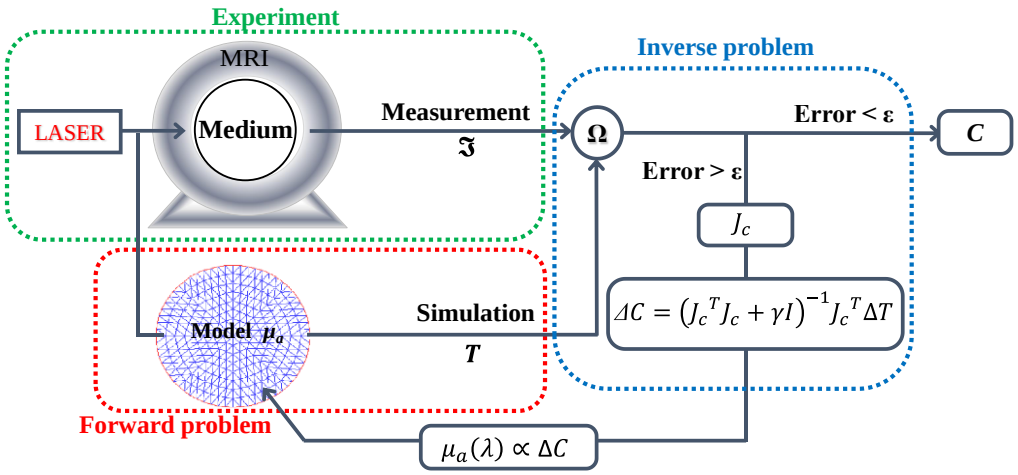

Figure 6: Diagram of the PMI direct chromophore concentrations recovery algorithm.

Similar to the conventional method, the first part in this approach is generating the simulated temperature map at each wavelength by solving the PMI forward problem using FEM. Then, the quadratic difference between the measured MRT temperature and the simulated ones is minimized iteratively in order to directly obtain the chromophore concentrations, for all the wavelengths collectively, according to the following objective function [106, 107]:

$$\Omega(C) = \underset{C}{arg\min} \sum_{\lambda=1}^{\Lambda} \sum_{n=1}^{N} \left(\Im_n - T_n(\mu_a)\right)^2 \tag{40}$$

The unknown chromophore concentrations are updated iteratively with the Levenberg–Marquardt minimization method by [20, 49, 55, 108]:

$$\Delta C = (J_c^T J_c + \gamma I)^{-1} J_c^T \Delta T \tag{41}$$

where ΔC is the update in the chromophore concentration, J_c is the spectrally-constrained Jacobian matrix, $\Delta T = (\Im - T(\mu_a))$, γ is the regularization parameter and I is the identity square matrix. The size of the spectrally-constrained Jacobian J_c matrix is $[\Lambda N \times PN]$. ΔC and ΔT are vectors of size $[PN \times 1]$, and $[\Lambda N \times 1]$, respectively.

$$\Delta C = \begin{bmatrix} \Delta C_1^1 \\ \vdots \\ \Delta C_N^1 \\ \vdots \\ \vdots \\ \Delta C_1^P \\ \vdots \\ \Delta C_N^P \end{bmatrix}, \ \Delta T = \begin{bmatrix} \Delta T_1^{\lambda_1} \\ \vdots \\ \Delta T_N^{\lambda_1} \\ \vdots \\ \vdots \\ \Delta T_1^{\lambda_\Lambda} \\ \vdots \\ \Delta T_N^{\lambda_\Lambda} \end{bmatrix}, and \quad J_c = \begin{bmatrix} J_{c1,\lambda 1} & J_{c2,\lambda 1} \cdots & J_{cP,\lambda 1} \\ J_{c1,\lambda 2} & J_{c2,\lambda 2} \cdots & J_{cP,\lambda 2} \\ \vdots & \vdots & \vdots \\ J_{c1,\lambda \Lambda} & J_{c2,\lambda \Lambda} & J_{cP,\lambda \Lambda} \end{bmatrix} \tag{42}$$

The spectrally-constrained Jacobian J_c describes the variation in the temperature caused by a small variation in the chromophore concentration, and can be obtained as follow [109]:

$$J_c = \frac{\partial T}{\partial c} = \frac{\partial T}{\partial \mu} \frac{\partial \mu}{\partial c} = J_{\mu_a} \otimes \varepsilon \tag{43}$$

where $J_{\mu_a} = \frac{\partial T}{\partial \mu}$ is the optical absorption Jacobian described in equation (35). ε is the known chromophore extinction coefficient, which is used as constraints in PMI direct algorithm, and $\otimes$ is the Kronecker tensor product [110].

Chapter 3: Validation of multi-wavelength PMI with simulation studies

Simulation studies were performed to validate the feasibility of the multi-wavelength PMI technique to resolve the concentration of multiple chromophores using the conventional and the direct methods, as described in this chapter.

3.1 Building the numerical phantom

This simulation study is conducted on a numerical mouse shaped geometry, which is extracted from a transverse cross-section of a 3-D mouse model, Figure 7 (a). The width and height of the used geometry is 28 mm and 25 mm, respectively. Two inclusions, 4 mm in diameter, were embedded 5.3 mm below the upper surface of the numerical geometry (surface to center distance) and located 5.5 mm apart (center to center distance). Figure 7 (b) shows the used cross-section and the two inclusions: Inclusion 1 containing Dye 1 (blue) and Inclusion 2 containing Dye 2 (red). Since the inclusions are placed in the upper part of the phantom, it was enough to perform the study with a single laser source from the top side as shown by the arrow (S), Figure 7 (b). Five wavelengths were used to illuminate the numerical phantom in this study. Finally, a finite element mesh consisting of 4212 nodes and 8118 triangular elements was generated on the numerical geometry using MATLAB, Figure 7 (c).

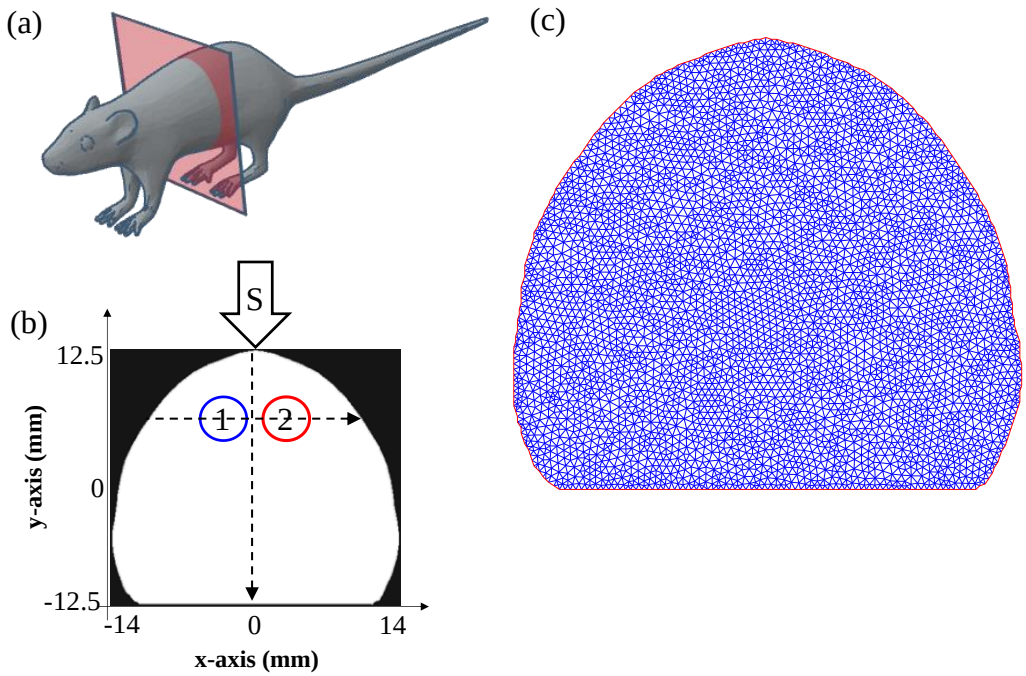

Figure 7: (a) The numerical mouse model and the orientation of the used transverse cross-section (the red plane). (b) The binary mask of the numerical phantom containing two inclusions. Inclusion 1 contains Dye 1 is on the left (blue) and Inclusion 2 that contains Dye 2 is on the right (red). The laser used to heat up the phantom is illustrated with an arrow at the top of the phantom (S). (c) The 2-D FEM generated on the mouse geometry.

The numerical phantom mimics a biological tissue containing fat, water and to simulate the presence of additional chromophores as hemoglobin in its both forms, two NIR absorbing dyes NIR782E and NIR869A (QCR Solutions Corp, USA) were used to fill Inclusion 1 and 2, respectively. The optical properties of fat and water were obtained from literature [111, 112]. For this simulation study, the concentration of the NIR dyes used are (C_{Dye1}=2.4%, C_{Dye2}=2.2%). Based on the concentration value and the known extinction coefficient values, the absorption coefficient for each chromophore at each wavelength is calculated using Equation (7). The absorption spectrum of Dye 1 and Dye 2 are shown in Figure 8 (a). The absorption spectra of Inclusion 1, Inclusion 2, and the background of the phantom are illustrated in Figure 8 (b). The absorption spectrum of the background is the sum of the water and fat spectra as well as a dye that has a flat spectrum with absorption coefficient equal to 0.01 mm^{-1}. The spectra of Inclusion 1 and Inclusion

2 are the result of adding the absorption coefficients of fat, water, and the specific dye at a given inclusion position.

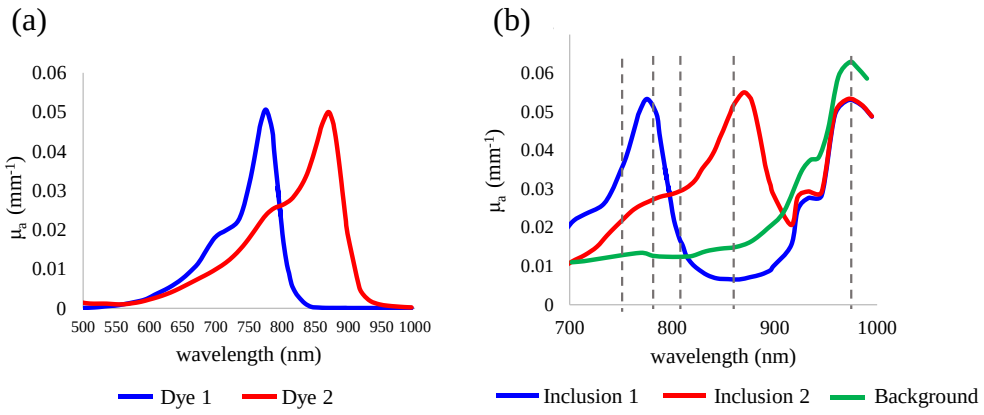

Figure 8: (a) The absorption spectra of Dye 1 (blue), Dye 2 (red). (b) The absorption spectra of the phantom: Inclusion 1 (blue), Inclusion 2 (red) and Background (green) [113].

The absorption coefficient at each wavelength of Inclusion 1, Inclusion 2, and the background are shown in Table 1.

Table 1: Absorption coefficients of Inclusion 1, Inclusion 2, and the phantom's background at each wavelength [113].

	Real absorption coefficient (mm^{-1})				
	760 nm	**780 nm**	**808 nm**	**860 nm**	**980 nm**
Inclusion 1	0.043	0.049	0.017	0.007	0.052
Inclusion 2	0.024	0.028	0.029	0.052	0.052
Background	0.014	0.013	0.012	0.015	0.062

In this study, the scattering was set using Intralipid® 20% (Fresenius Kabi, SE). The reduced scattering coefficient of the numerical phantom was adjusted to be equal to 0.8 mm^{-1}. The density and specific heat were set to be the same as water values 1000 $kg.m^{-3}$ and 4200 $J.(kg.℃)^{-1}$, respectively. The thermal conductivity, k, was set to be 0.58×10^{-3} $W.(mm.℃)^{-1}$.

3.2 Generation of synthetic measurements

The first step in this simulation study consists in generating the simulated temperature maps at each wavelength using the PMI forward solver. The first two rows of Figure 9 show the simulated temperature maps corresponding to a 10-second heating period with a NIR laser over an 8 mm in diameter illumination spot.

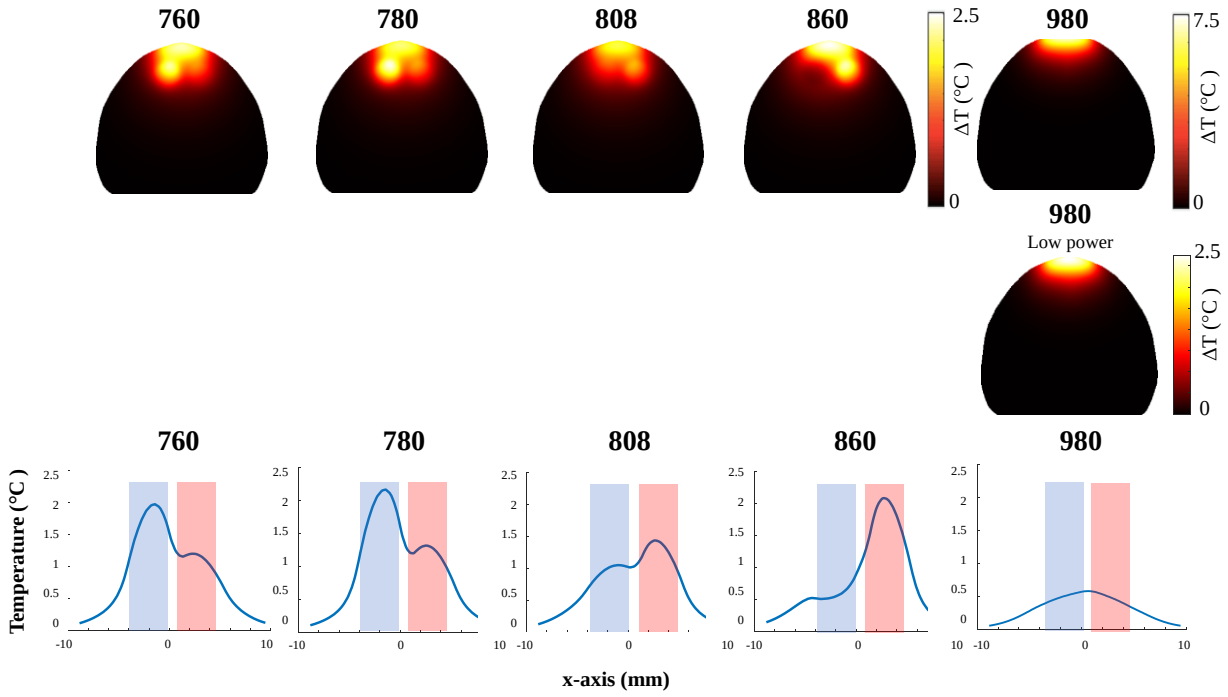

Figure 9: The temperature maps using equal power at each wavelength (first row), and the temperature map of 980 nm at low power (second row). Third row shows the temperature profiles carried along the line passing through the center of the two inclusions along the x-axis at each wavelength.

Due to the illumination from the top, we can observe a higher increase in the temperature around the source region. An equal laser power was used to generate those temperature maps, Figure 9 (first row). Utilizing equal power results of increase in the temperature around the source area of around 2.5 °C for the first four wavelengths (760, 780, 808, and 860 nm), while it reached 7.5 °C for wavelength 980 nm. This higher increase in temperature at 980 nm is due to the fact

that the background of the phantom absorption is principally governed by the absorption of the water at 980 nm. However, it has been demonstrated that the first degree skin burns happen when the temperature of the skin rises between 7 to 18 °C [114]. Therefore, to avoid skin injuries, the power of laser 980 nm was decreased by a ratio of 3 to decrease the temperature change from 7.5 to 2.5 °C. Figure 9 (second row) shows the temperature map at 980 nm after using the low power.

Utilizing low laser power would result of low increase in temperature and hence low signal-to-noise ratio. The noise level of the used MRT has been previously studied and found to be equal to 0.1 °C [50]. The performance of PMI depends on its ability to warm up the medium above the MRT noise level.

To study the temperature propagation with distance in this phantom, temperature profile was performed at the center of the phantom along the y-axis (vertical arrow in Figure 7(b)) for all the used five wavelengths, Figure 10. These profiles show that the maximum temperature increase was ranging between 2 and 2.5 °C demonstrating that multi-wavelength PMI is safe during *in vivo* imaging. The MRT noise level is illustrated with blue shadowed region in Figure 10.

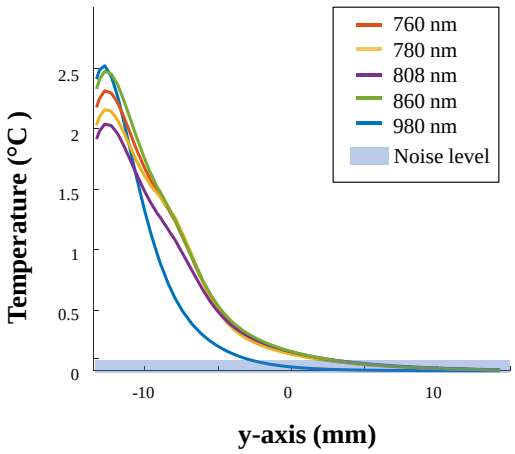

Figure 10: Temperature profiles at the center of the phantom along the y-axis at all five wavelengths.

The temperature profiles show that temperature is exponentially decreasing with depth. The temperature profile corresponding to the laser at 980 nm exhibits the shortest depth penetration (~ 10 mm). This is due to the high absorption of light at this wavelength as well as the use of lower laser power to avoid the burn injury to the skin. This short penetration depth is not a problematic in this specific case since the inclusions are located close to the illumination position. Nevertheless, the depth penetration can be increased by illuminating the phantom from multiple sides to increase the temperature of the whole medium above the noise level, as proved in a previous study [55].

The temperature profiles of the first four laser wavelengths (760-860 nm) show a small bent as the profile is passing between the two inclusions. On the other hand, the profile is smoother for laser 980 nm. This increase in temperature near the inclusions position is due to the high absorption contrast between at least one inclusion and the background. Table 2 summarizes the optical absorption contrast of Inclusion 1 and Inclusion 2 to the background at each wavelength.

Table 2: Optical absorption contrast of Inclusion 1 and 2 to the background at each wavelength [113].

	Absorption contrast				
	760 nm	**780 nm**	**808 nm**	**860 nm**	**980 nm**
$\mu_a\left(\frac{Inclusion\ 1}{Background}\right)$	3.07	3.77	1.42	0.47	0.84
$\mu_a\left(\frac{Inclusion\ 2}{Background}\right)$	1.71	2.15	2.42	3.47	0.84

To study the wavelength-dependent temperature variation within the phantom, temperature profiles carried along the line passing through the center of the two inclusions along the x-axis (horizontal arrow in Figure 7 (b)) were performed, Figure 9 (third row). The blue and red shadowed regions represent the position of Inclusion 1 and Inclusion 2, respectively.

Temperature maps and profiles at laser 760 nm and 780 nm, Figure 9, show that the temperature increase in Inclusion 1 is higher than in Inclusion 2 since the absorption contrast of Inclusion 1 is larger than the one of Inclusion 2. To the right of the isosbestic point for these two

inclusions at 808 and 860 nm, Inclusion 2 had higher temperature increase than Inclusion 1, which agrees with the spectra of the two dyes. At 860 nm, Inclusion 1 had lower temperature increase even than the background since at this wavelength Inclusion 1 had the lowest optical absorption value. At 980 nm Figure 9 (second row), the temperature increase within the inclusions was lower than the change at the other wavelengths even though their absorption was higher, Table 1. This is because the absorption of the background at this wavelength was high resulting in a poor penetration of light. Therefore, this weak increase in temperature was due to the low number of photons reaching the inclusions.

All temperature maps in Figure 9 already reveal the position of the inclusions except for laser 980 nm. Nevertheless, the position of the inclusions is still localized during the calculation of the temperature difference ΔT, Figure 11.

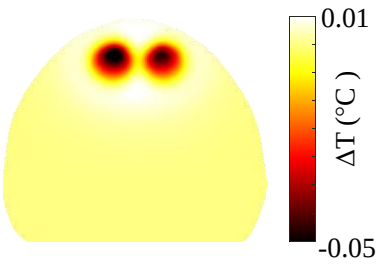

Figure 11: The map of temperature difference between the homogenous and heterogeneous case when using laser 980 nm.

3.3 Reconstruction of chromophore concentrations

The wavelength-dependent temperature measurements were used to recover chromophore concentration in two different approaches. First, the conventional method where the absorption coefficient maps are recovered to be used in the concentration recovery algorithm. Second, the temperature measurements are directly used to recover the concentration of the chromophores in the numerical phantom.

3.3.1 The conventional method

3.3.1.1 Recovering the absorption maps

PMI image reconstruction algorithm is used, for each wavelength, to recover the absorption coefficient map at the same wavelength. Figure 12 shows the real (1st row) and recovered (2nd row) absorption maps at each wavelength.

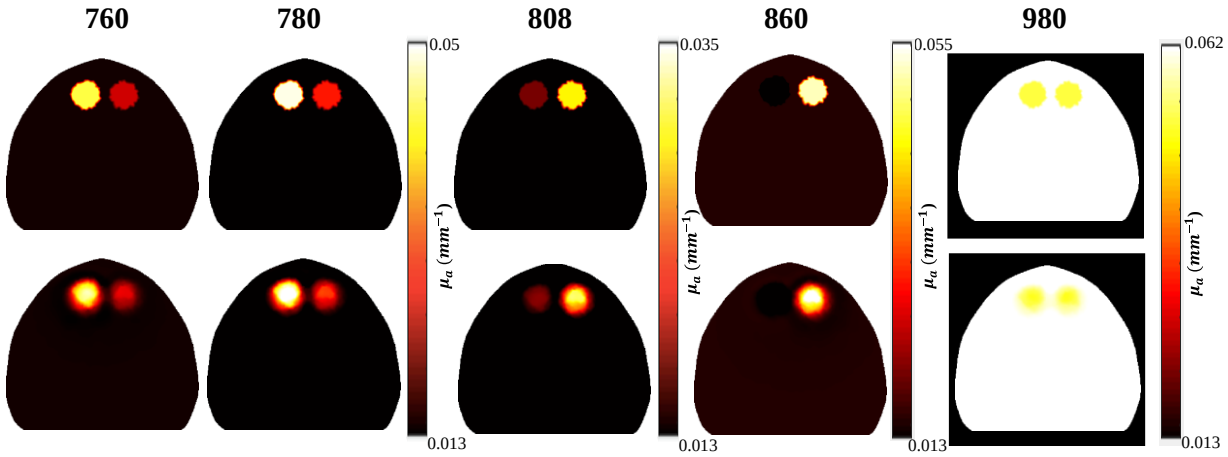

Figure 12: The real absorption coefficient maps (first row) and the high-resolution reconstructed absorption maps (second row) at each wavelength.

The absorption maps show that PMI is able to provide high-resolution absorption maps with high quantitative accuracy. In all maps, the inclusions were successfully resolved with average percentage error of 6% and 2.5% for inclusion 1 and inclusion 2, respectively. To compare the recovered with the real absorption coefficient visually, a profile carried along the x-axis and passing through the center of the two inclusions (horizontal arrow in Figure 7 (b)) was performed at each wavelength, Figure 13.

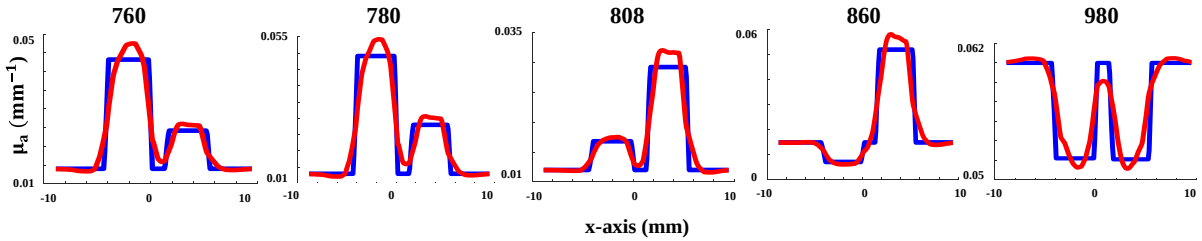

Figure 13: Absorption profiles carried along the x-axis and passing through the center of the two inclusions. The real absorption (blue line) and the recovered absorption (red line).

A quantitative quality evaluation is reported as the average and standard deviation of the reconstructed absorption value within the two inclusions, Table 3.

Table 3: Mean and standard deviation of the reconstructed absorption coefficients of the phantom.

	Recovered absorption coefficient (mm^{-1})				
	760 nm	**780 nm**	**808 nm**	**860 nm**	**980 nm**
Inclusion 1	0.0431±0.0029	0.0487±0.0036	0.0168±0.0004	0.008±0.0007	0.0576±0.0013
Inclusion 2	0.0239±0.0016	0.0276±0.0024	0.0289±0.0025	0.052±0.0051	0.0575±0.0012

3.3.1.2 Recovering the concentration maps.

After reconstructing the absorption maps at all five wavelengths, the concentration maps of the two dyes are recovered with an error of 3.3% and 3.2%, for Dye 1 and Dye 2 respectively, Figure 14.

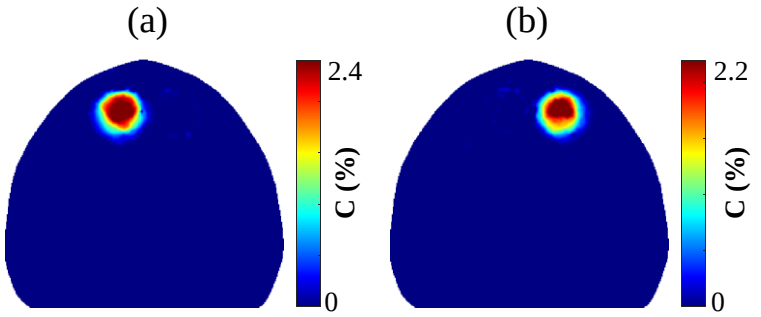

Figure 14: The recovered concentration maps of (a) Dye 1 and (b) Dye 2 using PMI conventional method.

3.3.2 The direct method

3.3.2.1 Recovering the concentration maps

Using PMI direct method, the concentration is recovered directly from the temperature measurements using chromophores extinction coefficients as *a priori* information. Using this method, the concentration maps of the two dyes are recovered with an error of 2.8% and 1.8%, for Dye1 and Dye 2 respectively, Figure 15.

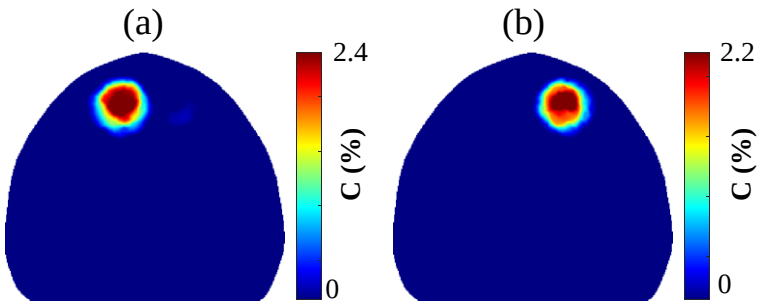

Figure 15: The recovered concentration maps of (a) Dye 1 and (b) Dye 2 using PMI direct method.

For a better comparison between the performance of PMI concentration reconstruction methods, a profile carried along the x-axis and passing through the center of the two inclusions (horizontal arrow in Figure 7 (b)) was performed for Dye 1 and Dye 2 concentration maps (Figure 14 and Figure 15) and compared with the real value of the concentration of each dye, Figure 16.

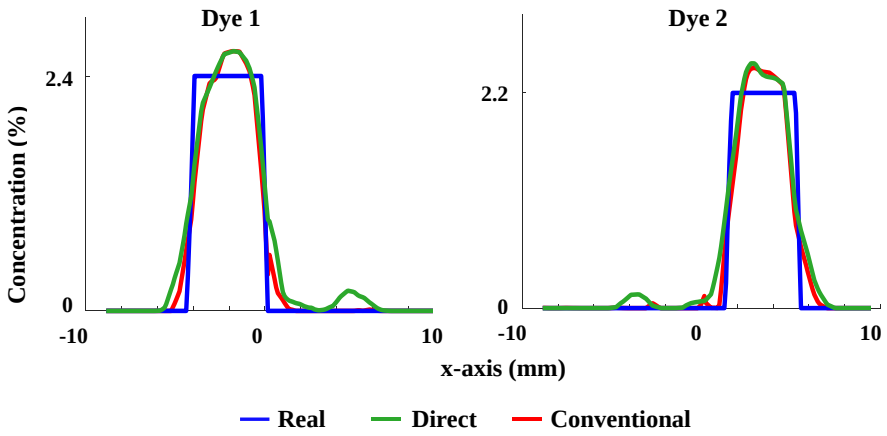

Figure 16: Concentration profiles carried along the x-axis and passing through the center of the two inclusions for Dye 1 and Dye 2 concentration maps. The real concentration (blue line), the recovered concentration using the direct method (green line) and the conventional method (red line).

A comparable performance on recovering the concentration is noticed using both methods, PMI conventional and direct methods. No artifacts nor cross talk are observed on the recovered concentration maps of Dye 1 and Dye 2. The mean and standard deviation of the recovered concentration of Dye 1 and Dye 2 using both PMI reconstruction methods are presented in Table 4.

Table 4: Mean and standard deviation of the reconstructed concentration of Dye 1 and Dye 2 using both PMI reconstruction methods.

	Recovered concentration (%)	
	Conventional	**Direct**
Dye 1	2.32±0.24	2.33±0.21
Dye 2	2.13±0.29	2.16±0.24

The results presented on this simulation study validated that multi-wavelength PMI technique is able to resolve multiple chromophore concentrations within the same medium with high-resolution and high quantitative accuracy, using both the conventional and direct method.

Chapter 4: Multi-wavelength PMI system development and experimental setup

Single-wavelength PMI showed high performance on recovering the distribution of the absorption coefficient with high-resolution and quantitative accuracy [52, 53, 55]. However, single-wavelength PMI was only employed to recover the total absorption of the imaged tissue. Over the last decades, several studies demonstrated the ability of multi-wavelength optical imaging in recovering the tissue chromophore concentrations, which is directly related to cancer screening and characterization [100, 115]. In fact, it has been widely demonstrated that recovery of endogenous and exogenous chromophore concentrations provides crucial information to assess angiogenesis and monitor the hypermetabolism state of tumorous tissue [12, 13]. Therefore, to leverage this imaging ability we developed the first multi-wavelength PMI system and upgraded the PMI technique from single to multiple wavelengths. The multi-wavelength PMI hardware and software development details are presented in this chapter.

4.1 Instrumentation

The multi-wavelength PMI system was entirely home-built. This system is composed of three main components: laser system, temperature management system, and a control computer. Each component is carefully designed and customized to fulfil its intended functionality. The schematic diagram of the multi-wavelength PMI experimental setup is presented in Figure 17. Briefly, during PMI data acquisition, the imaged object is placed inside the imaging interface in the MRI bore. The object is illuminated by the laser light generated by the PMI laser system (red block). Light is transported from the PMI laser system which is placed in the control room to the imaging interface via optical fibers. To monitor and control the temperature of the laser system, a

temperature management system (yellow block) has been also developed. Lastly, a dedicated LabVIEW-based software has been implemented to automatically control all the operating functionalities (blue block).

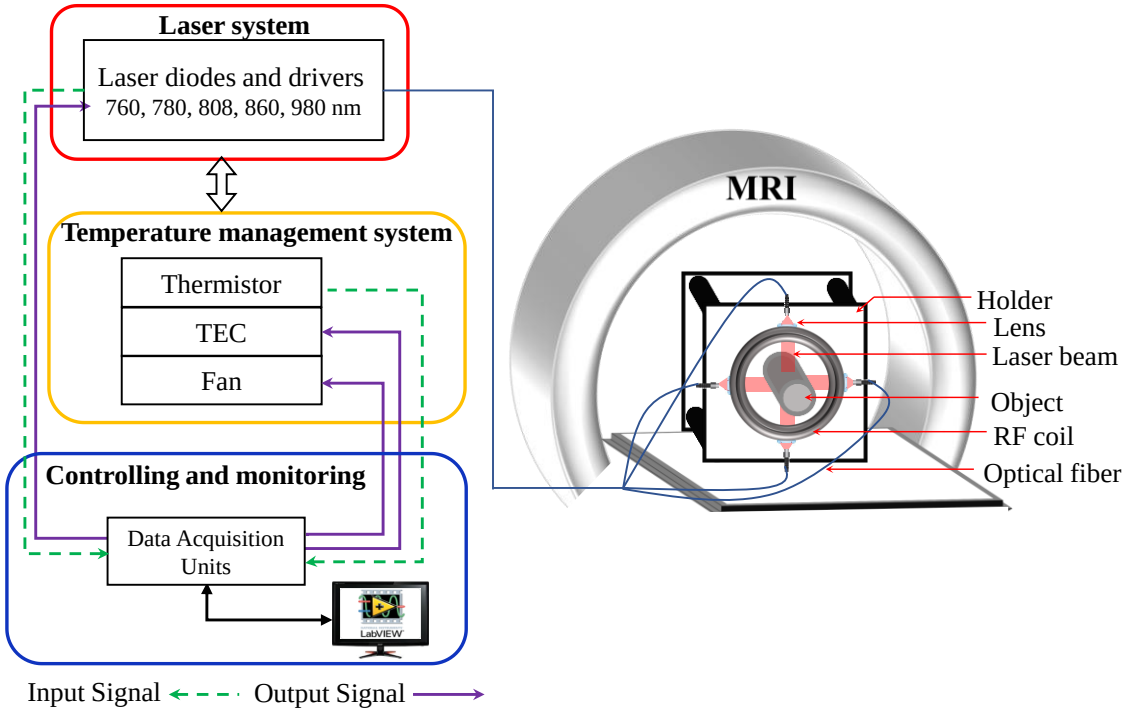

Figure 17: Schematic diagram of the multi-wavelength PMI system, mainly composed of: Laser system (red), temperature management system (yellow), and controlling and monitoring (blue).

To enable the mobility of the PMI system, all the components are assembled in a compact cart 18″ × 24″ × 32″ that fits the MRI control room, Figure 18. The components of the system are described in detail in the following sections.

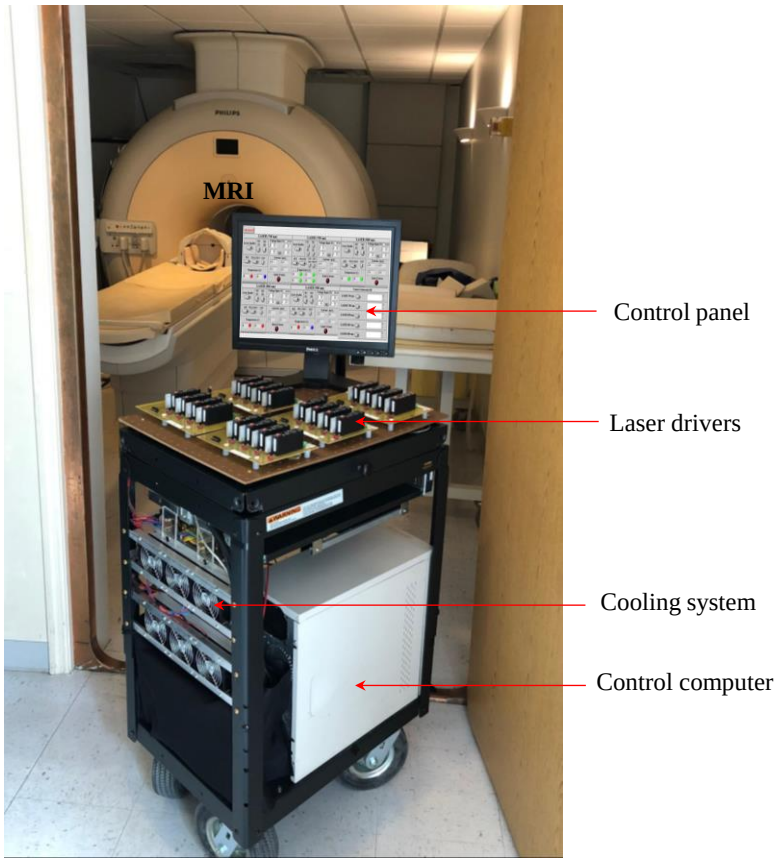

Figure 18: Photograph of the multi-wavelength PMI system.

4.1.1 Laser system

The multi-wavelength PMI system is designed to operate at five different laser wavelengths ranging between 760 to 980 nm. Each one of these laser diodes is driven with a dedicated laser diode driver.

4.1.1.1 Laser diodes

The multi-wavelength PMI system utilizes continuous wave laser diodes as a light source to illuminate the imaged object. PMI laser diodes emit in the NIR spectral window: 760, 780, 808, 860, and 980 nm. These specific wavelengths were selected to recover the concentration of the main endogenous chromophores that absorb NIR light in the biological tissue as well as the

potential used exogenous contrast agents. The choice of these wavelengths is based on the fact that each of these chromophores has a unique absorption spectrum in the NIR window as shown in Figure 3, section 2.2.

The number of the utilized wavelengths is chosen based on the number of the chromophores of interest to be recovered. For example, three wavelengths (760, 808, 860 nm) are enough to differentiate between only oxy- and deoxy- hemoglobin. While to assess the water content, the 980 nm wavelength is needed since the water has an absorption peak around 980 nm. Another example would be the use of a 780 nm for the recovery of the distribution of ICG, which has an absorption peak around this wavelength.

The laser diodes have been purchased from different manufacturers; thus, their optical and electrical specifications in terms of the operating current, output power, as well as package dimensions are different. Figure 19 shows the laser diodes used in the system: a) 760 nm (5 W; LDX Optronics Inc., Maryville, TN, US), b) 780 nm (3 W; Wavespectrum Laser group Ltd., Beijing, China), c) 808 nm (7 W; Focuslight Inc., Xi'an, China), and d) 860 nm (4.6 W; LDX Optronics Inc., Maryville, TN, US), and e) 980 nm (4.5 W; LDX Optronics Inc., Maryville, TN, US).

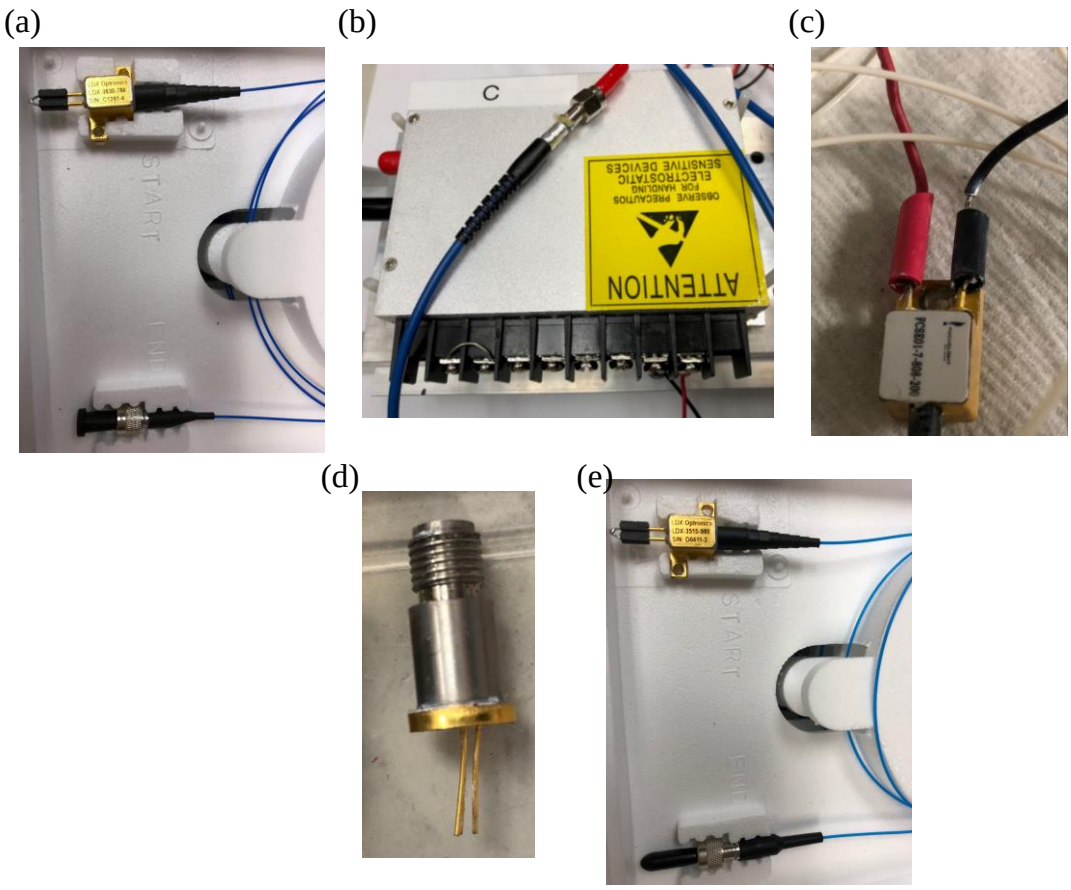

Figure 19: Laser diodes used in the multi-wavelength PMI system. (a) 760 nm, (b) 780 nm, (c) 808 nm, (d) 860 nm, and (e) 980 nm.

Figure 19 shows that the type of the laser diodes that operate at 760, 808, and 980 nm is 2-Pin package coupled with 400, 200, 200 μm fiber, respectively. The 780 nm receptacle package is coupled with 200 μm fiber. While a 400 μm detachable fiber is used to deliver the light from the 860 nm 9 mm SMA package. All the fiber optic connectors used in our system are SMA connectors.

To allow heating the subject from multiple sides as shown in Figure 17, four laser diodes are used for each wavelength resulting of total of 20 laser diodes hosted in the multi-wavelength PMI system. The 20 laser diodes were divided into two groups based on their package type. The first group consists of four receptacle packages of 780 nm laser wavelength, and this group will be

referred to as Group-1 through the chapter. The remaining 16 laser diodes were placed together in the same group due to their small package dimensions, which will be referred to as Group-2.

4.1.1.2 Laser diode drivers

The 20 laser diodes are operated by laser diode drivers (PLD5000, Wavelength Electronics Inc., Bozeman, MT, US). These drivers require a 5-volt power supply while providing a maximum of 5 A output current. Each laser diode is connected to one driver through a 14-AWG cable. Those drivers are grouped according to their operating wavelength and installed at the top of the system allowing an easy access to users, Figure 20.

Figure 20: Picture of the laser diode drivers. The drivers are grouped into five groups of four drivers based on their corresponding operating wavelength.

This easy access configuration enables the users to control the drivers manually. For safety purposes, the system was designed to have a manual override control that allows the users to quickly turn off the lasers in case of emergency. The override setups composed of AND gate and manual switches that were mounted on each circuit and used as enable switch, Figure 21.

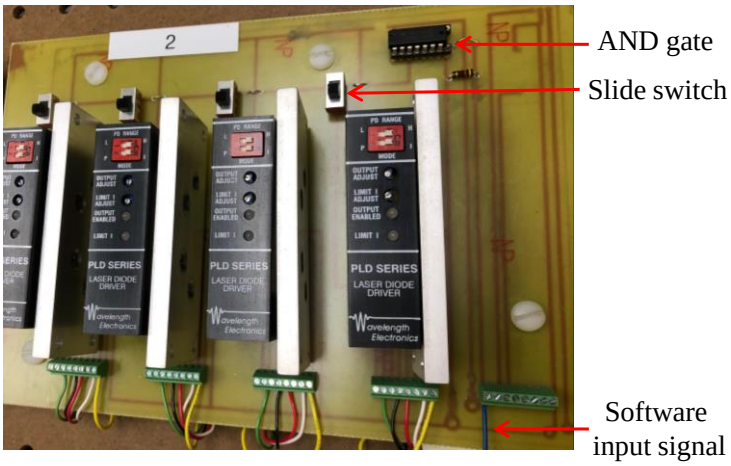

Figure 21: Top view of a representative laser drivers board showing the AND gate and the manual switch used to manually control the drivers.

A schematic of the manual override circuit is shown in Figure 22. In this circuit, the resulted output signal from the AND gate goes through a manual switch to enable the laser diode driver output. The first input for this logic gate is obtained from a physical 5-volt power supply. The second input signal consists in an automated enable signal delivered by the LabVIEW software. This circuit allows to keep the laser output off unless both the manual switch and the software enable signal are on.

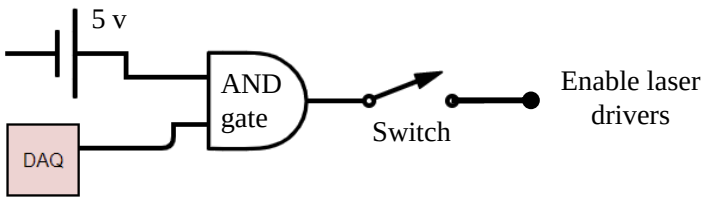

Figure 22: Diagram of the manual override circuit used in the multi-wavelength PMI system.

These laser diode drivers were manufactured with several features such as the “output current limit” of each driver, which is set manually using an on-board control to match the corresponding laser diode specifications. When the diode driver reaches the current limit, the

driver output will automatically switch off directly to protect the laser diode from over-current operation. A visual alert is available via a red status LED that turns on indicating that the driver reached the current limit. In addition, these drivers allow the user to adjust the output current either manually or using an analog signal. The latter was used in our system to automate the current control via our LabVIEW-based program software. More details regarding this automation process are presented in section 4.2.

4.1.2 Temperature management system

Since multi-wavelength PMI system employs high-power laser diodes, the increase in their operating temperature is inevitable. High operating temperature would cause a shift in the laser operating wavelength, increase the threshold current, and decrease the laser diode lifetime. Therefore, a temperature management system was implemented to monitor and control the operating temperature of the lasers.

First, the laser diodes are either mounted on (760, 808, and 980 nm) or drilled in copper plates (860 nm) to rapidly dissipate the generated operating heat, as in Group-2 Figure 23 (a) and (c). The copper plates are directly placed in contact with thermoelectric cooling (TEC) units (TEC1-12706; Hebei I. T. Co., Shanghai, China), which transfer the heat from the copper plates to a fan-cooled aluminum heatsink, Figure 23 (d). While the TEC units were placed directly under the laser diodes in Group-1, Figure 23 (b). The temperature of the laser diodes is continuously monitored using a thermistor (TH10K, Thorlabs Inc., Newton, NJ, US), Figure 23 (e).

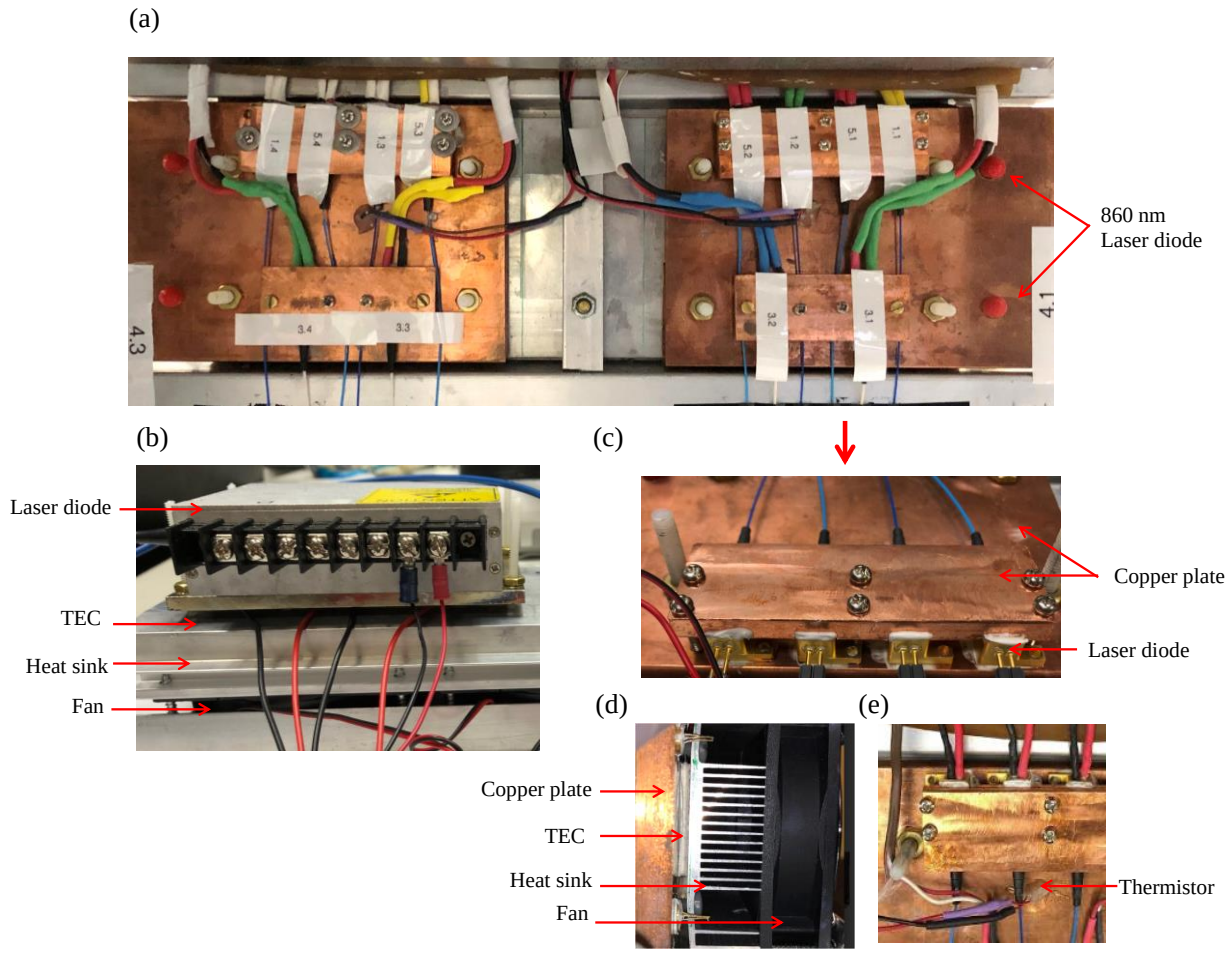

Figure 23: (a) Picture of the temperature management unit of laser diodes in Group-2. (b) Picture of the temperature management unit of one of the laser diodes in Group-1. (c) A zoomed-in picture of the temperature management unit of Group-2 showing the laser diodes sandwiched between two copper plates. (d) A side view of the temperature management unit. (e) A top view of the temperature management unit of Group-2 showing the thermistor inserted in the copper plate.

4.1.2.1 Temperature measurements (Thermistor)

Thermistors are resistors having a temperature-dependent resistance. Thermistors are used here to measure the temperature of the copper plates resulting from the dissipation of the operating temperature of the laser diodes. Briefly, any change in temperature induces a change in the thermistor resistance. This change causes a variation in the voltage measured across the thermistor. Consequently, the ability to perform accurate temperature measurements depends on the accuracy of this voltage measurement.

Technically, the temperature measurements circuit in the multi-wavelength PMI system has been built by connecting a thermistor (10 k.Ω at 25 °C) in series with a fixed 10 k.Ω resistor, Figure 24. The fixed resistor was used in series to be able to measure the voltage change, and hence the temperature. A combination of a 15-volt power supply and a voltage regulator (+12 v, 1A) is used to provide a constant and fixed voltage across the series connected thermistor and resistor. Then, the voltage measured across the thermistor is used to calculate the resistance at specific temperature, according to Ohm's law. Based on the thermistor specifications, the temperature is then processed by converting the calculated resistance to an absolute temperature value.

Six thermistors are used in our system. Four were provided by the manufacturer and were built in the 780 nm laser diodes (one thermistor in each diode). The remaining two were inserted in the copper plate to detect the temperature generated from the laser diodes in Group-2. A picture and a diagram of the temperature measurement circuit are shown in Figure 24. This circuit shows the fixed resistors (R1-R6), the thermistors (R7-R12), the voltage regulator, the power supply and the Data Acquisition (DAQ) device that is used to read the voltage across the thermistors.

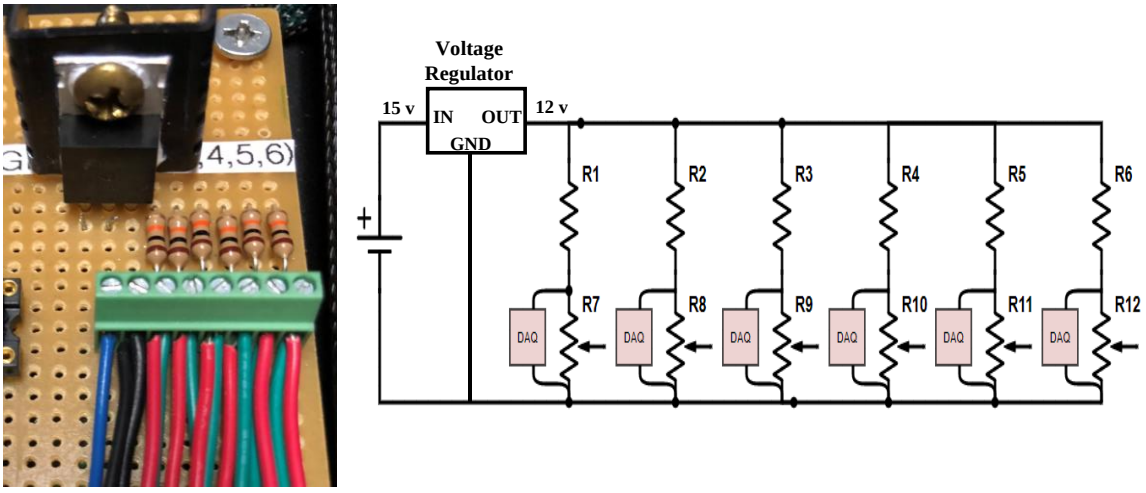

Figure 24: Picture of the temperature measurement circuit used in the multi-wavelength PMI system (left) and a diagram of the electric circuit showing the 10 kΩ resistors (R_1 -R_6), the thermistors (R_7 -R_{12}), the voltage regulator and its power supply (right).

4.1.2.2 Thermoelectric cooling units

Thermoelectric cooling (TEC) unit are used to transfer the heat from one side of the unit to the other side. TEC units are composed of a semiconductor material placed between two ceramic plates, and operate according to Peltier effect [116]. In the multi-wavelength PMI system, TEC units (15 v, 6.4 A) are used to cool down the laser diodes by placing the unit either directly below the laser diode (as in Group-1) or the copper plate to dissipate the excess heat from the laser diodes in Group-2. The operation of these TEC units is automatically controlled by the implemented PMI software and based on the temperature obtained by the thermistor.

Twelve TEC units are used in the multi-wavelength PMI system. Two units were placed under each 780 nm laser diode resulting of eight TEC units in total for Group-1. And four units were used for Group-2. Multiple 15-volt power supplies with a built-in remote ON-OFF control were used to manage the operation of the TEC units of each laser diode automatically. In Group-2, each two TEC units were operated using one power supply. Instead of using four power supplies for Group-1, an 8-channel relay is used to control the operation of the 8 TEC units. A picture and a schematic diagram of the TEC operation circuit used for Group-1 is shown in Figure 25.

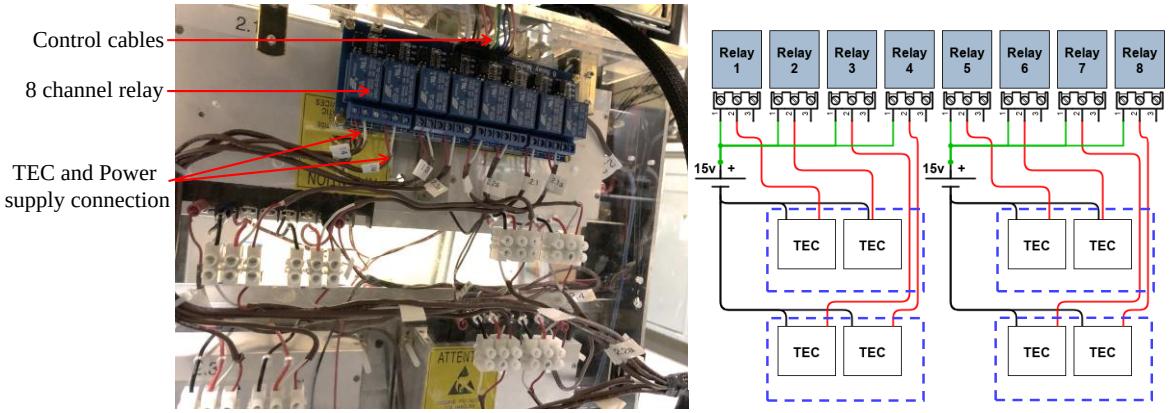

Figure 25: Picture (left) and diagram (right) of the TEC operation circuit used for Group-1 in the multi-wavelength PMI system. The blue dashed squares represent the position of the laser diodes.

4.1.2.3 Heatsinks and Fans

For an effective cooling management, the heat released from the copper plates or the laser diodes using the TEC units has to be dissipated properly. Therefore, the hot surface of the TEC units is mounted on top of an aluminum heatsink having three fans to circulate the air by blowing the heat away from the laser diodes. Three heatsink groups with total of nine fan units are used in the multi-wavelength PMI system. The main purpose of the fans is to accelerate the dissipation of the heat transferred from the TEC units. Thus, they are simultaneously switched on when the TEC units are operational. In order to automate this process, we implemented a switch circuit based on an NPN transistor that controlled via our implemented software. A visual sign of operation is implemented using an LED connected in parallel with each fans group. A picture and a schematic diagram of the fan operation circuit that is used in the multi-wavelength PMI system is shown in Figure 26.

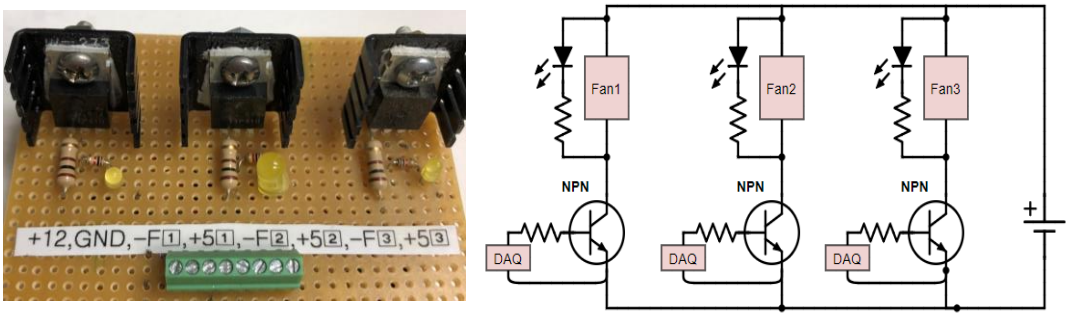

Figure 26: Picture (left) and diagram (right) of the fan operation circuit used in the multi-wavelength PMI system.

This circuit shows that there are three transistors, each transistor is used to operate one group of fans and the corresponding LED. The transistor is switched on when the enable signal is sent by the DAQ device. In this case, the group of fans as well as the connected LED will start to operate. The voltage sources in this circuit are the DAQ that is connected to each transistor and a

12-volt power supply. A resistor connected in series with each LED is used to reduce the current flowing through the LED. Another resistor is used to limit the amount of current flow into each transistor.

4.2 Multi-wavelength PMI control software

The different components of the multi-wavelength PMI system are controlled through a customized control panel created using LabVIEW software (National Instruments, Austin, TX). The control panel has been implemented to communicate with the hardware through National Instruments Data Acquisition devices (NI DAQ). This control panel enables automation of several operations such as: the control of lasers operation, TEC units and fans, as well as monitoring the laser's current and laser's diode temperature. It also allows to adjust the laser's operating current as well as managing the alarms. Therefore, the system was equipped with DAQ devices with both analog and digital input/output channels. The analog input channels are used to read the voltage signal across the thermistor in order to monitor laser diode temperature. They are also used to monitor the laser output current by reading the input signal voltage. On the other hand, analog output channels are required to adjust the laser current by sending a specific voltage corresponding to the desired power to be used during the experiment. In addition, digital output channels are needed as ON/OFF switches to control the operation of the lasers, TEC units and fans. Moreover, digital input channels are used to obtain the digital signal received from the established alarms. To accommodate all of these tasks, four data acquisition units were used: two DAQ cards (PCI-6023E and PCI-6703) and two DAQ USB-6008 external devices.

The PCI-6023E card provides 16 analog input (AI) channels and 8 digital input/output (DIO) channels. The PCI-6703 has been chosen since it has 16 analog output (AO) channels capable of outputting voltages ranging from -10.1 to 10.1 volts, and similar to the PCI-6023E card,

it has 8 digital input/output (DIO) channels. Although these PCI cards provide 16 AI, 16 AO, and 16 DIO channels, two USB-6008 devices each has 8 AI, 2 AO, and 12 DIO channels, were also used to operate our five-wavelength system. In total, multi-wavelength PMI system is provided with 32 AI, 20 AO, and 40 DIO.

Each DAQ card is connected to a (CB-68LPR) terminal block connector through a 68-pin cable. The CB-68LPR connector has 68-pin screw terminals that allows easy connection access. Those connectors as well as the two DAQ USB-6008 devices are mounted at the top of the multi-wavelength PMI system cart, which is secured with a hinged top, Figure 27.

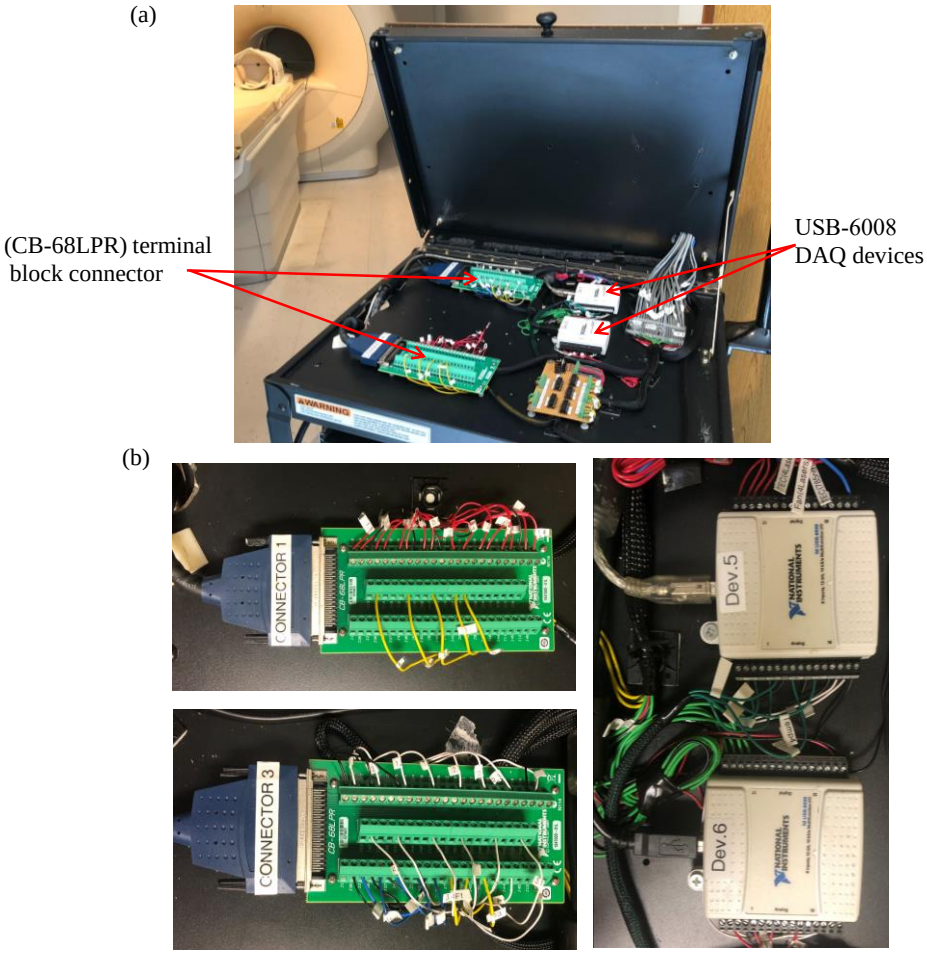

Figure 27: (a) Picture showing the position of the CB-68LPR connectors and the USB-6008 DAQ devices in the multi-wavelength PMI system. (b) A zoomed in pictures of the CB-68LPR connectors and the USB-6008 DAQ devices.

The multi-wavelength PMI control panel has been designed to be user-friendly. The control panel is divided into five windows, one for each wavelength. Figure 28 illustrates the multi-wavelength PMI control panel.

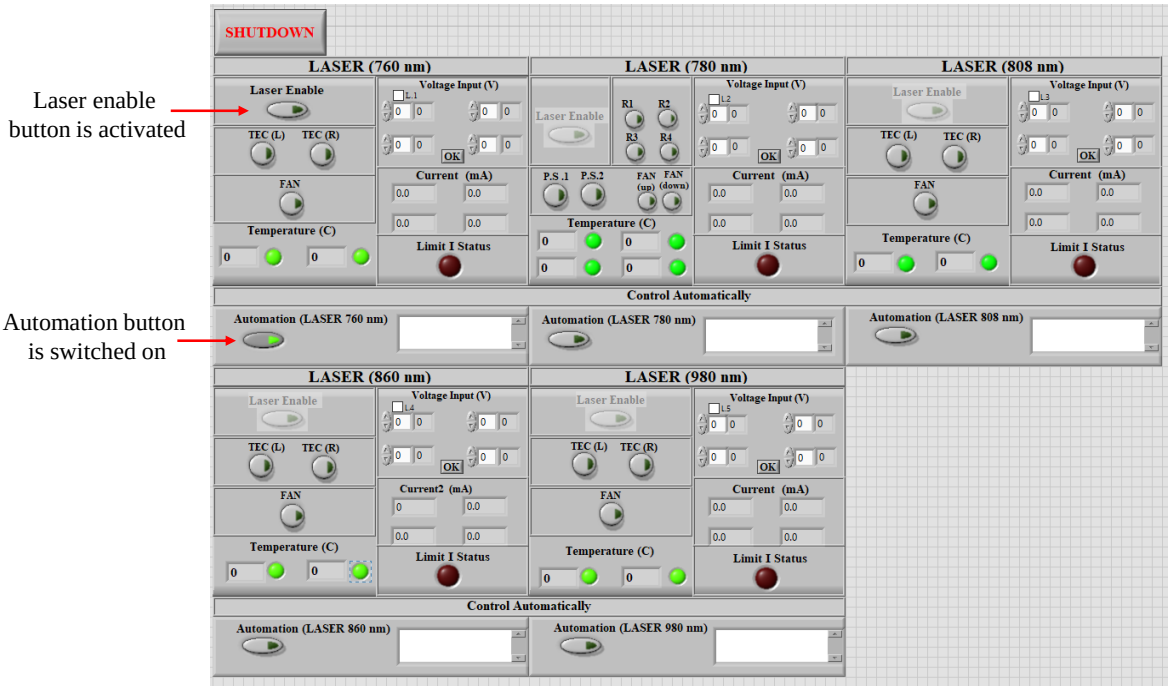

Figure 28: The multi-wavelength PMI control panel.

The process of controlling the multi-wavelength PMI system using this software starts by initializing each laser using its dedicated automation button. During the laser initialization process, the temperature of the laser diode is adjusted based on the operating temperature provided by the laser manufacturer, in a temperature management step. The laser initialization process is illustrated in Figure 29 (a) (red block), and the temperature management step is presented in Figure 29 (b). In this step, the laser diode temperature measured by the thermistor is continuously monitored. If the temperature is higher than the laser safe operating temperature, the TEC units as well as the fans are turned on to cool it down. Once the safe temperature range is reached, the TEC units and

fans are turned off and the laser enable button is activated indicating that the laser can be safely used as shown in Figure 28 (760 nm laser control panel).

When the initialization process is completed, the automation button can be turned off to activate the manual mode, where the TEC units and fans are controlled manually using the control panel and based on the thermistor feedback, Figure 29 (a) (blue block). Otherwise, the temperature is managed automatically, Figure 29 (a) (green block). In the automation mode, the real-time temperature is iteratively monitored to turn on the cooling system automatically when needed. The laser workflow and the temperature management process are presented in Figure 29.

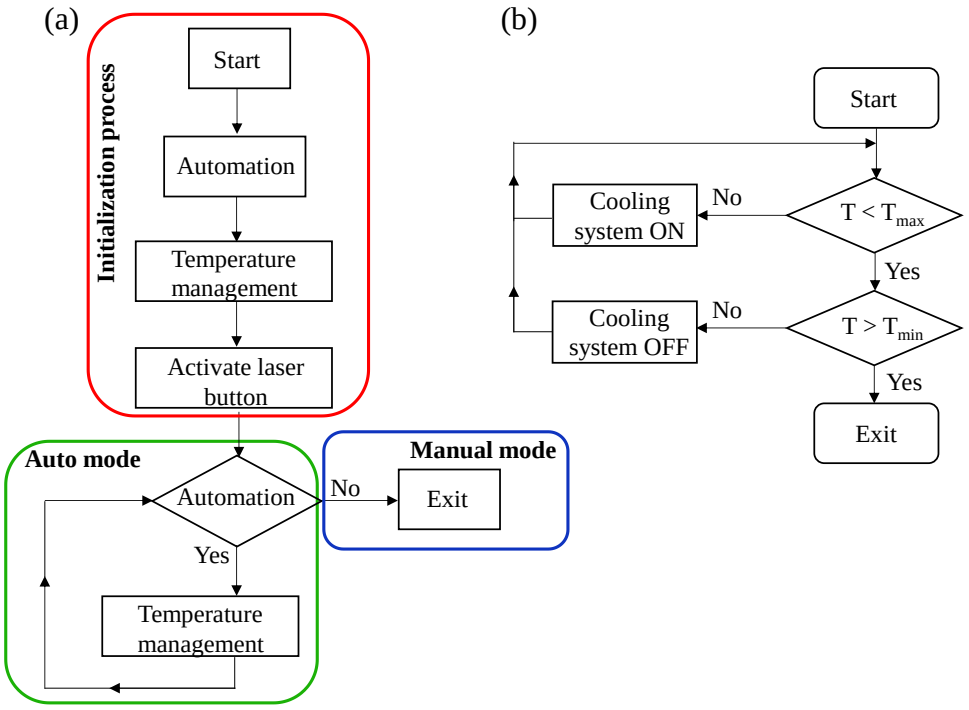

Figure 29: Laser workflow (a) and temperature management process (b) used in the multi-wavelength PMI software.

Once initialized, the laser can be turned on using the activated laser enable button that sends a signal to the manual override circuit, described in section 4.1.1.2, allowing the laser operation. Next, the user can send a specific current to each laser diode to operate at a particular power level, based on the experiment requirements. As part of our safety measures, a checkbox

has to be checked first, which will prompt a dialog window through which the user needs to confirm utilizing this specific wavelength. For each wavelength, four indicators were used to monitor the four laser diodes' output current. This output current is not directly accessed, but it is calculated based on a transfer function provided by the manufacturer. Indeed, since the DAQ devices send and receive voltage only, the transfer function corelates the voltage and the output current is used.

Furthermore, visual alarms have been implemented using LEDs to the control panel to not only ensure the safety of the patients, but the equipment during the experiment as well. For example, while operating in manual mode, an LED indicator was programed to alert the user about the temperature exceeding the safe operating temperature range. In addition, a status red LED is turned on when the laser operating current reaches the used defined laser current limit, namely Limit I Status. In fact, as mentioned in section 4.1.1.2, the laser diode drivers are equipped with a physical Status LED to indicate that the laser has been switched OFF after reaching the laser current limit. Despite this feature, our virtual LED indicator was also implemented in the front panel offering a more accessible notification. A single LED indicator was used to monitor the status of all four lasers of a given wavelength.

For this, instead of using a single digital input channel for each laser driver, an AND gate was used for each wavelength to combine the feedback of the 4 laser diode drivers. Thus, single digital alarm signal is received if at least one laser diode driver reaches the maximum current, resulting in turning on the LED indicator. Moreover, using this scheme was useful in reducing the number of the used digital input channels from 16 to 5 channels, Figure 30.

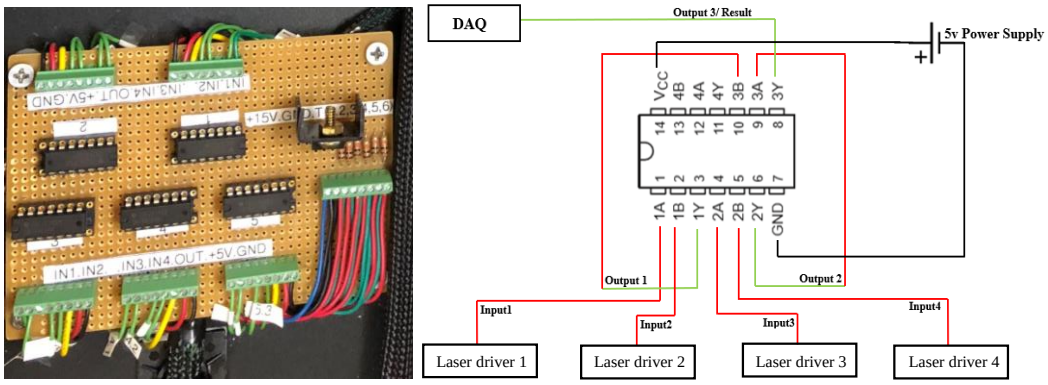

Figure 30: Picture (left) and diagram (right) of the limit current status circuit showing the five AND gates corresponding to the five wavelengths, and representative cable connection.

Lastly, a shutdown button that connects with all the functionalities was implemented in our software. In case of emergency, the user can turn off the operational functions all at once using this button.

4.3 Multi-wavelength PMI system testing

A comprehensive characterization of the multi-wavelength PMI system, including both instrumentation and software, was performed to ensure the optimal performance.

4.3.1 Laser output wavelength measurement

The lasers emission wavelengths were characterized by measuring each laser spectrum using a spectral analyzer (BRC711E PDA, B&W Tek, Inc.). Here, the laser spectral width and the central wavelength of each laser were investigated. Figure 31 shows the spectra of one representative laser from the four laser diodes (760, 808, 860, and 980 nm). Note that the following studies were performed before adding laser 780 nm. As expected, this figure shows that these spectra are narrow and in a Gaussian shape. The peak emission or the central wavelength for each spectrum was found at 757.3, 804.1, 854.5, and 970 nm, respectively. Nevertheless, this shift in the wavelength is within the central wavelength tolerance of each laser diode, as defined by its

specification. The other parameter to characterize the wavelength spectrum is the spectral width which determines the bandwidth that the laser diode produces. Laser spectral width is specified by the full width at half maximum (FWHM) parameter. The spectral widths at FWHM for these laser diodes are 3.4, 3.3, 3.4, 3.8 nm, respectively.

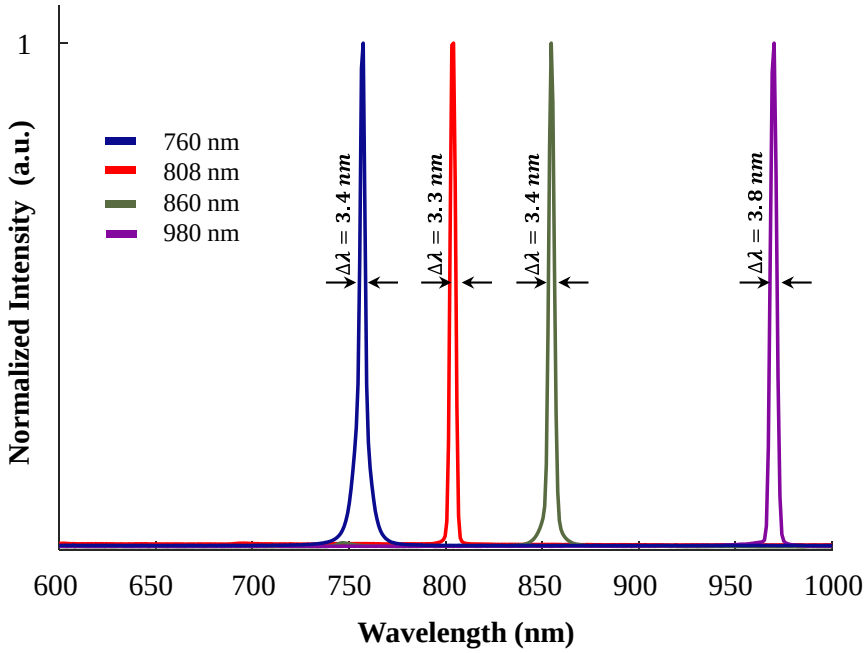

Figure 31: Normalized measured emission spectra of four laser diodes, one for each wavelength, 760 nm (blue), 808 nm (red), 860 nm (green), and 980 nm (purple). The spectral width (Δλ) at FWHM is presented in (nm) for each wavelength spectrum.

4.3.2 Laser output power measurement

Although being part of the laser diode specification, the output laser power as a function of current for each laser diode driver is investigated after completing the electrical connection of the PMI system.

For these measurements, the operating current was controlled and adjusted through the PMI software program while the corresponding optical power was measured using a thermal power meter device (PM10-10, Thorlabs Inc.). The measurements were performed with a 0.5 A current

step and up to the limit current for all laser diodes. Figure 32 shows the output power as a function of current for one laser diode of each wavelength.

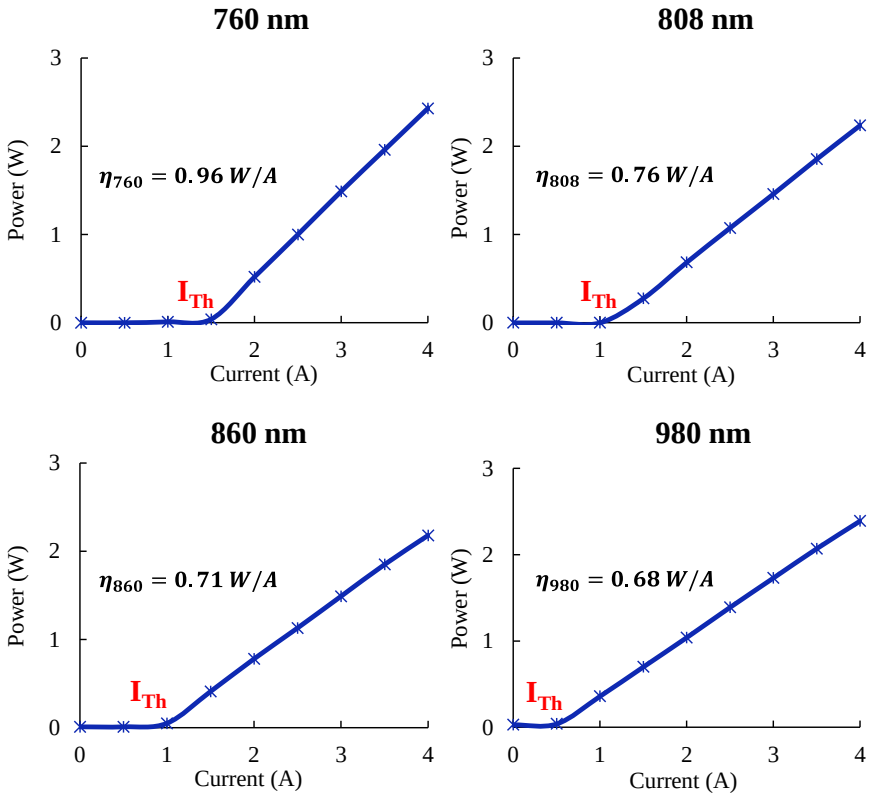

Figure 32: The output power as a function of current graphs for one laser diode of each wavelength (760, 808, 860, 980 nm). The slope efficiency and the threshold current are presented for these laser diodes.

From these results, the threshold current as well as the slope efficiency were identified for each diode. The threshold current corresponding the minimum current value before the lasing begins. The threshold current values are 1.5 A for the first three wavelengths and 1 A for laser 980 nm.

The linear correlation between the output laser power and the operating current, above the threshold current, was used as a conversion function relating the operating current to the laser power level. This conversion function allows the user to specify the current corresponding to the required power level.

4.3.3 Repeatability

The output power repeatability is defined as the variation in the measured power value every time the laser is switched on under the same conditions. For each laser diode, the output laser power at current corresponding to 0.5 W were obtained multiple times to verify its repeatability. The variation was then calculated for each laser diode. Table 5 presents the repeatability error for one laser diode from each wavelength.

Table 5: The calculated repeatability variation in the power measurements at each wavelength.

Wavelength (nm)	760	808	860	980
Repeatability %	0.55	0.38	0.26	0.22

4.3.4 Power stability measurement

The performance of the PMI system on providing a stable output power values over time, is also an important factor since it directly affects the accuracy of PMI results.

The power stability measurements were performed using a photodiode. The current generated from the photodiode is proportional to the laser output power. In order to read and record the photodiode current by a USB DAQ device, a transimpedance amplifier was used to convert the photodiode generated current to a voltage. For each laser diode, the output power was set, using the LabVIEW program, to 1 W and the measurements were acquired for one minute. Although stability studies are often performed over long periods, our testing was limited to one minute since PMI measurements are usually acquired in several seconds only. Figure 33 shows the normalized voltage measurements for one laser diode from each wavelength.

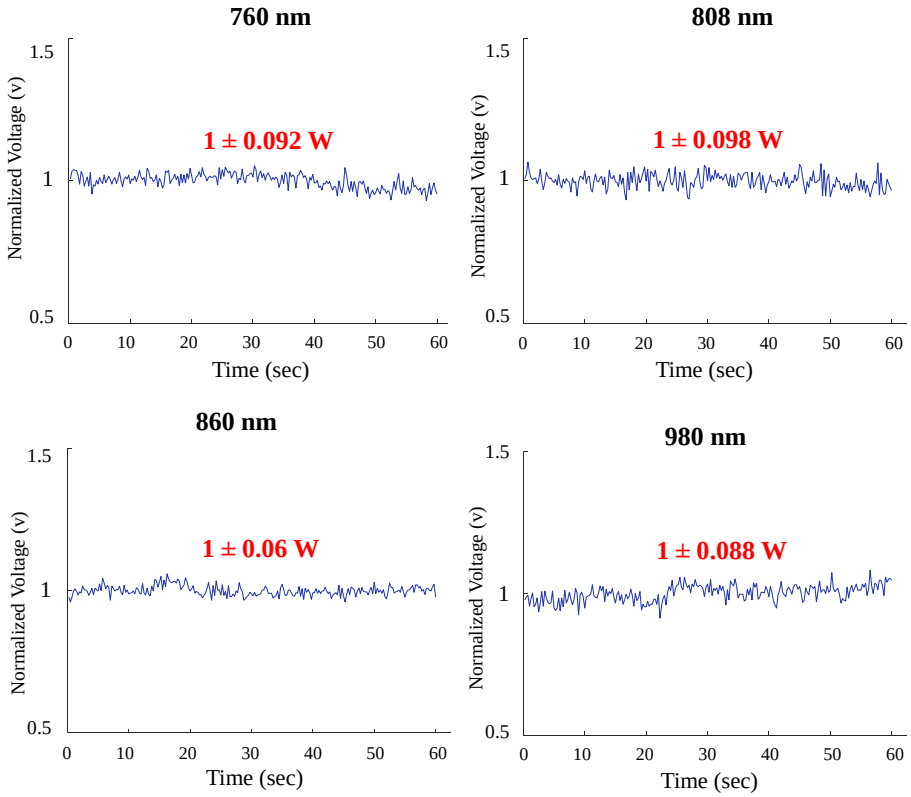

Figure 33: The power stability measurements of one laser diode of each wavelength (760, 808, 860, 980 nm).

For these measurements, the sample rate of the DAQ card and the number of samples were chosen as 100 sample/sec and 100 samples, respectively. Figure 33 shows that the laser output power is stable even right after turning the lasers on, which allowed for the PMI data acquisition to be synchronized with the laser operation. The calculated power deviations are ranging between 6% and 10% of the total output power (1 W) over the one-minute testing period. It is important to note that the power stability measurements were performed while the temperature management system is running to ensure the consistency in the laser diodes operating temperature.

Table 6 summarizes the power stability values for the laser diodes presented in Figure 33.

Table 6: The calculated power stability (%) values at each wavelength.

Wavelength (nm)	760	808	860	980
Power stability %	9.2	9.8	6	8.8

A simulation study has been performed to investigate the effect of the laser power variation on the recovered absorption coefficient. This study showed that the maximum power variation of ~ 10% only resulted in ~3% of the recovered absorption distribution percentage error.

4.4 Laser irradiance

The high-power lasers utilized by PMI are classified as Class 4 lasers based on the American National Standards Institute (ANSI) Z136.1-2000 Standard. In order to avoid any skin injures when performing PMI *in vivo* for human imaging, the laser irradiance has to be governed by the maximum permissible exposure (MPE) limit for skin as delineated by ANSI Standard. MPE for skin is the maximum laser irradiance (W/cm^2) that the person can be exposed to without causing any hazardous biological changes in the skin. MPE depends on the laser power, wavelength, laser spot size on the skin, and the exposure time. When utilizing NIR laser for a period of 10 sec or more, the MPE is calculated as follow:

$$MPE = 0.2\,(10^{2(\lambda-0.700)}) \tag{44}$$

here, the wavelength λ is expressed in micrometer.

Table 7 summarizes the MPE values calculated at the five wavelengths that are used in the multi-wavelength PMI system.

Table 7: The MPE value at each of the wavelength used in PMI system.

Wavelength (nm)	760	780	808	860	980
MPE (mW/cm^2)	264	289	329	418	726

Thus, for *in vivo* imaging, the power at each wavelength should be adjusted based on the calculated MPE values and the laser spot size to allow the irradiance to be smaller or equal to the MPE values listed in Table 7.

4.5 PMI data acquisition

4.5.1 Magnetic Resonance Thermometry (MRT)

Different approaches are available to monitor and measure the generated temperature in biological tissue while performing photothermal therapies. For example, a simple thermometers were widely used due to their low cost and easy integration [117, 118]. However, thermometers are limited to providing only point measurements. In addition, the measured values are suffered from inaccuracy due to the interaction with light sources. Another simple approach would be the infrared thermography. However, it can only acquire surface temperature measurements [119, 120].

In PMI, acquiring the laser-induced temperature measurement from the whole volume of the imaged medium, not only its surface, is required. MRI thermometry is ideal for noninvasively mapping internal temperature distribution [121, 122]. Therefore, MRT was utilized to perform PMI measurements. The studies presented in this thesis were all performed using a 3 Tesla MRI scanner (Achieva; Philips) located at our imaging center, Center for Functional Onco-Imaging at UCI.

There are several MRT methods that work based on the temperature-dependent MR parameters which can be used as temperature indicators. These methods are divided into two main groups based on the nature of their measurements. Some measure the change in temperature such as proton resonance frequency, T1 and T2 based methods, as well as diffusion method. The other methods measure the absolute temperature such as spectroscopic approaches and methods utilizing thermosensitive contrast agents [96, 123].

4.5.1.1 Proton Resonance Frequency (PRF) shift method

The PRF shift method is the most used method due to its high spatio-temporal resolution, sensitivity, tissue-type independence, fast data acquisition, as well as its excellent linear correlation with temperature over a large temperature range [96, 124]. Therefore, this method was chosen to study the laser-induced temperature on PMI technique.

The PRF shift method principle is based on the fact that the PRF in water molecule is dependent on the local magnetic field, which describes the magnetic field experienced by the protons. When temperature increases, the local magnetic field reduces due to the increase of the electron shielding around the Hydrogen proton, which consequently decreases the PRF. The change in the PRF due to temperature is observed in the phase of the MRI images which can be measured using a gradient echo sequence. Temperature variations maps are proportional to the phase variations maps and can be calculated using Larmor equation as follow [123]:

$$\Delta T = \frac{\psi(t) - \psi(t_0)}{\gamma \alpha B_0 T_E} \tag{45}$$

where $\psi(t)$ is the measured phase at time t, $\psi(t_0)$ is the baseline phase measured at a known temperature at time t_0, γ is the gyromagnetic ratio, α is the PRF coefficient, B_0 is the main magnetic field, and T_E is the MRT echo time. This equation shows that the phase variation $\Delta\psi$ is dependent on the applied echo time. Increasing the echo time would provide high precision in the phase variation measurements.

Since the relative temperature change is linearly proportional to the measured phase variation, dynamic phase maps are acquired during the PMI experiment. Figure 34 displays PMI data acquisition timeline showing the laser status and the change in temperature of the imaged medium.

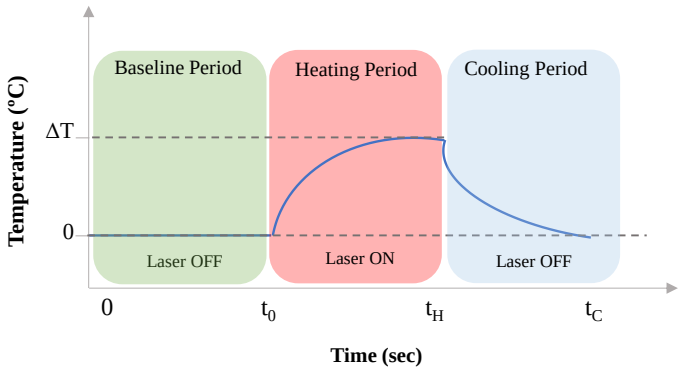

Figure 34: PMI data acquisition timeline. The times t_0, t_H and t_C are the times needed to acquire all the frames within the baseline, heating and cooling periods, respectively.

First, the baseline phase maps are acquired before the laser operation. Next, the laser is turned on and a series of phase maps are acquired during the heating period. An additional cooling phase maps series will be acquired after turning OFF the laser. Each acquired period consists of multiple frames with a duration defined by the MRT imaging parameters. Multiple baseline phase maps are usually averaged to obtain a baseline map with less noise to improve the signal-to-noise ratio (SNR) of the calculated temperature maps. A preprocessing step is required to unwrap these measured phase maps using the Goldstein branch-cut method [125]. The internal laser-induced temperature maps are then obtained using equation (45). The resulted temperature maps are then used in the PMI image reconstruing algorithm where each pixel in the map is considered as a measurement point.

4.5.2 Radiofrequency (RF) coils

To improve the SNR of the acquired phase measurements and consequently the temperature maps, relatively small RF coil was used. The RF coil works in conjunction with the Quadrature Body coil where the Q-Body works as the RF transmitter and the small RF coil as a receiver. Two RF coils have been used to perform the PMI studies, a customized home-built small

animal RF coil and a commercial Philips RF coil. In this section, the integration of multi-wavelength PMI system with those two RF coils is discussed.

4.5.2.1 Customized RF coil

This coil has been developed to perform small animal PMI imaging. The coil interface consists of the custom-designed RF coil, a small animal holder, and four windows to allow illumination from multiple sides. Figure 35 shows the PMI interface with the customized RF coil. Four long optical fibers (1-mm-diameter, 15-m-long) are used to transport light from the PMI system cart located in the control room to the object located in the RF coil inside the MRI bore. The tips of these fibers were customized to be MR compatible and accommodated by the illumination windows where the output light is collimated using a 32.5 mm diameter aspherical lens (Newport Corporation, Irvine, CA, US).

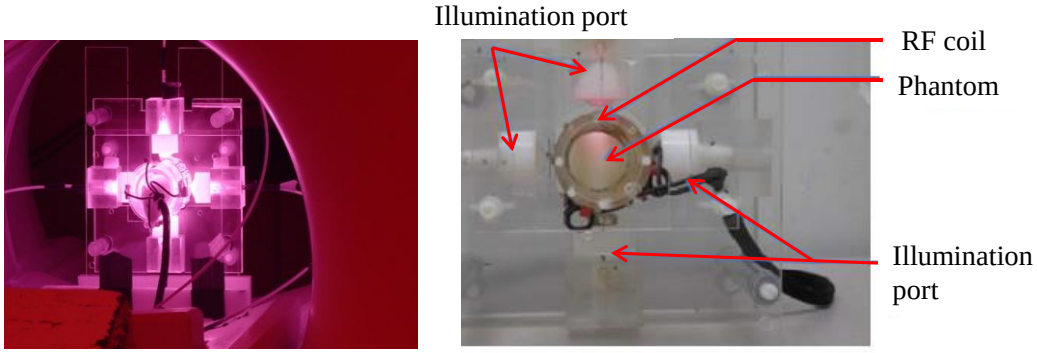

Figure 35: PMI interface during the experiment (left) and a zoomed in picture (right) shows the home-built RF coil with the optical fiber, lens and the phantom to be imaged [50, 126].

4.5.2.2 Commercial RF coil

The Philips SENSE 8-channel wrist coil is usually used to deliver high-resolution upper extremities imaging. This small RF coil has been chosen to perform small animal PMI studies based on its small size that allows the achievement of high SNR images. Few modifications were

necessary for its integration with the multi-wavelength PMI system. For example, the slot on its upper part was used as illumination window since the width of the slot was smaller than the diameter of the laser spot size. Similar to the customized RF coil, the 15-m-long fibers with the lens were used to transport the light from the PMI system to the imaged animal. However, having a single slot limited the number of possible illumination sides to only one. Lastly, a plastic bed was designed to conveniently hold the small animal facilitating the positioning of the imaged subject within the coil, Figure 36.

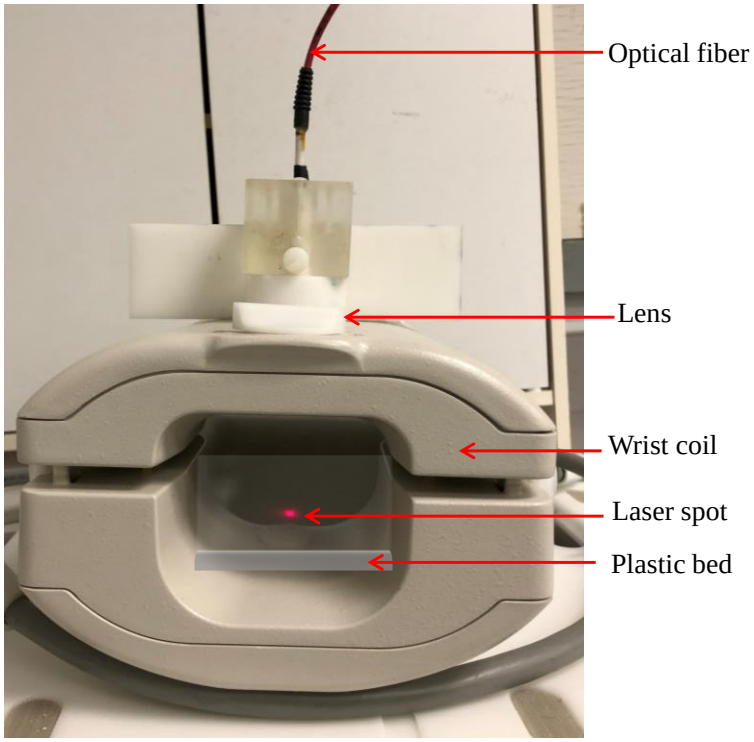

Figure 36: Picture of the Philips SENSE 8-channel wrist coil with the optical fiber, lens and the plastic bed where the object is placed.

Chapter 5: Validation of multi-wavelength PMI with-experimental phantom studies

This chapter presents the experimental studies conducted to test the multi-wavelength PMI system and evaluate its performance in order to validate the feasibility of the multi-wavelength PMI technique.

5.1 Experimental procedure

5.1.1 Phantom preparation

The development of the multi-wavelength PMI system has required the use of tissue-simulating objects to mimic the optical properties of animal or human tissues. These objects are commonly called phantoms, and they are widely used for system testing, characterization and validation. There are different types of tissue-simulating phantoms which can be used for optical imaging systems. They might be either solid, liquid, or gel phantoms. All the experiments performed in this thesis were conducted on the latter type. These phantoms are made by mixing agar powder (HiMedia Laboratories Ltd.) with distilled water. This agar mixture is heated and continuously stirring until the agar powder completely dissolves in water and the solution is clear and transparent. Then, the solution is cooled down while it is continuously stirring. The optical properties of the phantom are set using Intralipid® 20% (Fresenius Kabi Inc.) and black Indian ink dye (Winsor & Newton Ltd.) for scattering and absorption adjustment, respectively. A specific concentration of these components is added to the cooled-down agar solution to achieve the desired optical properties. In addition, the MRI contrast agent, gadolinium- diethylenetriamine penta-acetic acid (Gd-DTPA) (GE Healthcare Co.) is added to the mixture to increase the signal intensity

on T1-weighted image by shortening the relaxation time T1 [127, 128]. The mixture is then poured into a specific mold and cooled in a refrigerator to form the desired phantom shape.

5.1.2 PMI measurements acquisition

All the experiments presented in this thesis were performed on a mice-sized 25-mm-diameter cylindrical phantom, Figure 37 (a). Before conducting the experiment, the temperature of the phantom should be equalized with the MRI ambient temperature which is equal to 20 °C. This initial temperature will be considered as the phantom baseline temperature. During the experiment, the phantom is aligned along the MRI axial direction, and the center of the axial direction of the phantom is aligned with the laser spot center. For calculation simplicity, a single illumination window was used to heat-up the phantom in all the studies performed on this thesis. The phantoms used in this work are either having homogenous optical properties or heterogenous with inclusions embedded close to the upper surface of the phantom. Therefore, the illumination was employed from the top side of the phantom. Figure 37 (b) illustrates a T1-weighted MRI image showing a cross-section of the phantom and the laser source position.

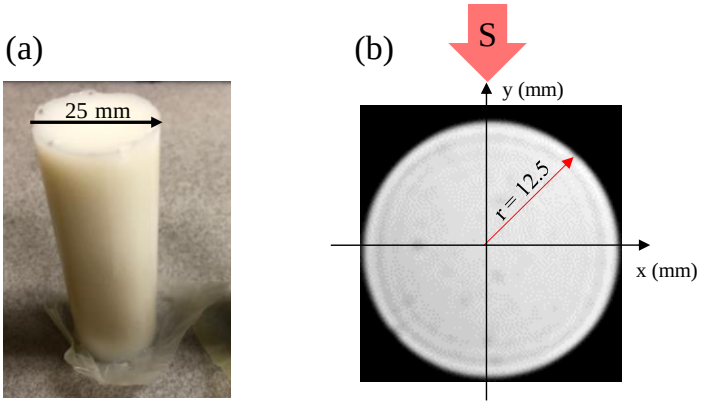

Figure 37: An example of the agar phantom used in the multi-wavelength PMI studies. (a) Photograph of the 25-mm-diameter agar phantom, (b) Axial T1-weighted MR image of the 25-mm-diameter phantom. The laser beam is illustrated using red arrow at the top side of the phantom (S).

All the MRT phase images were acquired with a size of 320 x 320 pixels and pixel size of 0.1875 mm, using a gradient echo sequence with repetition time TR=82 ms, TE= 12 ms, and a flip angle of 22° resulting in a temporal resolution of 6 sec. The internal laser-induced temperature variation maps are then obtained from the phase maps using the Larmor equation. When performing multi-wavelength PMI experiment, the MRT temperature maps are sequentially acquired for each wavelength. A two-minute gap is always used between acquisitions to ensure that the entire heat from the previous wavelength had dissipated, and that the phantom went back to its baseline temperature. When solving the PMI forward problem, the thermal properties of the phantom are set to be the same as water values since it represented approximately 98% of its constituents [129]. The optical properties of each phantom will be introduced in the following sections for each study individually.

5.2 System performance evaluation: preliminary experiments

Integration both systems, the new multi-wavelength PMI system and the measurements device (MRT) is important and needs to be investigated. Therefore, after developing and testing the multi-wavelength PMI system, experimental studies were conducted to evaluate the overall performance. PMI forward problem was solved for each study to compare the experimental results with the simulated ones.

5.2.1 Temperature evolution over time

The variation on the laser-induced temperature with time has been studied on a phantom during the heating and cooling periods. The phantom used in this experiment has homogenous optical properties ($\mu_a = 0.0141\ \text{mm}^{-1}, \mu_s' = 0.89\ \text{mm}^{-1}$). Multiple phase maps were acquired with a total acquisition time of 114 sec which resulted in 19 frames as the temporal resolution was

~ 6 sec. During the experiment, the first three phase maps were acquired before turning the laser on and used as baselines. During the heating period, starting at fourth frame, the 760 nm laser was used to illuminate the phantom from its top side for 42 sec while acquiring seven frames. The laser was then turned off at the end of the tenth frame and nine phase maps were acquired during this cooling period. The temperature maps were then calculated using Equation (45) by subtracting the average of the baseline phase maps from all the phase maps acquired during the heating and cooling periods. Figure 38 shows the experimentally measured temperature maps during the three periods, baselines, heating, and cooling. As expected, no temperature change is observed on the baseline temperature maps. The first map on the heating period shows that the heat energy is initiated from the top side of the phantom since the laser source was positioned at the top. The temperature is then continuously increases with time, due to the absorption of more photons as the phantom was still under the illumination during the heating period. After turning off the laser in the cooling period, the temperature unceasingly decreases with time while it keeps propagating through the medium as the heat diffusion increases with time resulting of blurry temperature maps.

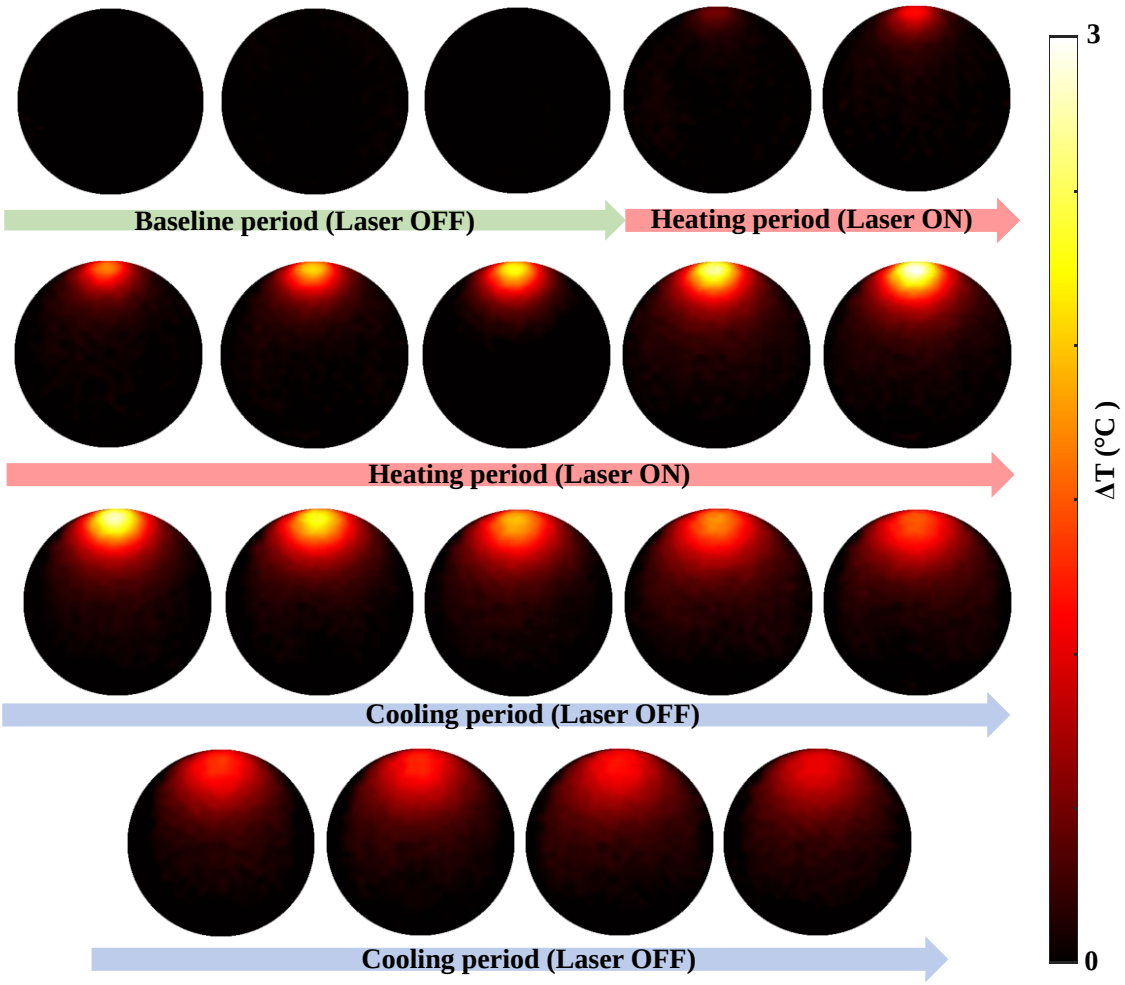

Figure 38: Temperature maps measured experimentally and the corresponding laser status during the baseline (green arrow), heating (red arrow), and cooling periods (blue arrow). These temperature maps are organized in the order of left to right and row by row.

After acquiring the MRT temperature maps, the PMI forward problem was used to replicate this experiment and generate simulated temperature maps on a numerical phantom having the same dimension and optical properties as the experimental phantom. The temperature variations were calculated for a total time of 114 sec with one-second temporal resolution. Since the MRT temporal resolution was limited to ~6 sec, the simulated temperatures obtained within intervals of 6 sec were averaged before being compared to the MRT experimental data. The comparison of the simulated and experimental temperature maps was performed by overlying the temporal temperature

profiles, which were calculated over a 2-mm-diameter region-of-interest (ROI) centered 2.5 mm under the upper surface of the phantom, Figure 39. These profiles show that the experimental temperature maps agree well with the temperature variations modelled via PMI forward problem with an R-squared coefficient of 0.995.

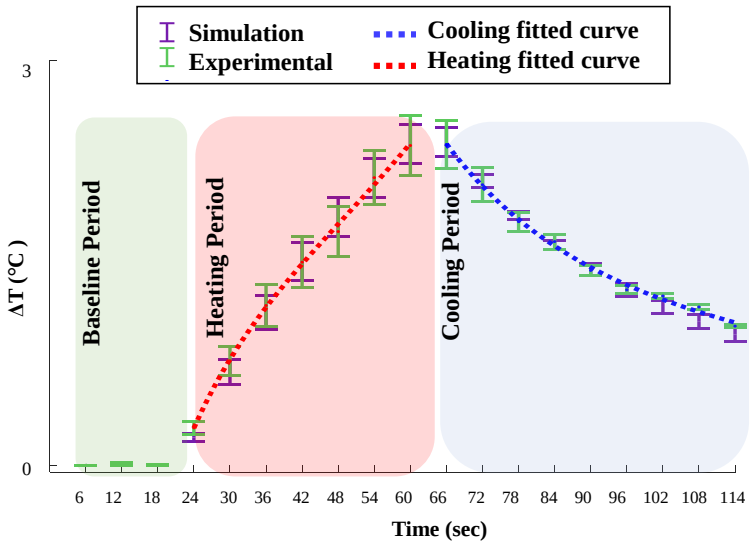

Figure 39: Experimental (purple) and simulated (green) temporal temperature profiles at the ROI during the baseline, heating and cooling periods. The dotted lines show the two-term exponential fit during the heating (red) and cooling (blue) periods.

The change in temperature during the heating and cooling periods were fitted by a two-term exponential function. A two-term exponential growth function was used to fit the heating curve with R-squared correlation coefficient of 0.998, and the temperature change during the cooling period was fitted with a two-term exponential decay function with correlation coefficient of 0.996.

Among these periods, temperature measurements acquired during the heating period are only used for PMI image reconstruction to minimize the heat diffusion effect which decreases the quantitative accuracy and the spatial resolution.

5.2.2 Laser-power effect

In this experiment, the effect of the laser power on the temperature variation and the consequent recovered absorption maps has been studied. This study was performed on a phantom with a 4-mm-diameter cylindrical inclusion embedded 4.5 mm under the upper surface of the phantom. The inclusion has a three times higher absorption coefficient compared to the background. The absorption and scattering of the background were set to 0.0141 mm^{-1} and 0.89 mm^{-1}, respectively. One laser wavelength, λ=760 nm, was utilized to illuminate the phantom from its top side. First, the PMI temperature measurements were acquired by illuminating the phantom with laser power of 1 W. Then the experiment is repeated by doubling the laser power. Between these two experiments, the phantom was left to cool down until it went back to its baseline temperature. Figure 40 shows the measured temperature maps after heating the phantom for 18 seconds utilizing one- and two- watt laser power, (a) and (b) respectively. These temperature maps show a high increase in temperature under the illumination area as well as in the inclusion due to its higher absorption with respect to the background. The maximum increase in temperature was around 0.88 °C and 1.8 °C when using the 1 W and 2 W power, respectively.

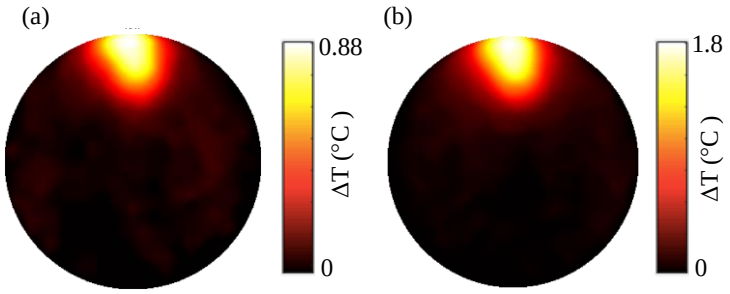

Figure 40: The measured temperature maps after heating the phantom for 18 seconds from its top side utilizing a laser power of (a) 1 W, and (b) 2 W.

For each laser power level, the temperature map was used in the image reconstruction algorithm to recover the corresponding absorption coefficient map. During the reconstruction, same parameters were used for the two cases except for the laser power level which was taken into consideration when the simulated temperature maps were generated. Figure 41 shows the recovered absorption maps where the absorption coefficient value was recovered with an average error of 10% and 9% for the one- and two-watt cases, respectively. These maps show that the absorption coefficient was accurately recovered even for the one-watt case which results of less temperature to noise measurement, Figure 40 (a). In fact, PMI can recover the absorption accurately as long as the increase in temperature exceeds the MRT noise level which is found to be 0.1 °C in our system.

Thus, by increasing the power of the utilized laser, the generated heat in the medium increases as well as the penetration depth. However, the recovered absorption remains constant as it depends on the concentration of the medium and the wavelength of the applied laser.

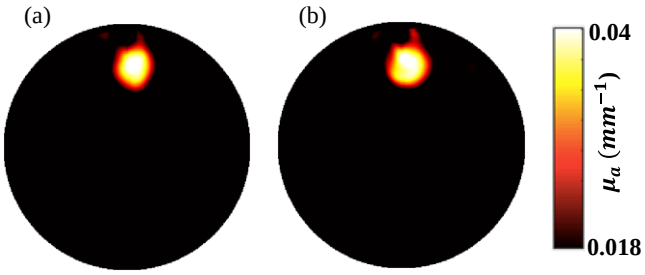

Figure 41: The recovered absorption maps when utilizing 760 nm laser with (a) low power level and (b) high power laser level.

5.2.3 Laser-wavelength effect

One of the parameters that affect the increase in temperature, is the optical absorption coefficient of the medium which is wavelength dependent. Multiple wavelengths were applied during this experiment to study the potential correlation between the temperature variations and

the wavelength-dependent absorption coefficient. One phantom with homogenous optical properties was used for this study. The optical absorption coefficient of this phantom was set using a black ink dye as well as a NIR dye (NIR869A, QCR solution Corp, USA) having a peak at 869 nm. This NIR dye was added to induce a noticeable wavelength-dependence. The normalized total absorption coefficient spectrum of the phantom in the NIR range is presented in Figure 42. The total absorption coefficient spectrum represents the sum of absorptions of the phantom constituents (water, intralipid, as well as the absorbent dye). The distinct spectrum of each constituent will be later presented in the following sections. The absorption spectra of water, fat, and black ink dye are presented in section 5.3 Figure 44.b, while the spectrum of the NIR869A dye is shown in section 5.4 Figure 49.b.

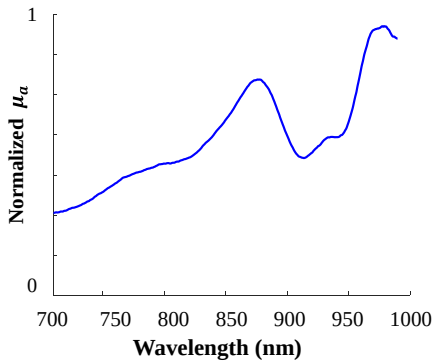

Figure 42: Normalized absorption coefficient spectrum of Phantom 1 (red) and Phantom 2 (blue) in the NIR spectral window.

To study the temperature change with the used laser wavelengths, the temperature maps were acquired for each wavelength successively, Figure 43 (first row). These temperature maps show that the increase in temperature matches the phantom absorption coefficient spectrum, Figure 42.

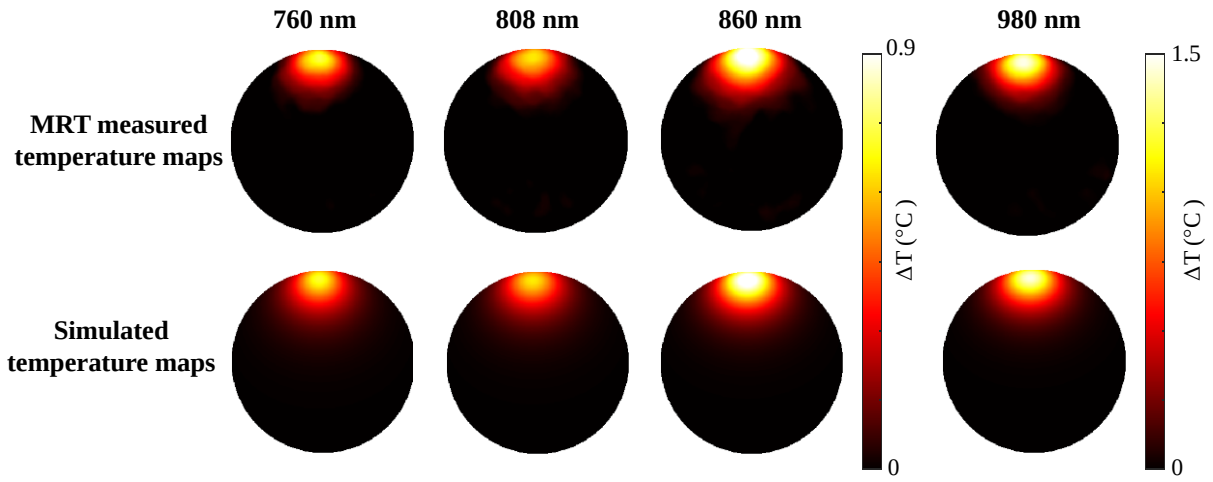

Figure 43: The MRT measured (first row) and the simulated (second row) temperature maps at 760 nm, 808 nm, 860 nm, and 980 nm.

The maximum increase in temperature was ~1.5 °C, which was measured at laser wavelength 980 nm since the phantom has the highest absorption at this wavelength. A higher increase in temperature was observed at 860 nm compared to the first two wavelengths, since the NIR dye has a peak around this wavelength. The increase in temperature at 860 nm reached 0.9 °C while it was ~ 0.7 °C for the first two wavelengths.

PMI forward problem has been solved at each wavelength to model the spatial and temporal temperature distribution using the real absorption coefficient at the utilized wavelength, as shown in Figure 43 (second row). The experimental temperature maps measured using MRT show good agreement with the simulated temperature maps with average R-squared correlation coefficient of 0.971.

5.3 Feasibility phantom study: proof of concept

As a first PMI concentration recovery study, a simple agar tissue-simulating phantom with homogenous optical properties was used to recover the concentration of its constituents utilizing multi-wavelength PMI [66].

5.3.1 Experimental setting

In this proof-of-concept study, the optical properties of the used phantom were chosen to be homogenous. The total absorption coefficient of the phantom consists in the sum of absorptions of its main chromophores (water, intralipid, and a black ink dye). Figure 44 (a) shows the total absorption coefficient spectrum of the phantom (dashed line) as well as the spectrum of each chromophore, water (green), fat (red) and the ink dye (blue). The absorption spectra of both water and fat were obtained from literature [111, 112]. While the optical absorption spectrum of the ink dye was experimentally measured using a spectrometer (USB 2000+, Ocean Optics, Inc.).

The reduced scattering coefficient of the phantom was adjusted using intralipids and set to be equal to 0.89 mm^{-1} at 760 nm and validated using our frequency-domain Diffuse Optical Tomography (DOT) system [130]. The values for the other wavelengths were calculated using the Mie theory approximation [131]. The reduced scattering coefficient spectrum of the phantom in the NIR range is shown in Figure 44 (b).

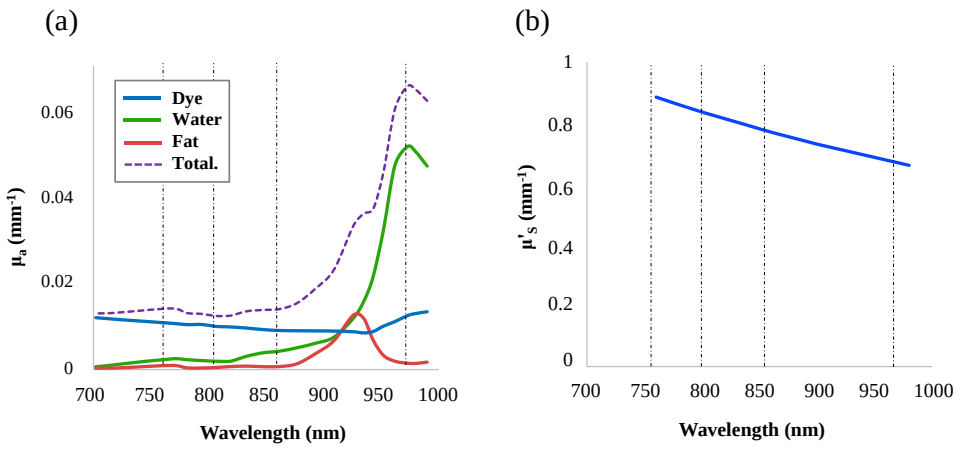

Figure 44: Description of the agar phantom used for the multi-wavelength PMI chromophore recovery proof of concept study: (a) Total absorption spectrum of the phantom (dashed line), as well as the individual spectra of its chromophores: water (green), fat (red) and the ink dye (blue) in the NIR spectral range. The vertical dot-dashed lines represent the PMI laser wavelengths used in the study [66]. (b) The reduced scattering coefficient spectrum of the phantom in the NIR range.

Four laser wavelengths (760 nm, 808 nm, 860 nm, 980 nm) of the multi-wavelength PMI system were employed to illuminate the phantom in this study. The phantom optical properties at these wavelengths were calculated from the spectra in Figure 44 and summarized in Table 8.

Table 8: Real optical absorption and reduced scattering of the agar phantom used for the multi-wavelength PMI chromophore recovery proof of concept study [66].

	Real optical properties			
	760 nm	**808 nm**	**860 nm**	**980 nm**
μ_a **(mm^{-1})**	0.0141	0.0124	0.014	0.0645
μ_s' **(mm^{-1})**	0.89	0.84	0.77	0.66

5.3.2 MRT temperature measurements at multiple wavelengths

In this study, the second MRT frame provided the temperature map corresponding to a 12 sec heating period was used, Figure 45. Since the phantom was only illuminated from its top side, a higher increase in temperature below the illumination site was induced. The increase of temperature depends on several parameters such as the applied laser power, exposure time and optical properties of the phantom. In this study, the applied power and the exposure time were set to be equal for all wavelengths; therefore, any difference in the temperature increase would be due to a variation in the optical absorption coefficient of the phantom. At the first three wavelengths (760 nm, 808 nm, and 860 nm), a comparable temperature increase was observed with a peak increase of 1.33 °C. This similarity in the temperature variation is indicative of having a relatively similar absorption coefficient at these wavelengths. However, a higher increase in temperature was observed at 980 nm. This high temperature increase at this wavelength is mainly due to the absorption of water, which has its absorption peak at 980 nm [112].

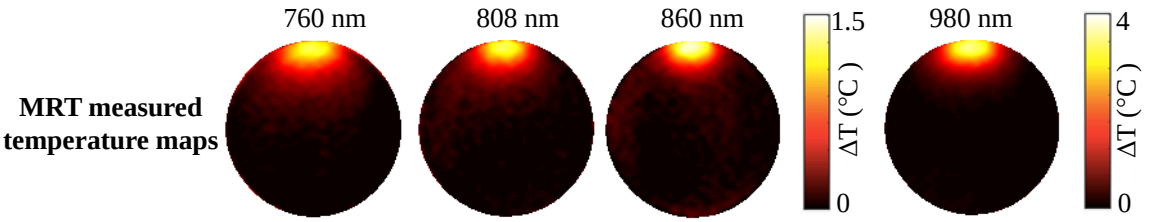

Figure 45: The MRT measured temperature maps after a 12 sec heating period [66].

5.3.3 Reconstruction of the absorption coefficient at multiple wavelengths

PMI was used to retrieve the phantom optical absorption coefficient at each wavelength from the MRT measured temperature maps. PMI recovered a homogeneous absorption map at each wavelength. The mean and standard deviation of the recovered absorption coefficient values are summarized in Table 9. The recovered absorption values demonstrate the ability of PMI to accurately recover the optical absorption of the phantom with an average error as low as ~ 1.9%.

Table 9: Mean, standard deviation, and the percentage error of the recovered absorption coefficient of the phantom at all four wavelengths [66].

	Recovered absorption			
	760 nm	**808 nm**	**860 nm**	**980 nm**
μ_a (mm^{-1})	0.0144 ± 0.0011	0.0128 ± 0.0011	0.0142 ± 0.0008	0.065 ± 0.0028
Percentage error (%)	2.1	3.2	1.4	0.8

As expected from the MRT temperature maps, Table 9 shows that the recovered absorption coefficients are relatively similar at the first three wavelengths (760 nm, 808 nm, and 860 nm) while it is approximately 5 times higher at 980 nm.

In order to validate our results, the recovered absorption coefficients (Table 9) were used in the PMI forward problem solver to generate the corresponding simulated temperature maps. The forward temporal resolution is 1 sec while it is 6 sec for the MRT. Therefore, the generated simulated temperature maps were first averaged over time periods corresponding to the MRT

duration frames before being compared to MRT experimental data. The simulated temperature map corresponding to the mean of the temperatures between 7-12 sec heating period (2nd MRT frame) at each wavelength is presented in Figure 46. These simulated temperature maps show similar temperature variations as the ones observed on the measured MRT maps.

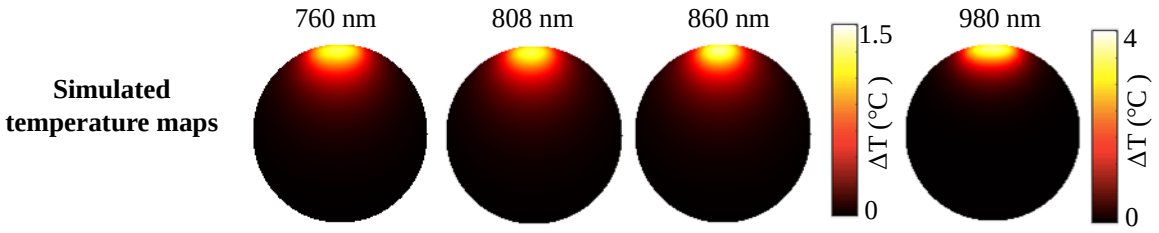

Figure 46: The simulated temperature maps obtained using the absorption coefficient recovered at each wavelength using the MRT maps presented in Figure 45 [66].

A performance validation of the PMI technique was achieved by comparing the temperature in the experimental and simulated data. Figure 47 presents a profile carried-out along the y-axis of the MRT temperature maps (red) and the simulated ones (blue) at each wavelength. The blue highlighted region illustrates the noise level of our MRT measurements which is equal to 0.1 °C. These results confirmed that the measured MRT temperature profiles are in a good agreement with the simulated ones with R-squared correlation as good as 0.992 in average for all wavelengths.

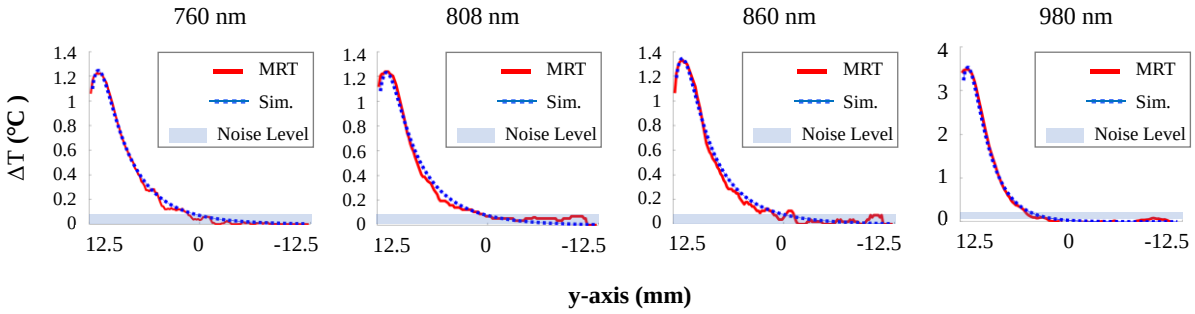

Figure 47: Temperature profiles carried out along the y-axis of the induced temperature maps: measured MRT (red) and simulated temperatures (blue) [66].

Although the highest change in temperature was observed at 980 nm around the source position, the change in temperature decreases faster with depth at this wavelength. Indeed, the high absorption coefficient at this wavelength causes less photon penetration. The temperature reached the MRT sensitivity at 3.9 mm above the center of the phantom, while it was ranging between 1.4 and 0.89 mm above the center for the other laser wavelengths.

5.3.4 Recovering the chromophore concentration

The recovered optical absorption at the used four wavelengths was then utilized in a least-squared minimization process based on the modified Beer-Lambert Law to retrieve the concentration of the main chromophores of the phantom. The contribution of the absorption of the fat was neglected since their maximum absorption at the used wavelengths represent less than 2.2% of the total absorption of the phantom. The concentration maps were recovered accurately for both water and the ink dye, Table 10. Due to the water abundance, its concentration was recovered with an average error of only 0.4%.

Table 10: Real and recovered concentration of the main chromophores, namely water and the used ink dye and their percentage error [66].

	Concentration		
	Real (%)	**Recovered (%)**	**Percentage Error %**
Dye	0.35	0.39 ± 0.0465	11.4
Water	98	98.38 ± 1.5979	0.4

The recovered concentration values of the main chromophores were used then to calculate the total absorption spectrum of the phantom in the NIR window. Figure 48 shows the calculated total absorption of the phantom in the NIR spectral range. This total absorption spectrum was obtained by performing a limited set of measurements at four wavelengths only.

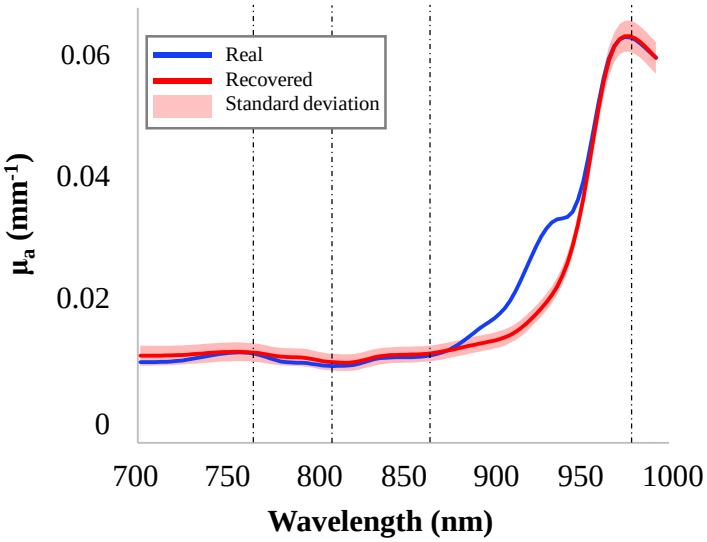

Figure 48: Total absorption spectrum of the phantom in the NIR spectral range: real (blue) and calculated (red). The highlighted red area represents the standard deviation of the recovered absorption, and the vertical dot-dashed lines represent the four wavelengths used in the study [66].

The recovered total absorption spectrum (red) is in a good agreement with the real one (blue) with an average error of ~ 2.3%, except in the spectral region around 930 nm. This spectral region corresponds to the peak absorption of fat, which were neglected during the concentration calculations. This error clearly shows that a laser wavelength is required for each specific chromophore based on its peak absorption. Therefore, our system was designed to host additional lasers. For example, wavelength 930 nm will be added to be able to recover the concentration of fat.

In summary, multi-wavelength PMI demonstrated a great ability to assess the concentration of the different chromophores, thus providing the total absorption of the phantom at any wavelength within the NIR spectral range using only limited set of measurement performed at accurately chosen wavelengths.

5.4 Phantom bearing inclusions study

Multi-wavelength PMI has shown a good performance on recovering the concentration of chromophores distributed homogenously throughout a mice-sized phantom. As a next step, a heterogeneous phantom bearing inclusions with different optical properties has been used to mimic the presence of tumors inside a healthy tissue [67]. This step is essential to pave the road for the *in vivo* application of multi-wavelength PMI for tumor detection and characterization.

5.4.1 Experimental setting

The phantom used in this study has two embedded 4-mm-diameter inclusions, Figure 49 (a). The absorption coefficient of these inclusions is set to be higher than the background to simulate an absorption contrast due to the presence of a cancerous tumor [132]. Inclusion 1 and Inclusion 2 are respectively positioned at 7.3 mm and 5.2 mm above the center of the phantom, Figure 49 (a). The absorption coefficient of the background is set using the black ink dye introduced in section 5.3.1, which has a quasi-flat absorption spectrum in the NIR spectral region, Figure 44 (b). The concentration of this dye is adjusted to provide an absorption coefficient of 0.009 mm^{-1}. Two NIR dyes (Dye 1: NIR869A and Dye 2: NIR782E, QCR solutions Corp, USA) were used in Inclusion 1 and Inclusion 2, respectively. Each of these two dyes has a different absorption spectrum in the NIR spectral region with a peak absorption at 869 nm for Dye 1, and 782 nm for Dye 2, Figure 49 (b). The concentrations C_{Dye1}= 0.014 M of Dye 1and C_{Dye2} = 0.009 M of Dye 2 were set to obtain an absorption contrast with respect to the background of the phantom.

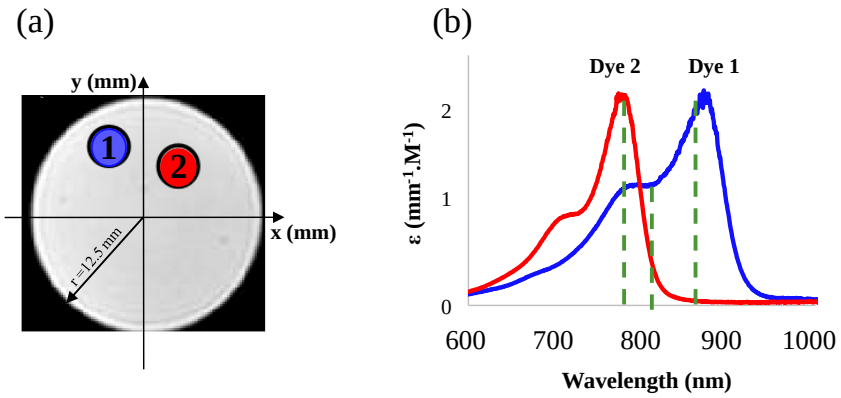

Figure 49: Description of the heterogeneous agar phantom used for the multi-wavelength PMI chromophore recovery: (a) Axial T1-weighted MR image showing a cross-section of the phantom. The inclusions are sketched on the phantom to show their size and position. (b) Extinction coefficient spectrum Dye 1 used to fill Inclusion 1 (blue), and Dye 2 used in Inclusion 2 (red) [67].

In this study, three illumination wavelengths were used (780 nm, 808 nm, and 860 nm). These wavelengths were chosen for this study since two of them are matching the absorption peak of these two dyes, while the 808 nm laser is close to their isosbestic point. The absorption coefficients at each wavelength of these two inclusions as well as the background are summarized in Table 11.

Table 11: Real absorption coefficient of Inclusion 1 and Inclusion 2 at the three used wavelengths [67].

	Real absorption coefficient (mm^{-1})		
	780 nm	**808 nm**	**860 nm**
Inclusion 1	0.023	0.023	0.038
Inclusion 2	0.026	0.014	0.0094
Background	0.009	0.009	0.009

5.4.2 MRT temperature measurements at multiple wavelengths

Multi-wavelength temperature measurements were collected to recover the concentration map of the dye in each inclusion. The MRT temperature maps at the three used wavelengths are shown in Figure 50.

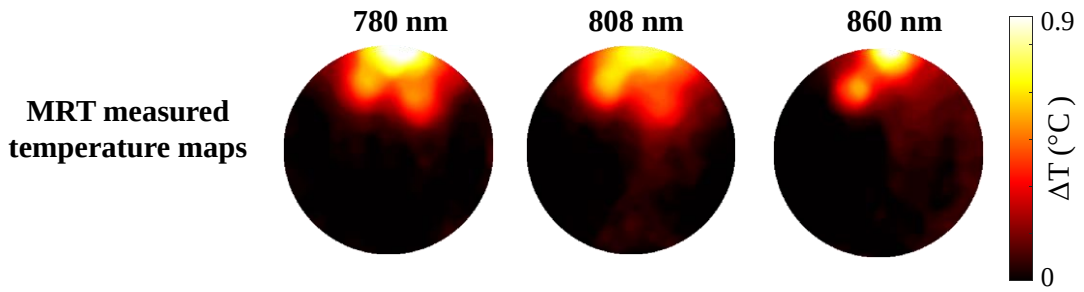

Figure 50: The temperature maps measured experimentally using MRT at 780 nm, 808 nm and 860 nm [67].

The increase in temperature at each wavelength depends on the position of the inclusion (distance from the source) as well as its local absorption coefficient. This is clearly noticed in the temperature maps acquired at 808 nm and 860 nm, where Inclusion 1 shows a higher increase in temperature compared to Inclusion 2. This is because Inclusion 1 was positioned closer to the source, and it has a higher absorption coefficient at these two wavelengths. However, a comparable increase in temperature is observed in both inclusions at 780 nm despite Inclusion 2 being located deeper. In fact, this is due to its higher absorption coefficient at this wavelength.

For further comparison, the real absorption coefficients of the dyes, summarized in Table 11, were used to generate simulated temperature maps using the PMI forward problem solver. Figure 51 shows that these simulated temperature maps exhibit a similar behavior to the one observed on the MRT measured maps, Figure 50.

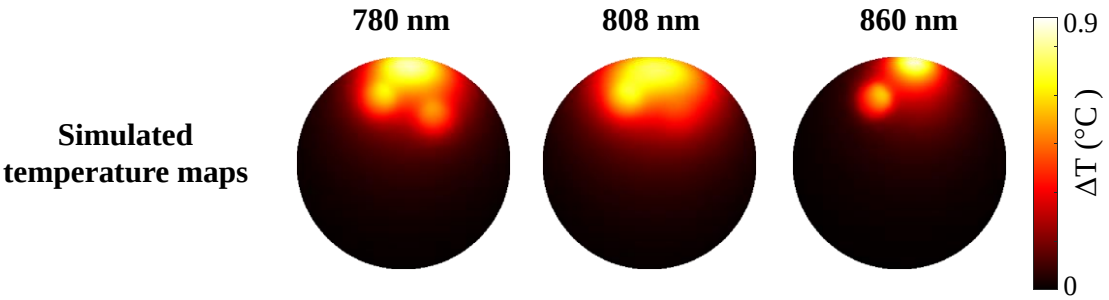

Figure 51: The simulated temperature maps at 780 nm, 808 nm and 860 nm [67].

5.4.3 Recovering the chromophore concentration: conventional method

5.4.3.1 Reconstruction of the absorption coefficient at multiple wavelengths

For each wavelength, the measured temperature map was used as an input for the PMI inverse problem solver to recover the high-resolution and quantitatively accurate corresponding absorption map, Figure 52.

As expected, the reconstructed absorption maps follow the dyes spectra presented in Figure 49 (b). Also, these absorption maps show that both inclusions are recovered with high-resolution regardless of their depth or position within the phantom. The accuracy of the recovered absorption map at each wavelength demonstrates the high performance of PMI. Indeed, the average error of the recovered absorption coefficient at the three wavelengths is as low as 14% for Inclusion 1 and 21% for Inclusion 2. This error represents the average mean absolute percentage error calculated at each wavelength, for each inclusion. However, one can observe some reconstruction artifacts. These artifacts are minimal since they only represent approximately 15% of the local absorption of the dyes. These absorption maps are obtained after only heating the phantom for 6 seconds. This heating period allows to only increase the internal temperature of the phantom to 0.9 °C, which is approximately nine times higher than the MRT noise level of 0.1 °C [52, 55].

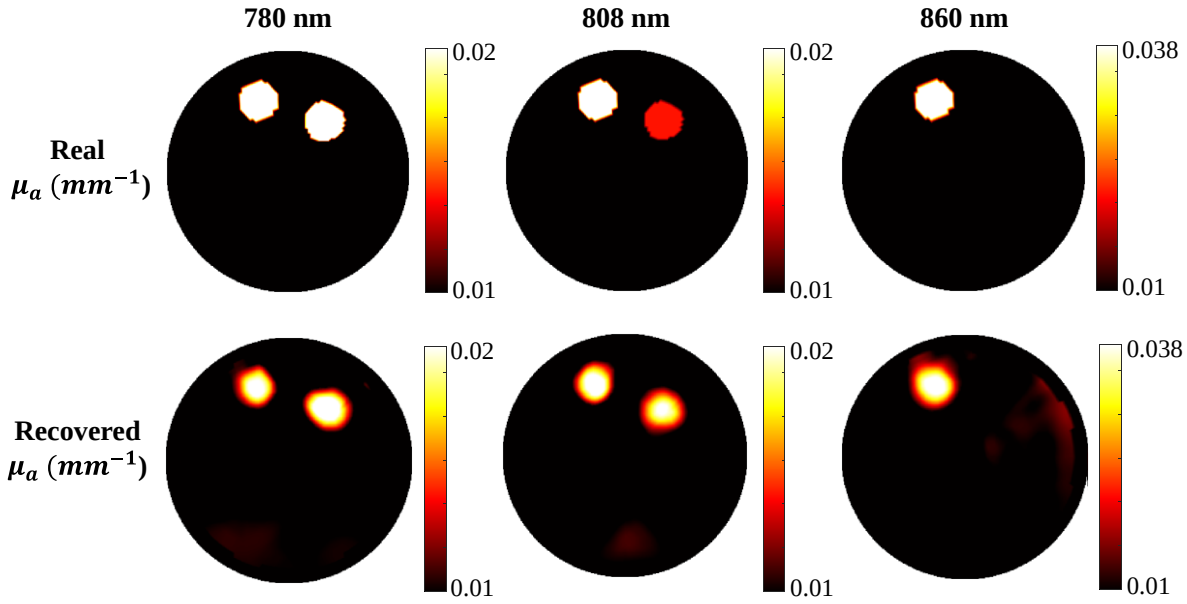

Figure 52: The real absorption maps (top) and the recovered absorption maps at 780 nm, 808 nm, and 860 nm (bottom) [67].

Table 12 summarizes the mean and standard deviation of the recovered absorption coefficient values.

Table 12: Mean and standard deviation of the recovered absorption coefficient of Inclusion 1, Inclusion 2 and the background at the three used wavelengths [67].

	Recovered absorption coefficient (mm^{-1})		
	780 nm	**808 nm**	**860 nm**
Inclusion 1	0.0182±0.0019	0.0193±0.0019	0.0365±0.0031
Inclusion 2	0.0205±0.0020	0.0179±0.0015	0.0108±0.0002
Background	0.0093±0.0006	0.0092±0.0005	0.0095±0.0010

5.4.3.2 Recovering the chromophore concentration

After solving the PMI inverse problem, the recovered absorption maps were then used in a least-square minimization process based on the Beer-Lambert Law to resolve the concentration maps of the two dyes. Figure 53 depicts the calculated concentration maps of the two dyes. Due to the high-resolution and accuracy of the recovered absorption maps, these concentration maps were recovered accurately with an average error of 13% and 29% for Dye 1 and Dye 2, respectively. As

expected, some artifacts are noticed in the concentration maps resulting from the minimization process. These artifacts resulted from the ones previously observed in the absorption maps. In fact, the recovered mean concentration outside the inclusions position was as low as 2.84×10^{-4} M and 2.28×10^{-4} M for Dye1 and Dye 2 concentration maps, respectively. These artifacts are minimal since their maximum values only represent an average of 13% of the concentration of the dyes. In addition, a little cross-talk is observed in Dye 1 concentration map from the contrast of Dye 2 with a mean value of 7.13×10^{-4} M.

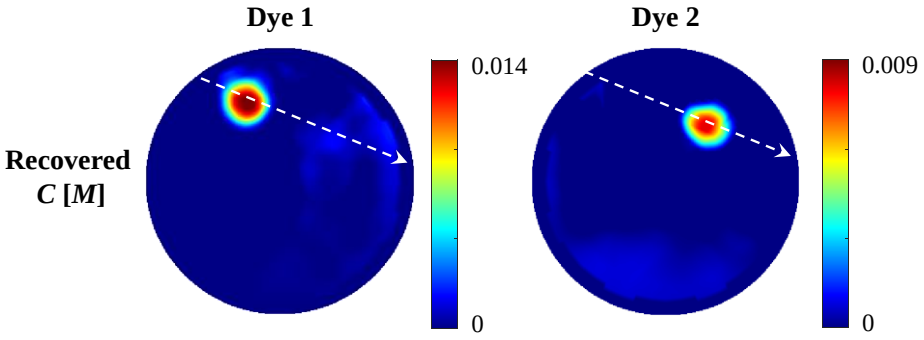

Figure 53: The recovered molar concentration maps of Dye 1 (left) and Dye 2 (right) obtained using the PMI conventional method. The dashed arrows show the position of the profiles presented in Figure 55 [67].

5.4.4 Recovering the chromophore concentration: direct method

Unlike the conventional method where each temperature map is processed individually, this method processes the MRT measured temperature maps collectively to recover the chromophore concentrations directly utilizing the newly developed spectrally constrained PMI algorithm [110].

The temperature maps presented in Figure 50 were used in the spectrally constrained PMI algorithm to directly recover the concentration of each dye by omitting the intermediate step of reconstructing the absorption coefficient, which is necessary for the conventional method. The

concentration was reconstructed directly with high-resolution and quantitative accuracy for both dyes with mean absolute percentage error of 12% and 22% for Dye 1 and Dyes 2, respectively. Figure 54 shows the recovered concentration maps obtained directly from the MRT temperature maps.

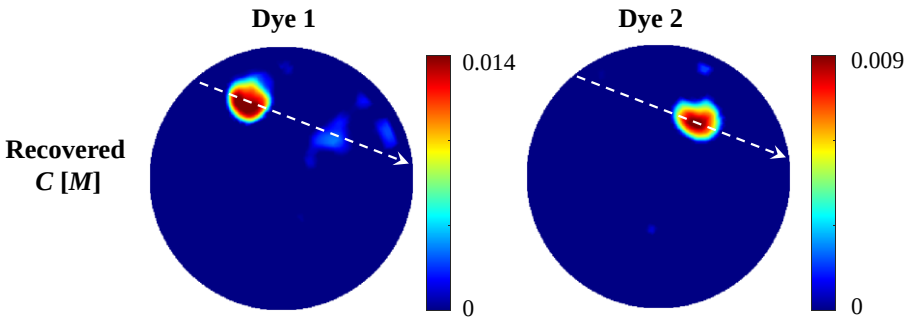

Figure 54: The recovered molar concentration maps of Dye 1 (left) and Dye 2 (right) obtained directly from temperature maps using the novel spectrally constrained reconstruction method. The dashed arrows show the position of the profiles presented in Figure 55 [110].

The resulted concentration maps show that the chromophore concentrations were recovered without any significant noise except a small artifact that represents an average of 17% of the concentration of both dyes. By excluding the position of both inclusions, the recovered mean concentration was found to be 0.001 M and 6.78×10^{-4} M for Dye 1 and Dye 2 concentration maps, respectively. Similar to the conventional method, a little cross-talk is observed in Dye 1 concentration map from the contrast of Dye 2 with a mean value of 8.8×10^{-4} M.

Furthermore, a change in the shape of Inclusion 2 is observed in the recovered concentration map of Dye 2. This shape deformation is due to the reconstruction parameters which has been utilized to compensate for the resulted cross-talk. Nevertheless, this deformation underestimated the size of the recovered inclusion with only 2% of its real size. In addition, it resulted of recovering 7% false positive values.

5.4.5 Comparison analysis of the reconstruction methods

A comparison between the performance of the two PMI reconstruction methods, the conventional and spectrally constrained direct reconstruction methods, on recovering the chromophore concentration has been made utilizing the results from section 5.4.3 and 5.4.4. To perform point-by-point comparison, profiles passing through the center of both inclusions are performed for each map and compared with the real concentration value, as shown in Figure 55. The position of the performed profile is presented as white dashed arrows on the recovered concentration maps, Figure 53 and Figure 54.

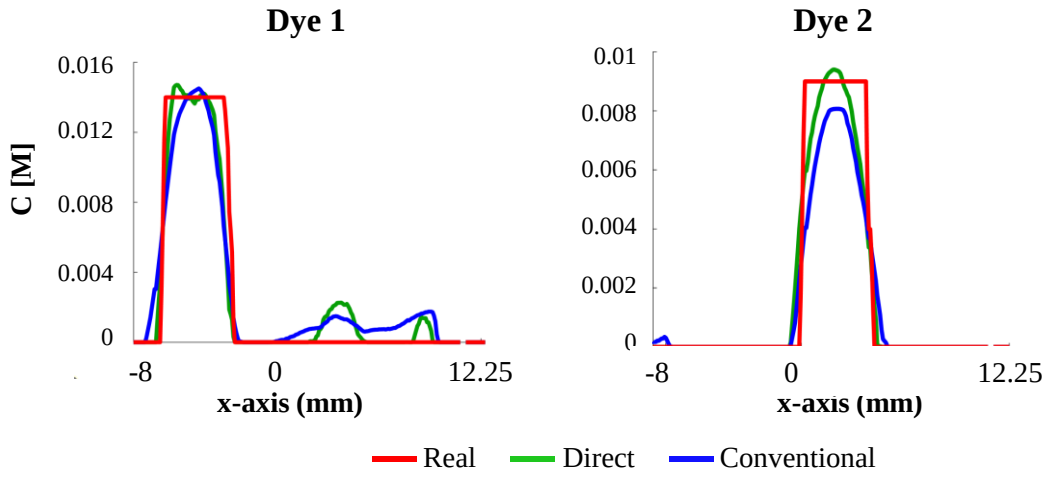

Figure 55: Chromophore concentration profiles passing through the center of both inclusions for Dye 1 and Dye 2 concentration maps. The real concentration (red), the recovered concentration using the direct method (green), and the conventional method (blue) [110].

These results show that the performance of both methods is comparable on recovering the chromophore concentration with high-resolution and quantitative accuracy. In both methods, a little cross-talk is observed in the Dye 1 concentration map from the contrast of Dye 2. The estimation of the cross-talk in the Dye 1 concentration map at the position of Inclusion 2 represents less than 12% for the concentration recovered using the direct method, and 11% when using the

conventional method. The cross-talk of Dye 2 into Dye 1 concentration map is defined as the measured contrast in Dye 1 map divided by the measured contrast in Dye 2 map at the position of inclusion 2 [105]. These cross-talks are very minimal demonstrating the higher performance of PMI compared to conventional DOT methodologies. For quantitative comparison, the recovered mean concentration and standard deviation of Dye 1 and Dye 2 using both approaches have been calculated and compared to the real concentration value as illustrated in Figure 56.

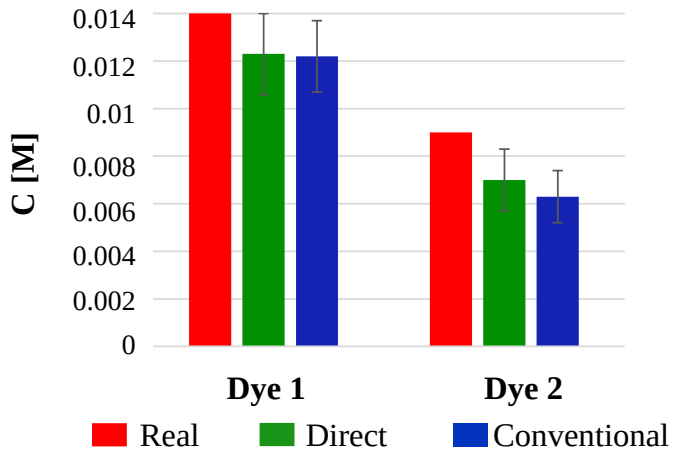

Figure 56: Real (red) and recovered mean concentration values with standard deviation error bars for Dye 1 (left) and Dye 2 (right) using the conventional (blue) and direct (green) methods [110].

The results show that the new technique is as accurate as the conventional method on recovering the chromophore concentration as in Dye 1 while it excelled on recovering a more reliable concentration value for the low concentration Dye 2. Indeed, the conventional PMI approach is based on the quality of the reconstructed absorption maps, which already has been extensively proven to be characterized with high-resolution and quantitative accuracy due to the well-posedness of the PMI inverse problem. On the other hand, the concentration recovered by PMI direct algorithm is accurate since there is no error translates from the recovered wavelength-dependent absorption maps to the resulted concentration maps.

In summary, utilizing the spectrally constrained direct reconstruction method allows to accurately recover the chromophore concentration from the temperature maps directly, in one step, instead of separately applying the reconstruction algorithm for each wavelength then inject the results in PMI conventional concentration recovery algorithm. Table 13 summarizes the average percentage error of the recovered concentration utilizing both methods. This quantification has been performed by defining the boundary of the inclusions at their full width at half maximum (FWHM) of the recovered concentration maps.

Table 13: The percentage error of the recovered concentration of Dye 1 and Dye 2 using PMI conventional and direct methods.

	Percentage error (%)	
	Conventional	**Direct**
Dye 1	13 %	12 %
Dye 2	29 %	22 %

These results demonstrated the PMI robustness on recovering chromophore concentration in a tissue-like phantom.

Chapter 6: Performance evaluation of multi-wavelength PMI ex vivo

After validating the performance of the multi-wavelength PMI on phantom studies, animal studies were conducted. In this chapter, the performance was evaluated on animal *ex vivo* studies. In addition, before proceeding with *in vivo* imaging, a simulation study was performed to investigate the effect of the blood perfusion rate on the recovered absorption coefficient.

6.1 Animal experimental study

6.1.1 Animal preparation

A fisher rat injected subcutaneously with the R3230 AC adenocarcinoma tumor model was used for this ex vivo study. The acquisition of the data was initiated 3 weeks after implanting the tumor cells when the tumor size reached 1 cm in diameter. Before performing the experiment, the rat was prepared for the laser illumination by removing the hair around imaging area.

6.1.2 Experimental procedure

The Fisher rat bearing the R3230 breast tumor model was placed on the plastic bed inside the RF Philips SENSE 8-channel wrist coil. Two CuSO4-filled markers were placed between and in parallel to the optical fiber to align the laser illumination plane with the MRI slice that shows the tumor. A high-resolution T2 weighted image was acquired to locate the tumor and to be used as a mask when processing the data, Figure 57.

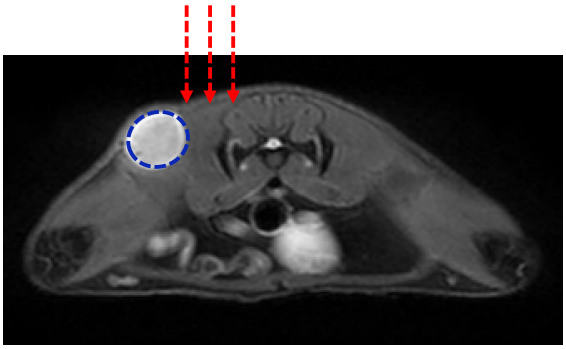

Figure 57: A T2 weighted MR image of the Fisher rat bearing the R3230 breast tumor model. The tumor region is outlined with a dashed-line in blue color. The red dashed arrows represent the position of the laser source.

In this experiment, the dynamic MR temperature sequence acquisition is initiated using a gradient echo sequence with repetition time TR at 82 ms and echo time TE at 12 ms, FOV = 80 mm*80 mm, MR image pixel size is 0.2000 *0.2000 mm^2, and a 5 mm slice thickness to acquire MR phase maps. These MRI parameters resulted in 8.2 seconds temporal resolution per frame.

6.1.3 MRT temperature measurements at multiple wavelengths

Prior to the multi-wavelength PMI experiment, data were acquired using single wavelength but with different power levels for laser power optimization. In this part of the experiment, the rat was illuminated from its top side using laser 760 nm with two power levels, 1 W and 1.5 W. For each power level, the temperature measurements were acquired for 82 seconds. During this time, 10 frames were obtained divided as 4 baseline and 6 heating frames. After acquiring the measurements of the first power level, a break was given for few minutes until its temperature went back to the baseline temperature.

The experiments were performed in a very short time after the rat was sacrificed. The increase in temperature at the area under the laser beam was studied for both power levels. To compare the increase in the temperature in both cases, the mean temperature values at this ROI

were calculated. Figure 58 shows the temporal temperature profiles when the low laser power (blue) and the high power (red) were utilized.

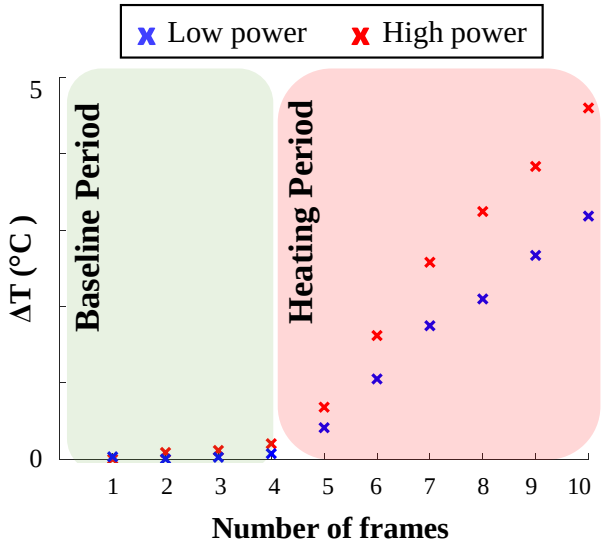

Figure 58: Temporal temperature profiles at the laser beam area during the baseline and heating periods when utilizing laser power of 1 W (blue) and 1.5 W (red).

This study shows that the highest increase in the temperature at the laser beam area was 3.2 °C for the low-power case and 4.6 °C for the high-power one. The max temperature was reached following 49 seconds of laser illumination. Based on these results, the experimental parameters for the multi-wavelength experiment were chosen. For example, the laser power was chosen to be 1.5 W. This laser power level was preferred to avoid the long operation time of the laser diode as well as to achieve high temperature to noise measurements. In addition, the number of frames was chosen to be only 3 frames during the heating period to not overheat the subject.

For the multi-wavelength PMI experiment, four wavelengths were used. For each wavelength, 4 baseline frames were obtained then the laser was turned on at the end of the fourth frame to illuminate the rat for three frames. After data acquisition was completed for each wavelength, a short duration of time is taken to ensure that the generated heat had dissipated before

moving to the next laser wavelength. The total time for this experiment was around 10 minutes. Figure 59 illustrates the rat temperature map at each wavelength after 25 seconds of laser illumination.

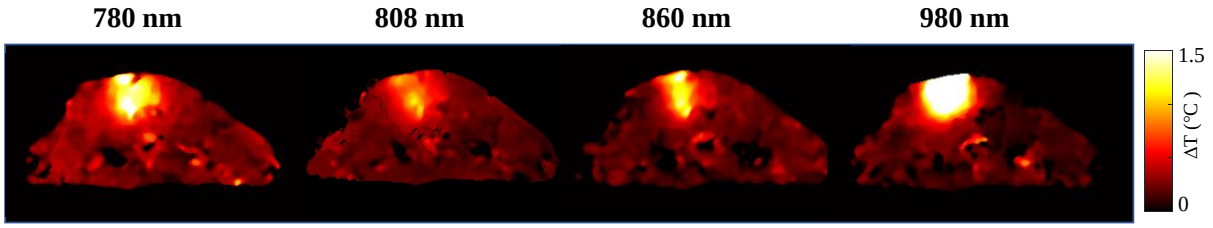

Figure 59: Rat temperature maps acquired experimentally after 25 seconds of laser illumination at (780 nm, 808 nm, 860 nm, and 980 nm).

Although the same level of the laser power was utilized for all wavelengths in this experiment, the increase in temperature was varying with wavelength due to the change in the absorption coefficient. The temperature increase at the tumor area was calculated at each wavelength in order to study the temperature change with respect to the utilized wavelength. Table 14 summarizes the mean temperature value at the tumor area at each wavelength.

Table 14: The calculated mean temperature value at the tumor area at the utilized wavelength.

Wavelength (nm)	780	808	860	980
ΔT (°C)	0.46	0.30	0.31	1.22

This study validated that the temperature change follows the optical absorption coefficient spectrum, shown in Figure 3, with hemoglobin presenting in its oxygen-unloaded form (deoxy-hemoglobin) and a maximum temperature increase at 980 nm. Performing this study was beneficial to facilitate the transition to the future *in vivo* studies.

6.2 The effect of blood perfusion rate on the recovered absorption coefficient: simulation study

For all the previous phantom studies, the distributions of laser-induced temperature were modeled using the heat conduction equation, equation (19). In order to transfer from simple phantom studies to more complicated animal *in vivo* studies, Pennes bioheat equation, that includes a special term which accounts for the effect of blood perfusion should be applied, equation (21). This term describes that the rate of heat exchange between blood flow and tissue is proportional to the product of a volumetric perfusion rate and the difference between the temperature of arterial blood T_a and the local tissue temperature T. The main assumption of this model is that the blood enters a specific volume at the temperature of arterial blood and leaves it with the local tissue temperature. Therefore, the heat distribution is affected by the blood flow as the heat is dissipated; hence, it is modeled as a heatsink.

To study the effect of incorporating the blood perfusion term during PMI *in vivo* studies, multiple simulation studies were performed to quantify the dependency of the recovered absorption coefficient on the temperature loss due to the blood flow.

6.2.1 Building the numerical phantom

For these studies, the FEM mesh was generated with 3764 nodes from a T2 weighted MR image of a mouse bearing a subcutaneous tumor, Figure 60. The mesh was divided into two regions, tumor and normal tissue, by segmenting the tumor boundaries as outlined in the green line in Figure 60.

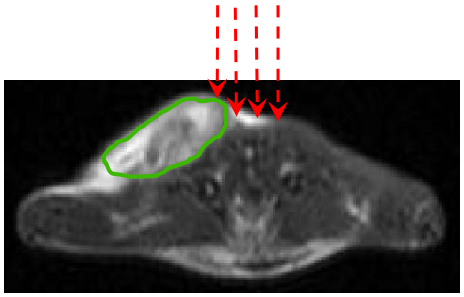

Figure 60: A T2 weighted MR image of a mouse with a subcutaneous tumor. The tumor region is outlined with green color. The red dashed arrows represent the position of the laser source.

In order to study the blood perfusion effect, single wavelength, λ=808 nm, was used for the following studies. The optical properties of the used numerical phantom were adjusted to be equal to the average animal optical properties. Therefore, the absorption and reduced scattering coefficients of the normal tissue were set to 0.01 mm^{-1} and 0.8 mm^{-1}, respectively. The absorption coefficient of the tumor was set to be two times higher than the normal tissue in the background.

For tissue thermal properties, living tissue properties were used for both regions. For the blood thermal properties, one value was homogenously distributed in each region instead of modeling blood vessels individually. Blood perfusion rate of normal tissue and tumor were set to 3×10^{-3} sec^{-1} and 6×10^{-3} sec^{-1}, respectively [133].

6.2.2 Generation of synthetic measurements

The numerical mouse was illuminated from its top side using one illumination window as illustrated in the red dashed arrows in Figure 60. The temperature map at the utilized wavelength was then generated by solving the PMI forward problem, where the heat transfer in the medium is modelled by accounting for the blood perfusion term and by neglecting this term as shown in Figure 61 (a) and Figure 61 (b), respectively.

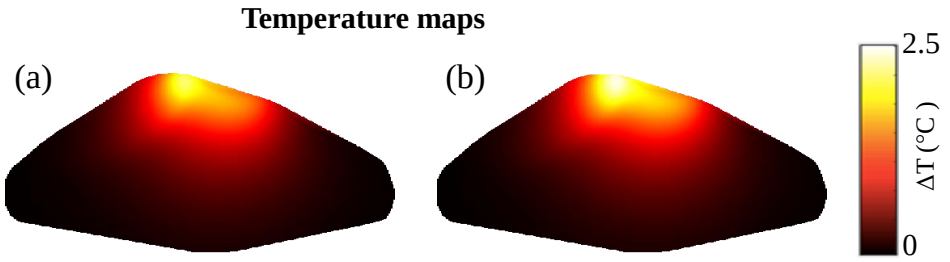

Figure 61: Simulated temperature maps at laser 808 nm generated: (a) with and (b) without the blood perfusion term.

These temperature maps indicate that the tumor is on the left side absorbs more light due to its higher absorption, resulting of higher increase in temperature. In addition, these temperature maps show that there is a maximum of 0.32 °C temperature loss when the blood perfusion rate term was taken into consideration, Figure 61 (a).

6.2.3 Recovering the tumor absorption coefficient

To study the effect of the blood perfusion rate on the recovered absorption coefficient, the absorption distribution is recovered by solving the PMI inverse problem for multiple cases, and the quantitative accuracy was evaluated for each case. The temperature map modelled by accounting for the blood perfusion term, Figure 61 (a), was used as a temperature measurement input in the PMI inverse problem for all the following cases.

6.2.3.1 Case study 1: without the blood perfusion rate

In this case study, the absorption coefficient map was recovered by neglecting the blood perfusion effect for both tumor and normal tissue, Figure 62.

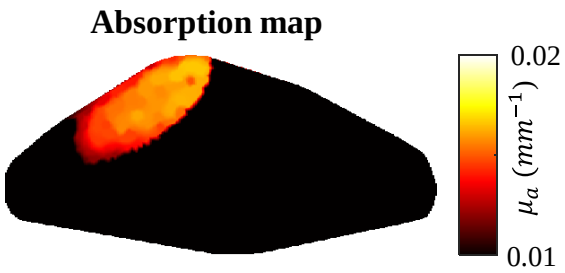

Figure 62: The absorption map recovered by neglecting the blood perfusion rate with 21.8% error.

This absorption map shows that the tumor was correctly detected, but the recovered absorption value was underestimated. The absorption of the tumor was recovered with average percentage error of 21.8%.

6.2.3.2 Case study 2: with the blood perfusion rate

The blood perfusion rate values of normal and tumor tissue were used in this study to recover the absorption of the tumor, Figure 63. In this case, the absorption of the tumor was recovered with average percentage error of 3.5%.

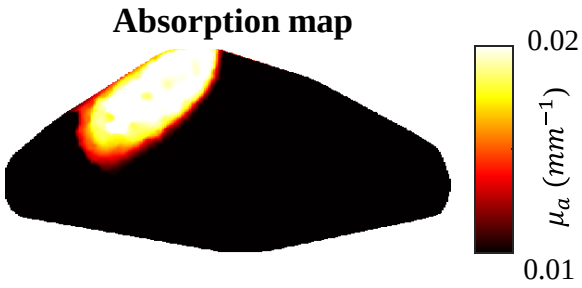

Figure 63: The absorption map recovered with 3.5% error by using the blood perfusion rate value of both tumor and normal tissue.

This result indicates that the blood perfusion rate has a noticeable impact on the recovered absorption coefficient since the percentage error decreased by 18% when it was incorporating during the calculation.

6.2.3.3 Additional cases

6.2.3.3.1 Case 1: unknown tumor position

Additional cases were also evaluated by using temperature map with the blood perfusion term such as: studying the effect on the recovered absorption if the position of the tumor is unknown or if the anatomical MRI image is not available. In this case, the temperature map was generated while using the blood perfusion rate of normal tissue only, Figure 64 (a). By comparing this temperature map to the one where the perfusion values were correctly assigned Figure 61 (a), the maximum temperature difference is found to be equal to 0.14 °C with higher temperature loss for the higher blood perfusion contrast.

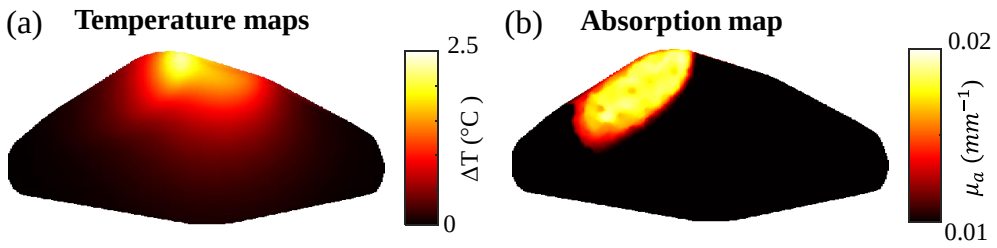

Figure 64: (a) Temperature map generated using blood perfusion rate of normal tissue only. (b) The recovered absorption map for this case with average of 13.1% percentage error.

Due to the inaccuracy on the blood perfusion contrast of the tumor to the background, the tumor absorption coefficient was recovered with average percentage error of 13.1%, Figure 64 (b).

6.2.3.3.2 Case 2: unknown tumor size

Another case was performed to assess the dependency of the recovered absorption coefficient on the perfusion spatial resolution. In this case, the temperature map was generated by assigning the tumor blood perfusion value to inaccurate tumor size. For example, the tumor size

was assumed to be 2 mm (case 2.a) and 4 mm (case 2.b) less than the correctly segmented tumor size, the green line in Figure 60. The temperature maps were generated for these two cases and used in the PMI inverse problem to recover the absorption coefficients map, Figure 65. The maximum difference in the temperature between these two cases was only 0.06°C, with higher temperature loss for the larger sized case.

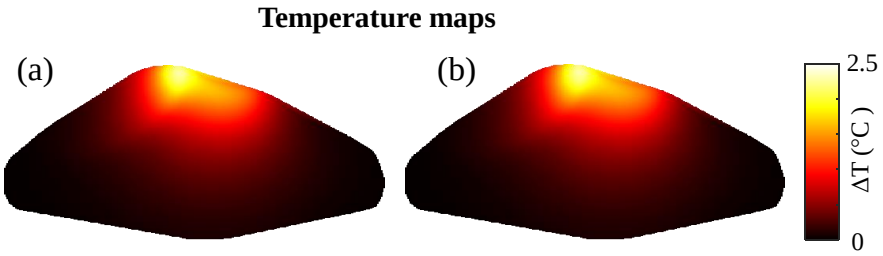

Figure 65: Temperature maps generated when the tumor size was assumed to be (a) case 2.a: 2 mm and (b) case 2.b: 4 mm less than the real size of the tumor.

The distribution of the absorption coefficient was recovered for each case and the error on the recovered value was evaluated over the correct tumor size. By decreasing the assigned tumor size by 2 mm, the average percentage error of the recovered absorption was 6.8%, while the error increased by 2.7% when decreases the tumor size by 4 mm of its real size. Figure 66 shows the recovered absorption maps for these two cases.

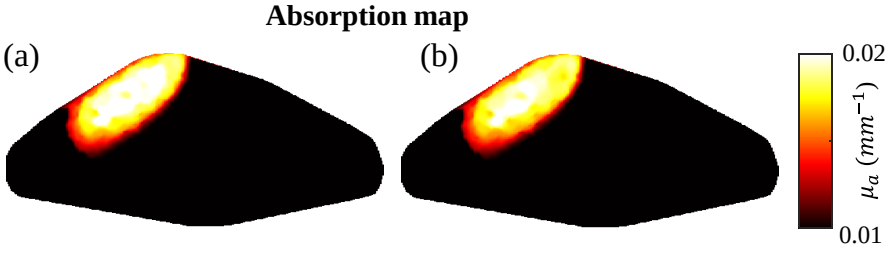

Figure 66: The absorption maps recovered when the tumor size was assumed to be (a) case 2.a: 2 mm and (b) case 2.b: 4 mm less than the real size of the tumor. These absorption maps recovered with 6.8% and 9.5% error, respectively.

In summary, these results indicate that incorporating the blood perfusion rate is important for accurate absorption coefficient recovery. Employing the blood perfusion of the tumor also has

an impact on the accuracy. While the inaccuracy on the segmented tumor size does not have a significant effect. Table 15 summarizes the mean and standard deviation of the tumor recovered absorption coefficient for each case and the corresponding percentage error.

Table 15: Mean and standard deviation of the recovered absorption coefficient of the tumor and the percentage error for all the performed cases.

Case		**Recovered absorption**	
		μ_a (mm^{-1})	**Percentage error (%)**
1		0.0156±0.0008	21.8
2		0.0193±0.0014	3.5
Additional cases	1	0.0174±0.011	13.1
	2.a	0.0186±0.0014	6.5
	2.b	0.0181±0.0013	9.5

In general, the accuracy of the recovered absorption can be also improved by illuminating the object from multiple sides. Indeed, all the recovered absorption maps presented in this section show an error at the lower left boundary of the tumor due to receiving less temperature.

Chapter 7: Conclusions and future work

7.1 Conclusion

This thesis introduced a novel high-resolution diffuse optical imaging technique that combined the high-resolution of MRI with the sensitivity of DOT to provide accurate chromophore concentration maps. The stand-alone DOT suffers from serious limitations, mainly the low spatial resolution of the obtained functional information. This is due to the fact that only the boundary measurements can be acquired. Unlike DOT, PMI utilizes laser to induce a relatively low temperature increase in the medium, while measuring the laser-induced temperature from the whole medium using MRT. Previously, single-wavelength PMI was introduced as an imaging technique that provides spatially distributed optical absorption from the measured temperature map. In order to provide tissue functional information, the single-wavelength PMI technique was upgraded to the multiple-wavelength version to convert the measured temperature maps into chromophore concentration maps. Providing the distribution of endogenous chromophores such as oxy- and deoxy-hemoglobin as well as lipid and water is important as the concentration of these chromophores are directly correlated with the malignancy of tumorous tissue.

In this thesis, two image reconstruction algorithms were developed to recover the chromophore concentration. In the conventional approach, the laser-induced temperature map measured at each wavelength is used in the image reconstruction algorithm to recover the corresponding absorption map at the employed wavelength. Then, the chromophore concentrations are obtained from all the recovered absorption maps using the Beer Lambert law. The second novel approach is based on recovering the chromophore concentration directly from the MRT temperature maps by imposing prior spectral information into the image reconstruction algorithm.

The performance of both approaches was tested on numerical phantoms via simulation studies. The results of these simulation studies were encouraging for the design and development of the multi-wavelength PMI system.

The development details of the multi-wavelength PMI system that utilizes five laser wavelengths ranging between 760 nm and 980 nm were presented in this work. This system can noninvasively be used to induce an internal temperature increase within a medium at five wavelengths to recover endogenous and exogenous chromophore concentrations. Initially, the system went through series of tests and characterization. Afterwards, the performance of the new system was experimentally validated on different homogenous and heterogeneous agar tissue-simulating phantoms. Finally, the feasibility of the multi-wavelength PMI technique for recovering chromophore concentrations was demonstrated on homogenous and heterogeneous phantoms. In these studies, the concentration distributions of the phantom constituents were accurately recovered using both reconstruction methods.

PMI is a safe imaging modality as it utilizes nonionizing radiation, and because it elevates the internal temperature a few degrees without altering the physiological process in the body or causing thermal damage. Indeed, as presented in this thesis, PMI temperature measurements are acquired in a few seconds after turning the laser on to induce a slight increase in the internal temperature. This increase in temperature has to be higher than the MRT noise level but lower than hyperthermia to avoid protein denaturation. Multi-wavelength PMI has the potential to be used in various medical applications since it is safe and can provide functional information with high-resolution and quantitative accuracy. For example, multi-wavelength PMI can be used to detect and diagnose different cancerous tumors as long as a sufficient heating is achieved. Consequently, the power of the laser is adjusted based on the size of the imaged tissue. For imaging of large

organs such as the breast, multiple illumination sites must be used, and high laser power has to be applied. On the other hand, for internal organs such as ovarian imaging, PMI fiber can be inserted internally to ensure achieving the required heat. In fact, multi-wavelength PMI is not only beneficial for tumor detection and characterization but also for other diseases where the oxygen saturation level and blood volume are used as biomarkers such as mapping of human brain function and detection of joint inflammations diseases. Furthermore, applications of photothermal therapy applied at any NIR wavelengths can benefit from this PMI technique. Indeed, the PMI recovered total absorption can be used during photothermal therapy planning in order to determine important parameters. For example, it can obtain laser power as well as laser exposure time needed to attain a specific increase in temperature prior to treatment throughout simulation studies.

7.2 Future work

Although demonstrating a high-performance level, multi-wavelength PMI in its current form remains limited due to several factors. For example, a short penetration depth was noticed especially at laser wavelength 980 nm due to the high optical absorption coefficient at this wavelength. The heating penetration depth can be enhanced by illuminating the volume under investigation from multiple sides to increase the SNR in the whole volume, which consequently increases the depth of penetration. Hence, future PMI studies will be performed with four illumination windows instead of one. Additionally, PMI reconstructions are conducted while considering some assumptions such as the value of the reduced scattering coefficient. This parameter was measured using a DOT system at one wavelength while the values at other wavelengths were estimated based on the Mie theory. However, for higher accuracy, this parameter has to be found at each wavelength individually. In fact, the multi-wavelength measurements of PMI can also be used to recover the spatially resolved scattering coefficient. In

the future, an updated version of the PMI image reconstruction algorithm has to be implemented to obtain not only the chromophore concentrations but also the scattering amplitude allowing PMI to be a stand-alone modality [103, 115].

Also, the thermal properties of the used phantoms were assumed to be equal to those of water and homogeneously attributed to the entire medium. Nevertheless, for the future *in vivo* studies, the thermal properties of each organ should be set based on relevant literature, where T1 weighted anatomical image is used for organ segmentation. Also, *in vivo* imaging will require upgrading the modeling process by using the Pennes bioheat equation in order to account for the tissue blood perfusion.

Another limitation results of the fact that PMI utilizes the PRF shift method to monitor the laser-induced temperature. Although PRF shift method has been shown to be robust in aqueous tissue, this method has some challenges. One of the main challenges is that the temperature changes in adipose tissue (such as breast and abdomen tissue) cannot be detected using this approach due to the lack of water molecules in adipose tissue. Having a mixture of adipose and aqueous tissue in the same voxel would underestimate the measured temperature variation and thereby affect the accuracy of the temperature measurements. To overcome this limitation during PMI image reconstruction, temperature measurements at adipose tissue should be removed from PMI measurements vector, where the region of the adipose tissue can be defined from MRI anatomical image. Utilizing multiple MRT methods to monitor temperature simultaneously such as PRF and T1, is also a useful approach. In this method, the PRF is used to monitor temperature in aqueous tissue while T1 is used to monitor temperature in the adipose tissue.

Before translating PMI to the clinical arena, this technique has to be upgraded to a three-dimensional (3-D) imaging modality to capture all the small details that are not available in the 2-

D PMI version. In this case, the 3-D MRT data acquisition sequence should be employed during the experiments to obtain 3-D temperature maps. The PMI image reconstruction algorithm should also be expanded to a 3-D framework to recover 3-D volumetric concentration maps. Furthermore, in the current PMI stage, the concentration is obtained in a post processing step. However, this upgrade necessitates the acceleration of the PMI image reconstruction algorithm to facilitate the transition of PMI to the clinical arena.

Reference

1. Nioka, S. and B. Chance, *NIR spectroscopic detection of breast cancer.* Technology in cancer research & treatment, 2005. **4**(5): p. 497-512.
2. Weissleder, R., *A clearer vision for in vivo imaging*. 2001, Nature Publishing Group.
3. Eggebrecht, A.T., et al., *Mapping distributed brain function and networks with diffuse optical tomography.* Nat Photonics, 2014. **8**(6): p. 448-454.
4. Lin, Y., et al., *A photo-multiplier tube-based hybrid MRI and frequency domain fluorescence tomography system for small animal imaging.* Phys Med Biol, 2011. **56**(15): p. 4731-47.
5. Pogue, B.W., et al., *Comparison of imaging geometries for diffuse optical tomography of tissue.* Optics express, 1999. **4**(8): p. 270-286.
6. Farina, A., et al., *Multiple-view diffuse optical tomography system based on time-domain compressive measurements.* Optics letters, 2017. **42**(14): p. 2822-2825.
7. Alayed, M., et al., *Time-resolved diffuse optical tomography system using an accelerated inverse problem solver.* Optics express, 2018. **26**(2): p. 963-979.
8. Gibson, A. and H. Dehghani, *Diffuse optical imaging.* Philos Trans A Math Phys Eng Sci, 2009. **367**(1900): p. 3055-72.
9. Jacques, S.L., *Optical properties of biological tissues: a review.* Physics in medicine and biology, 2013. **58**(11): p. R37.
10. Vavadi, H., et al., *Compact ultrasound-guided diffuse optical tomography system for breast cancer imaging.* Journal of biomedical optics, 2018. **24**(2): p. 021203.
11. Ruiz, J., et al., *Breast density quantification using structured-light-based diffuse optical tomography simulations.* Applied optics, 2017. **56**(25): p. 7146-7157.
12. Yazdi, H.S., et al., *Mapping breast cancer blood flow index, composition, and metabolism in a human subject using combined diffuse optical spectroscopic imaging and diffuse correlation spectroscopy.* Journal of biomedical optics, 2017. **22**(4): p. 045003.
13. Pakalniskis, M.G., et al., *Tumor angiogenesis change estimated by using diffuse optical spectroscopic tomography: demonstrated correlation in women undergoing neoadjuvant chemotherapy for invasive breast cancer?* Radiology, 2011. **259**(2): p. 365-74.
14. Anderson, P.G., et al., *Broadband optical mammography: chromophore concentration and hemoglobin saturation contrast in breast cancer.* PLoS One, 2015. **10**(3): p. e0117322.
15. Leproux, A., et al., *Differential diagnosis of breast masses in South Korean premenopausal women using diffuse optical spectroscopic imaging.* Journal of biomedical optics, 2016. **21**(7): p. 074001.
16. Tromberg, B.J., et al., *Imaging in breast cancer: diffuse optics in breast cancer: detecting tumors in pre-menopausal women and monitoring neoadjuvant chemotherapy.* Breast Cancer Res, 2005. **7**(6): p. 279-85.
17. Cerussi, A.E., et al., *In vivo absorption, scattering, and physiologic properties of 58 malignant breast tumors determined by broadband diffuse optical spectroscopy.* Journal of biomedical optics, 2006. **11**(4): p. 044005.
18. Fishell, A.K., et al., *Portable, field-based neuroimaging using high-density diffuse optical tomography.* Neuroimage, 2020. **215**: p. 116541.
19. Wu, H.Y., et al., *Development of a multi-wavelength diffuse optical tomography system for early diagnosis of rheumatoid arthritis: simulation, phantoms and healthy human studies.* Biomedical Optics Express, 2016. **7**(11): p. 4769-4786.
20. Lighter, D., et al., *Multispectral, non-contact diffuse optical tomography of healthy human finger joints.* Biomedical optics express, 2018. **9**(4): p. 1445-1460.
21. Cochran, J., et al., *Longitudinal optical monitoring of blood flow in breast tumors during neoadjuvant chemotherapy.* Physics in Medicine & Biology, 2017. **62**(12): p. 4637.

22. Altoe, M.L., et al., *Changes in Diffuse Optical Tomography Images During Early Stages of Neoadjuvant Chemotherapy Correlate with Tumor Response in Different Breast Cancer Subtypes.* Clinical Cancer Research, 2021.
23. Arridge, S., *Optical tomography in medical imaging.* Inverse Problems, 1999. **15**(2): p. R41-R93.
24. Elsabahy, M., et al., *Polymeric nanostructures for imaging and therapy.* Chemical reviews, 2015. **115**(19): p. 10967-11011.
25. Wallyn, J., et al., *Biomedical imaging: principles, technologies, clinical aspects, contrast agents, limitations and future trends in nanomedicines.* Pharmaceutical research, 2019. **36**(6): p. 78.
26. Lin, Y., et al., *Tumor characterization in small animals using magnetic resonance-guided dynamic contrast enhanced diffuse optical tomography.* J Biomed Opt, 2011. **16**(10): p. 106015.
27. Cochran, J.M., et al., *Hybrid time-domain and continuous-wave diffuse optical tomography instrument with concurrent, clinical magnetic resonance imaging for breast cancer imaging.* Journal of biomedical optics, 2019. **24**(5): p. 051409.
28. Lin, Y., et al., *Quantitative fluorescence tomography using a combined tri-modality FT/DOT/XCT system.* Optics Express, 2009.
29. Zimmermann, B.B., et al., *Multimodal breast cancer imaging using coregistered dynamic diffuse optical tomography and digital breast tomosynthesis.* Journal of Biomedical Optics, 2017. **22**(4): p. 046008.
30. Zhu, Q., et al., *Assessment of functional differences in malignant and benign breast lesions and improvement of diagnostic accuracy by using US-guided diffuse optical tomography in conjunction with conventional US.* Radiology, 2016. **280**(2): p. 387-397.
31. Zhang, L., et al., *Direct regularization from co-registered anatomical images for MRI-guided near-infrared spectral tomographic image reconstruction.* Biomedical optics express, 2015. **6**(9): p. 3618-3630.
32. Althobaiti, M., H. Vavadi, and Q. Zhu, *Diffuse optical tomography reconstruction method using ultrasound images as prior for regularization matrix.* Journal of biomedical optics, 2017. **22**(2): p. 026002.
33. Dehghani, H., et al., *Numerical modelling and image reconstruction in diffuse optical tomography.* Philos Trans A Math Phys Eng Sci, 2009. **367**(1900): p. 3073-93.
34. Kwong, T.C., et al., *Differentiation of tumor vasculature heterogeneity levels in small animals based on total hemoglobin concentration using magnetic resonance-guided diffuse optical tomography in vivo.* Applied optics, 2016. **55**(21): p. 5479-5487.
35. Attia, A.B.E., et al., *A review of clinical photoacoustic imaging: Current and future trends.* Photoacoustics, 2019. **16**: p. 100144.
36. Choi, W., D. Oh, and C. Kim, *Practical photoacoustic tomography: Realistic limitations and technical solutions.* Journal of Applied Physics, 2020. **127**(23): p. 230903.
37. Toi, M., et al., *Visualization of tumor-related blood vessels in human breast by photoacoustic imaging system with a hemispherical detector array.* Scientific reports, 2017. **7**(1): p. 1-11.
38. Lin, L., et al., *Single-breath-hold photoacoustic computed tomography of the breast.* Nature communications, 2018. **9**(1): p. 1-9.
39. Jo, J., et al., *Photoacoustic tomography for human musculoskeletal imaging and inflammatory arthritis detection.* Photoacoustics, 2018. **12**: p. 82-89.
40. Upputuri, P.K. and M. Pramanik, *Dynamic in vivo imaging of small animal brain using pulsed laser diode-based photoacoustic tomography system.* Journal of biomedical optics, 2017. **22**(9): p. 090501.
41. Shan, T., et al., *In-vivo hemodynamic imaging of acute prenatal ethanol exposure in fetal brain by photoacoustic tomography.* Journal of biophotonics, 2020. **13**(5): p. e201960161.
42. Burgholzer, P., et al., *Resolution limits in photoacoustic imaging caused by acoustic attenuation.* Journal of Imaging, 2019. **5**(1): p. 13.
43. Jeon, S., et al., *Review on practical photoacoustic microscopy.* Photoacoustics, 2019. **15**: p. 100141.

44. Alshahrani, S.S., et al., *All-reflective ring illumination system for photoacoustic tomography.* Journal of biomedical optics, 2019. **24**(4): p. 046004.
45. Xia, J., et al., *Whole-body ring-shaped confocal photoacoustic computed tomography of small animals in vivo.* Journal of biomedical optics, 2012. **17**(5): p. 050506.
46. Nishiyama, M., et al., *Ring-array photoacoustic tomography for imaging human finger vasculature.* Journal of biomedical optics, 2019. **24**(9): p. 096005.
47. Wang, X., et al., *Noninvasive imaging of hemoglobin concentration and oxygenation in the rat brain using high-resolution photoacoustic tomography.* J Biomed Opt, 2006. **11**(2): p. 024015.
48. Thayer, D.A., et al., *Laser-induced photo-thermal magnetic imaging.* Appl Phys Lett, 2012. **101**(8): p. 83703.
49. Lin, Y., et al., *Photo-magnetic imaging: resolving optical contrast at MRI resolution.* Physics in Medicine & Biology, 2013. **58**(11): p. 3551.
50. Luk, A.T., et al. *A true multi-modality approach for high resolution optical imaging: photo-magnetic imaging*. in *Multimodal Biomedical Imaging IX*. 2014. International Society for Optics and Photonics.
51. Luk, A.T., et al. *A novel high-resolution optical imaging modality: photo-magnetic imaging*. in *Multimodal Biomedical Imaging VIII*. 2013. International Society for Optics and Photonics.
52. Luk, A., et al., *Ex vivo validation of photo-magnetic imaging.* Optics letters, 2017. **42**(20): p. 4171-4174.
53. Luk, A.T., et al. *Monitoring gold nanoparticle distribution with high resolution using photo-magnetic imaging*. in *Optical Interactions with Tissue and Cells XXVII*. 2016. International Society for Optics and Photonics.
54. Nouizi, F., et al., *Real-time photo-magnetic imaging.* Biomedical Optics Express, 2016. **7**(10): p. 3899-3904.
55. Nouizi, F., et al., *Experimental validation of a high-resolution diffuse optical imaging modality: photomagnetic imaging.* J Biomed Opt, 2016. **21**(1): p. 16009.
56. Nouizi, F., et al. *Analytical Photo Magnetic Imaging*. in *Optical Tomography and Spectroscopy*. 2016. Optical Society of America.
57. Nouizi, F., et al., *An accelerated photo-magnetic imaging reconstruction algorithm based on an analytical forward solution and a fast Jacobian assembly method.* Phys Med Biol, 2016. **61**(20): p. 7448-7465.
58. Tagirov, R. and L. Tagirov, *Lambert formula—Bouguer absorption law?* Russian physics journal, 1997. **40**(7): p. 664-669.
59. Wang, J., et al., *Spectral tomography with diffuse near-infrared light: inclusion of broadband frequency domain spectral data.* Journal of biomedical optics, 2008. **13**(4): p. 041305.
60. Wieneke, S. and C. Gerhard, *Lasers in Medical Diagnosis and Therapy*. 2018: IOP Publishing, Bristol, UK.
61. Mesquita, R.C. and A.G. Yodh, *Diffuse optics: fundamentals and tissue applications.* Nano optics and atomics: transport of light and matter waves, 2011. **173**.
62. Wang, X., et al., *Approximation of Mie scattering parameters in near-infrared tomography of normal breast tissue in vivo.* J Biomed Opt, 2005. **10**(5): p. 051704.
63. Ruiz, J., *Breast Density Quantification Using Structured-light Diffuse Optical Tomography*. 2016, UC Irvine.
64. Kocsis, L., P. Herman, and A. Eke, *The modified Beer-Lambert law revisited.* Phys Med Biol, 2006. **51**(5): p. N91-8.
65. Erickson-Bhatt, S.J., et al., *Noninvasive surface imaging of breast cancer in humans using a hand-held optical imager.* Biomedical physics & engineering express, 2015. **1**(4): p. 045001.
66. Algarawi, M., et al., *Multi-Wavelength Photo-Magnetic Imaging System for Photothermal Therapy Guidance.* Lasers in Surgery and Medicine, 2020.
67. Algarawi, M., et al., *Resolving tissue chromophore concentration at MRI resolution using multi-wavelength photo-magnetic imaging.* Biomedical Optics Express, 2020. **11**(8): p. 4244-4254.

68. Vasudevan, S., et al., *Method for Quantitative Broadband Diffuse Optical Spectroscopy of Tumor-Like Inclusions.* Applied Sciences, 2020. **10**(4): p. 1419.
69. Tromberg, B.J., et al., *Assessing the future of diffuse optical imaging technologies for breast cancer management.* Med Phys, 2008. **35**(6): p. 2443-51.
70. Solomon, M., et al., *Optical imaging in cancer research: basic principles, tumor detection, and therapeutic monitoring.* Medical Principles and Practice, 2011. **20**(5): p. 397-415.
71. Arridge, S.R. and J.C. Hebden, *Optical imaging in medicine: II. Modelling and reconstruction.* Phys Med Biol, 1997. **42**(5): p. 841-53.
72. Boas D A, B.D.H.M.E.L.D.C.A.K.M.G.R.J. and Q. Zhang, *Imaging the body with diffuse optical tomography.* IEEE Sig. Proc. Mag., 2001. **18**(6): p. 57.
73. Ishimaru, A., *Wave propagation and scattering in random media and rough surfaces.* Proceedings of the IEEE, 1991. **79**(10): p. 1359-1366.
74. Haskell, R.C., et al., *Boundary conditions for the diffusion equation in radiative transfer.* J Opt Soc Am A Opt Image Sci Vis, 1994. **11**(10): p. 2727-41.
75. Simon, R.A. and C.S. John, *Optical tomography: forward and inverse problems.* Inverse Problems, 2009. **25**(12): p. 123010.
76. Arridge, S.R., M. Hiraoka, and M. Schweiger, *Statistical basis for the determination of optical pathlength in tissue.* Phys Med Biol, 1995. **40**(9): p. 1539-58.
77. Leng, C. and J. Tian, *Mathematical method in optical molecular imaging.* Science China Information Sciences, 2015. **58**(3): p. 1-13.
78. Dehghani, H., et al., *Near infrared optical tomography using NIRFAST: Algorithm for numerical model and image reconstruction.* Communications in numerical methods in engineering, 2009. **25**(6): p. 711-732.
79. Godavarty, A., et al., *Influence of the refractive index-mismatch at the boundaries measured in fluorescence-enhanced frequency-domain photon migration imaging.* Optics Express, 2002. **10**(15): p. 653-662.
80. Pennes, H.H., *Analysis of tissue and arterial blood temperatures in the resting human forearm.* Journal of applied physiology, 1948. **1**(2): p. 93-122.
81. Wissler, E.H., *Pennes' 1948 paper revisited.* J Appl Physiol (1985), 1998. **85**(1): p. 35-41.
82. Xu, Y., et al., *Mathematical simulation of temperature distribution in tumor tissue and surrounding healthy tissue treated by laser combined with indocyanine green.* Theoretical Biology and Medical Modelling, 2019. **16**(1): p. 1-11.
83. Mohammed, Y. and J.F. Verhey, *A finite element method model to simulate laser interstitial thermo therapy in anatomical inhomogeneous regions.* Biomedical engineering online, 2005. **4**(1): p. 2.
84. Brix, G., et al., *Estimation of heat transfer and temperature rise in partial-body regions during MR procedures: an analytical approach with respect to safety considerations.* Magnetic resonance imaging, 2002. **20**(1): p. 65-76.
85. Erkol, H., et al., *Validation of a comprehensive analytical model for photothermal therapy planning in a layered medium with gold nanoparticles.* International Journal of Heat and Mass Transfer, 2020. **163**: p. 120438.
86. Boas, D.A., et al., *Scattering of diffuse photon density waves by spherical inhomogeneities within turbid media: analytic solution and applications.* Proc Natl Acad Sci U S A, 1994. **91**(11): p. 4887-91.
87. Walker, S.A., D.A. Boas, and E. Gratton, *Photon density waves scattered from cylindrical inhomogeneities: theory and experiments.* Appl Opt, 1998. **37**(10): p. 1935-44.
88. Martelli, F., et al., *Analytical approximate solutions of the time-domain diffusion equation in layered slabs.* JOSA A, 2002. **19**(1): p. 71-80.
89. Wang L, J.S.L. and L. Zheng, *MCML-Monte Carlo modeling of light transport in multi-layered tissues.* Comput. Methods Programs Biomed., 1995. **47**(2): p. 131.

90. Boas D A, C.J.P.S.J.J. and A.K. Dunn, *Three dimensional Monte Carlo code for photon migration through complex heterogenous media including the adult human head.* Opt. Express, 2002. **10**: p. 159.
91. Erkol, H., et al., *Comprehensive analytical model for CW laser induced heat in turbid media.* Optics Express, 2015. **23**(24): p. 31069-31084.
92. Schweiger, M., et al., *The finite element method for the propagation of light in scattering media: boundary and source conditions.* Med Phys, 1995. **22**(11 Pt 1): p. 1779-92.
93. Arridge, S., et al., *A finite element approach for modeling photon transport in tissue.* Medical physics, 1993. **20**(2): p. 299-309.
94. Arridge, S.R., *Methods in diffuse optical imaging.* Philos Transact A Math Phys Eng Sci, 2011. **369**(1955): p. 4558-76.
95. Arridge, S.R. and M. Schweiger, *Image reconstruction in optical tomography.* Philos Trans R Soc Lond B Biol Sci, 1997. **352**(1354): p. 717-26.
96. Rieke, V. and K. Butts Pauly, *MR thermometry.* J Magn Reson Imaging, 2008. **27**(2): p. 376-90.
97. Marquardt, D.W., *An algorithm for least-squares estimation of nonlinear parameters.* Journal of the society for Industrial and Applied Mathematics, 1963. **11**(2): p. 431-441.
98. Levenberg, K., *A method for the solution of certain non–linear problems in least squares.* 1944.
99. Cerussi, A.E., et al., *Spectroscopy enhances the information content of optical mammography.* J Biomed Opt, 2002. **7**(1): p. 60-71.
100. Srinivasan, S., et al., *Near-infrared characterization of breast tumors in vivo using spectrally-constrained reconstruction.* Technol Cancer Res Treat, 2005. **4**(5): p. 513-26.
101. Biswal, N.C., Y. Xu, and Q. Zhu, *Imaging tumor oxyhemoglobin and deoxyhemoglobin concentrations with ultrasound-guided diffuse optical tomography.* Technology in cancer research & treatment, 2011. **10**(5): p. 417-429.
102. Cox B T, A.S.R. and P.C. Beard, *Estimating chromophore distributions from multiwavelength photoacoustic images.* J. Opt. Soc. Am., 2009. **26**(2): p. 443.
103. Corlu A, D.T.C.R.S.M.H.E.M.C.A.S.R. and A.G. Yodh, *Uniqueness and wavelength optimization in continuous-wave multispectral diffuse optical tomography.* Opt. Lett., 2003. **28**(23): p. 2339.
104. Brooksby, B., et al., *Spectral priors improve near-infrared diffuse tomography more than spatial priors.* Opt Lett, 2005. **30**(15): p. 1968-70.
105. Li, A., et al., *Reconstructing chromosphere concentration images directly by continuous-wave diffuse optical tomography.* Opt Lett, 2004. **29**(3): p. 256-8.
106. Corlu, A., et al., *Diffuse optical tomography with spectral constraints and wavelength optimization.* Applied optics, 2005. **44**(11): p. 2082-2093.
107. Algarawi, M., et al. *Reconstruction chromophore concentration directly by Photo-Magnetic Imaging: simulation study*. in *Clinical and Translational Biophotonics*. 2020. Optical Society of America.
108. Srinivasan, S., et al. *Spectrally constrained NIR tomography for breast imaging: Simulations and clinical results*. in *Optical Tomography and Spectroscopy of Tissue VI*. 2005. International Society for Optics and Photonics.
109. Srinivasan, S., et al., *Spectrally constrained chromophore and scattering near-infrared tomography provides quantitative and robust reconstruction.* Applied optics, 2005. **44**(10): p. 1858-1869.
110. Nouizi, F., et al., *Multiwavelength photo-magnetic imaging algorithm improved for direct chromophore concentration recovery using spectral constraints.* Applied Optics, 2021. **60**(35): p. 10855-10861.
111. van Veen, R.L., et al., *Determination of visible near-IR absorption coefficients of mammalian fat using time- and spatially resolved diffuse reflectance and transmission spectroscopy.* J Biomed Opt, 2005. **10**(5): p. 054004.

112. Palmer, K.F. and D. Williams, *Optical properties of water in the near infrared.* JOSA, 1974. **64**(8): p. 1107-1110.
113. Algarawi, M., et al. *High-resolution chromophore concentration recovery using multi-wavelength photo-magnetic imaging*. in *Multimodal Biomedical Imaging XIV*. 2019. International Society for Optics and Photonics.
114. Raj, P.K., *A review of the criteria for people exposure to radiant heat flux from fires.* Journal of Hazardous Materials, 2008. **159**(1): p. 61-71.
115. Srinivasan, S., et al., *Spectrally constrained chromophore and scattering near-infrared tomography provides quantitative and robust reconstruction.* Appl Opt, 2005. **44**(10): p. 1858-69.
116. Kishore, R.A., et al., *Ultra-high performance wearable thermoelectric coolers with less materials.* Nature communications, 2019. **10**(1): p. 1-13.
117. Fu, G., et al., *Nanoparticle-mediated photothermal effect enables a new method for quantitative biochemical analysis using a thermometer.* Nanoscale, 2016. **8**(10): p. 5422-5427.
118. Ma, Y., et al., *Indocyanine green loaded SPIO nanoparticles with phospholipid-PEG coating for dual-modal imaging and photothermal therapy.* Biomaterials, 2013. **34**(31): p. 7706-7714.
119. Long, S., et al., *Characteristics of temperature changes in photothermal therapy induced by combined application of indocyanine green and laser.* Oncology Letters, 2019. **17**(4): p. 3952-3959.
120. Hirohashi, K., et al., *Lung cancer photothermal ablation by low-power near-infrared laser and topical injection of indocyanine green.* Interactive cardiovascular and thoracic surgery, 2019. **29**(5): p. 693-698.
121. West, C.L., et al., *Monitoring tissue temperature during photothermal therapy for cancer.* Journal of bio-X research, 2019. **2**(4): p. 159.
122. Chen, Y., et al., *Magnetic resonance imaging guidance for laser photothermal therapy.* Journal of biomedical optics, 2008. **13**(4): p. 044033.
123. Odéen, H. and D.L. Parker, *Magnetic resonance thermometry and its biological applications–Physical principles and practical considerations.* Progress in nuclear magnetic resonance spectroscopy, 2019. **110**: p. 34-61.
124. Hindman, J., *Proton resonance shift of water in the gas and liquid states.* The Journal of Chemical Physics, 1966. **44**(12): p. 4582-4592.
125. Goldstein, R.M., H.A. Zebker, and C.L. Werner, *Satellite radar interferometry: Two-dimensional phase unwrapping.* Radio science, 1988. **23**(4): p. 713-720.
126. Luk, A.T., *A True Multi-modality System for Optical Imaging with MR Resolution: Photo-magnetic Imaging*. 2016, UC Irvine.
127. Xiao, Y.-D., et al., *MRI contrast agents: Classification and application.* International journal of molecular medicine, 2016. **38**(5): p. 1319-1326.
128. Silver, N., et al., *Sensitivity of contrast enhanced MRI in multiple sclerosis. Effects of gadolinium dose, magnetization transfer contrast and delayed imaging.* Brain: a journal of neurology, 1997. **120**(7): p. 1149-1161.
129. Johnson, A.D. and K. Sherwin, *Foundations of mechanical engineering*. 1996: CRC Press.
130. Unlu B.M, B.O., Shafihaa R., Gulsen G., Nalcioglu O., *Diffuse Optical Tomographic Reconstruction Using Multi-frequency Data.* J Biomed Opt, 2006. **11**(5): p. 054008.
131. Van Staveren, H.J., et al., *Light scattering in lntralipid-10% in the wavelength range of 400–1100 nm.* Applied optics, 1991. **30**(31): p. 4507-4514.
132. Zhu, Q., et al., *Early-stage invasive breast cancers: potential role of optical tomography with US localization in assisting diagnosis.* Radiology, 2010. **256**(2): p. 367-378.
133. Shurrab, K.M. and M.S. El-Daher, *Simulation and study of temperature distribution in living biological tissues under laser irradiation.* Journal of lasers in medical sciences, 2014. **5**(3): p. 135.